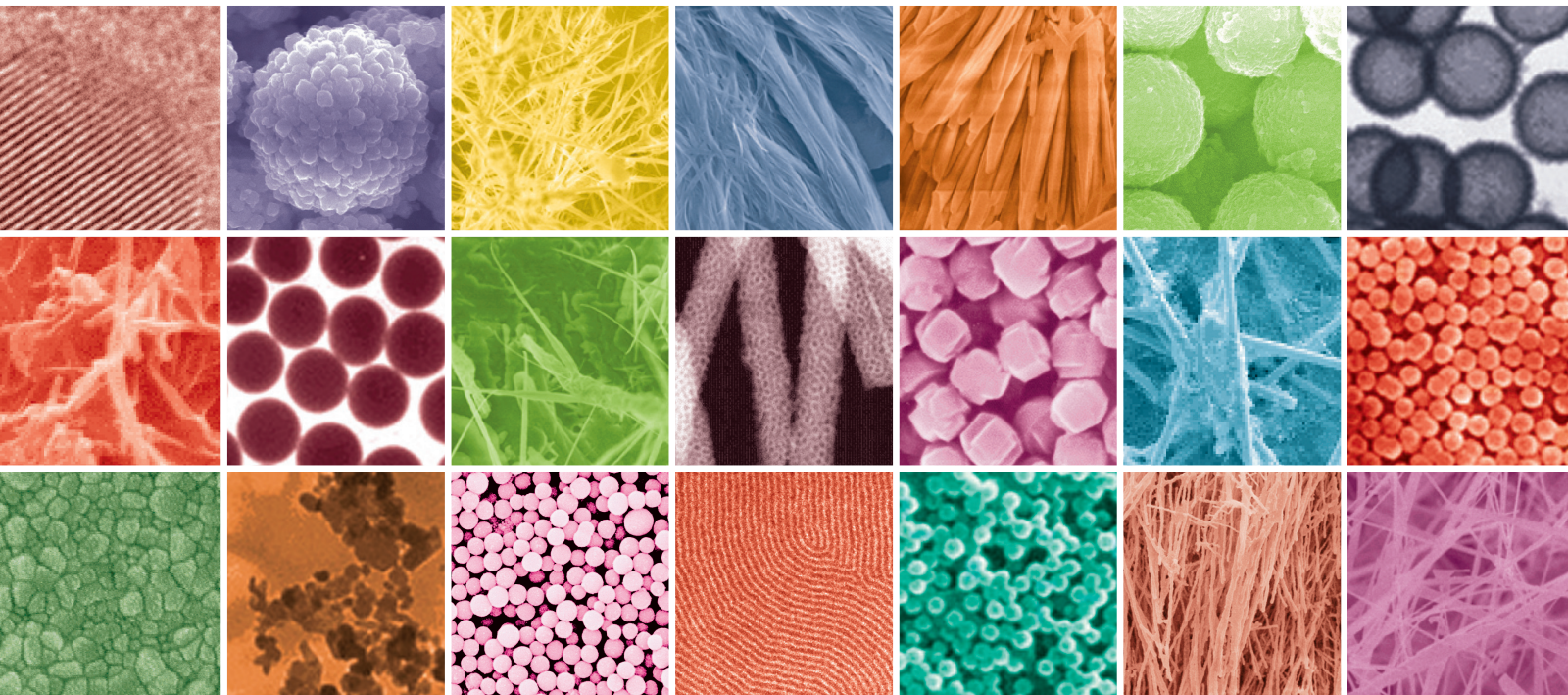


Nanofiber Manufacture, Properties, and Applications 2013

Guest Editors: Tong Lin, Gajanan S. Bhat, and Raghavendra Hegde





**Nanofiber Manufacture, Properties,
and Applications 2013**

Journal of Nanomaterials

**Nanofiber Manufacture, Properties,
and Applications 2013**

Guest Editors: Tong Lin, Gajanan S. Bhat,
and Raghavendra Hegde



Copyright © 2014 Hindawi Publishing Corporation. All rights reserved.

This is a special issue published in "Journal of Nanomaterials." All articles are open access articles distributed under the Creative Commons Attribution License, which permits unrestricted use, distribution, and reproduction in any medium, provided the original work is properly cited.

Editorial Board

K. E. Aifantis, Greece
Nageh K. Allam, USA
Margarida Amaral, Portugal
Xuedong Bai, China
Lavinia Balan, France
Enrico Bergamaschi, Italy
T. Borca-Tasciuc, USA
C. Jeffrey Brinker, USA
Christian Brosseau, France
Xuebo Cao, China
Shafiq Chowdhury, USA
Kwang-Leong Choy, UK
Cui ChunXiang, China
M. A. Correa-Duarte, Spain
Shadi A. Dayeh, USA
Ali Eftekhari, USA
Claude Estourns, France
Alan Fuchs, USA
Lian Gao, China
Russell E. Gorga, USA
Hongchen Chen Gu, China
Mustafa O. Guler, Turkey
John Zhanhu Guo, USA
Smrati Gupta, Germany
Michael Harris, USA
Zhongkui Hong, China
Michael Z. Hu, USA
David Hui, USA
Y.-K. Jeong, Republic of Korea
Sheng-Rui Jian, Taiwan
Wanqin Jin, China
Rakesh K. Joshi, UK
Zhenhui Kang, China
F. Karimzadeh, Iran
Alireza Khataee, Iran

Do Kyung Kim, Korea
Alan K. T. Lau, Hong Kong
Burtrand Lee, USA
Jun Li, Singapore
Benxia Li, China
Xing-Jie Liang, China
Shijun Liao, China
Gong-Ru Lin, Taiwan
Tianxi Liu, China
J. -Y. Liu, USA
Songwei Lu, USA
Daniel Lu, China
Jue Lu, USA
Ed Ma, USA
Gaurav Mago, USA
Santanu K. Maiti, India
Sanjay R. Mathur, Germany
Vikas Mittal, UAE
Weihai Ni, Germany
Sherine Obare, USA
Atsuto Okamoto, Japan
Abdelwahab Omri, Canada
Edward Andrew Payzant, USA
Kui-Qing Peng, China
Anukorn Phuruangrat, Thailand
Mahendra Rai, India
S. Sinha Ray, South Africa
Ugur Serincan, Turkey
Huaiyu Shao, Japan
Donglu Shi, USA
Vladimir Sivakov, Germany
Marinella Striccoli, Italy
Bohua Sun, South Africa
Saikat Talapatra, USA
Nairong Tao, China

Titipun Thongtem, Thailand
Somchai Thongtem, Thailand
Alexander Tolmachev, Ukraine
Valeri P. Tolstoy, Russia
Tsung-Yen Tsai, Taiwan
Takuya Tsuzuki, Australia
Raquel Verdejo, Spain
Mat U. Wahit, Malaysia
Zhenbo Wang, China
Ruibing Wang, Canada
Shiren Wang, USA
Cheng Wang, China
Yong Wang, USA
Jinquan Wei, China
Ching-Ping Wong, Hong Kong
Xingcai Wu, China
Guodong Xia, Hong Kong
Ping Xiao, UK
Zhi Li Xiao, USA
Yangchuan Xing, USA
Shuangxi Xing, China
N. Xu, China
Doron Yadlovker, Israel
Yingkui Yang, China
Khaled Youssef, USA
Kui Yu, Canada
William W. Yu, USA
Haibo Zeng, China
Tianyou Zhai, Japan
Renyun Zhang, Sweden
Bin Zhang, China
Yanbao Zhao, China
Lianxi Zheng, Singapore
Chunyi Zhi, Hong Kong

Contents

Nanofiber Manufacture, Properties, and Applications 2013, Tong Lin, Gajanan S. Bhat, and Raghavendra Hegde
Volume 2014, Article ID 543678, 2 pages

Low Temperature Flex-on-Flex Assembly Using Polyvinylidene Fluoride Nanofiber Incorporated Sn58Bi Solder Anisotropic Conductive Films and Vertical Ultrasonic Bonding, Tae-Wan Kim, Kyung-Lim Suk, Sang-Hoon Lee, and Kyung-Wook Paik
Volume 2013, Article ID 534709, 10 pages

On the Nature of Electric Current in the Electrospinning Process, Baturalp Yalcinkaya, Fatma Yener, Oldrich Jirsak, and Funda Cengiz-Callioglu
Volume 2013, Article ID 538179, 10 pages

Improved Methane Sensing Properties of Co-Doped SnO₂ Electrospun Nanofibers, Weigen Chen, Qu Zhou, Lingna Xu, Fu Wan, Shudi Peng, and Wen Zeng
Volume 2013, Article ID 173232, 9 pages

Synthesis and Characterization of Drug-Loaded Poly(ϵ -caprolactone)/Silica Hybrid Nanofibrous Scaffolds, Kwan-Ha Shin, Young-Hag Koh, and Hyoun-Ee Kim
Volume 2013, Article ID 351810, 12 pages

A Mucoadhesive Electrospun Nanofibrous Matrix for Rapid Oramucosal Drug Delivery, Clare Dott, Charu Tyagi, Lomas K. Tomar, Yahya E. Choonara, Pradeep Kumar, Lisa C. du Toit, and Viness Pillay
Volume 2013, Article ID 924947, 19 pages

A Study of Surface Modifications of Carbon Nanotubes on the Properties of Polyamide 66/Multiwalled Carbon Nanotube Composites, Li Qiu, Yongkang Chen, Yongzhen Yang, Lihua Xu, and Xuguang Liu
Volume 2013, Article ID 252417, 8 pages

Nanofibrous *p-n* Junction and Its Rectifying Characteristics, Jian Fang, Xungai Wang, and Tong Lin
Volume 2013, Article ID 758395, 7 pages

Editorial

Nanofiber Manufacture, Properties, and Applications 2013

Tong Lin,¹ Gajanan S. Bhat,² and Raghavendra Hegde³

¹ Australian Future Fibres Research and Innovation Centre, Institute for Frontier Materials, Deakin University, 75 Pigdons Road, Waurin Ponds, VIC 3216, Australia

² Nonwovens Research Laboratory, The University of Tennessee, 1321 White Avenue, Knoxville, TN 37996, USA

³ Domtar Personal Care, 2332 US Highway 42 South, Delaware, OH 43015, USA

Correspondence should be addressed to Tong Lin; tong.lin@deakin.edu.au

Received 12 January 2014; Accepted 12 January 2014; Published 18 February 2014

Copyright © 2014 Tong Lin et al. This is an open access article distributed under the Creative Commons Attribution License, which permits unrestricted use, distribution, and reproduction in any medium, provided the original work is properly cited.

Nanofibers possess versatile properties and wide applications. Although they can be prepared by several different methods, electrospinning is distinct from other nanofiber-making techniques in versatility to process different polymers, ability to control fiber diameter, morphology, orientation, component and fibrous structure, and potential for large-scale production. The ease of electrospinning nanofibers on small scales, mainly using a needle-based electrospinning setup, in laboratories has considerably facilitated researchers' finding of the unique properties and applications of electrospun nanofibers.

This special issue highlights the functional applications of electrospun nanofibers in gas sensor, drug delivery, and electronics fields. A planar-type methane sensor was prepared from a doped electrospun SnO₂ nanofiber. The sensor was reported to have good stability, prominent reproducibility, and excellent selectivity. In comparison with SnO₂ nanospheres, which were used conventionally for making methane sensors, the nanofibers had higher gas response and saturated detection concentration, as well as quicker response-recovery time.

Controlling drug release has many applications in the biomedical field. In one of the papers on drug delivery nanofibers, drug was loaded in polymer/silica hybrid nanofibers. The presence of the silica remarkably enhanced drug loading efficiency, nanofiber hydrophilicity, and mechanical properties. Assessed by *in vitro* cell tests, the hybrid nanofibers showed good biocompatibility for guided bone regeneration. Another paper reports drug loaded nanofibers which were electrospun directly onto a polymeric

backing film. The optimized nanofiber/film matrix system showed enhancement in drug dissolution rate, useful for rapid mucosal drug delivery.

Two papers on electronics applications of electrospun nanofibers were included in this special issue. One paper reports on the *p-n* junction and rectifying property of a layered fibrous mat consisting of inorganic nanofibers and conducting polymer nanofibers. The fibrous mat had an obvious diode-rectifying characteristic, and the thickness of the nanofiber layers considerably influenced the device resistance and rectifying performance. Such nanofibrous diode rectifier may find applications in sensors, energy harvest, and electronic textiles. Another paper is on electrode connection solder. Short circuit often occurs at fine pitch interconnections of electronic devices. To solve this problem, solder balls were incorporated into polyvinylidene fluoride nanofibers through electrospinning. The nanofiber solder showed considerable improvement in solder capture rate and 100% insulation between electrodes. It also improved contact conductivity, current handling ability, and reliability.

The special issue also collects fundamental research on electrospinning. Electric current between electrospinning electrodes originates from the movement of charge carriers through the spinning space. It was reported that the majority of charge carriers were formed by ionization of the air close to the metallic needle nozzle or the polymer jet. The addition of salt to polymer solution increased the carrier concentration. However, the conductivity of polymer jets did not significantly affect the current since the jets did not link the electrodes.

Apart from electrospun nanofibers, a paper on multi-walled carbon nanotube (MWCNT)/polyamide 66 composites is also included in this special issue. MWCNTs with surfaces modified separately with acid and amine groups were used as fillers. The amine-modified MWCNTs showed better dispersion in the polymer matrix than pristine- and acid-modified MWCNTs. They induced heterogeneous nucleation of PA66 and significantly improved the composite hardness and elastic modulus.

As guest editors of this special issue, we are pleased to see this progress. We hope that this special issue will contribute to the wide use of nanofibers and that the papers collected in this special issue are well received by the reader.

Acknowledgments

The editors gratefully thank the authors for their contributions to this special issue and the reviewers for their constructive comments and dedication.

*Tong Lin
Gajanan S. Bhat
Raghavendra Hegde*

Research Article

Low Temperature Flex-on-Flex Assembly Using Polyvinylidene Fluoride Nanofiber Incorporated Sn58Bi Solder Anisotropic Conductive Films and Vertical Ultrasonic Bonding

Tae-Wan Kim, Kyung-Lim Suk, Sang-Hoon Lee, and Kyung-Wook Paik

Department of Materials Science and Engineering, Korea Advanced Institute of Science and Technology (KAIST),
291 Daehak-ro, Yuseong-gu, Daejeon 305-701, Republic of Korea

Correspondence should be addressed to Kyung-Lim Suk; stones01@kaist.ac.kr and Sang-Hoon Lee; svl5083@kaist.ac.kr

Received 9 August 2013; Accepted 15 November 2013

Academic Editor: Gajanan S. Bhat

Copyright © 2013 Tae-Wan Kim et al. This is an open access article distributed under the Creative Commons Attribution License, which permits unrestricted use, distribution, and reproduction in any medium, provided the original work is properly cited.

In this study, solder ball incorporated polyvinylidene fluoride (PVDF) nanofiber was added into the ACF system to overcome short circuit issues of fine pitch flex-on-flex (FOF) assembly. Also, in order to improve the thermal mismatch of the flexible substrate which can lead to electrode misalignment during the bonding process, low melting temperature Sn58Bi solder balls were used with vertical ultrasonic (U/S) bonding method. When performing FOF assembly using PVDF nanofiber/Sn58Bi solder ACF and vertical ultrasonic bonding, PVDF nanofiber/Sn58Bi solder ACFs showed 34% higher solder capture rate on an electrode compared to conventional Ni ACFs and conventional Sn58Bi solder ACFs. Additionally, PVDF nanofiber/Sn58Bi solder ACFs showed 100% insulation between neighboring electrodes where conventional Ni ACFs and conventional Sn58Bi solder ACFs showed 75% and 87.5% insulation. Other electrical properties such as contact resistance and current handling capability as well as reliability test of PVDF nanofiber/Sn58Bi solder ACFs showed improved results compared to those of conventional Ni ACFs, which proves the formation of stable solder joint of PVDF nanofiber/Sn58Bi solder ACFs.

1. Introduction

The rapid development of portable electronic products requires miniaturized, multifunctional, and high performance package products. In order to fulfill these requirements, flex-on-flex (FOF) assembly was introduced due to its fine pitch capability and reduced assembly thickness and areas [1].

In various electronic interconnections, anisotropic conductive films (ACFs) are commonly used as an interconnecting material [2–7]. These ACFs are well-known adhesive materials which consist of conductive particles and polymer resin material. However, for conventional ACFs, conductive particle such as gold coated Ni ball showed insufficient power carrying capability as well as reliability due to the physical contact after bonding. In order to overcome this barrier, metallurgical bonding based solder ACFs with vertical ultrasonic bonding were introduced previously where solder

ACFs showed excellent metallurgical solder joint formation resulting excellent electrical properties and reliability [8–10].

But, when it comes to fine pitch application, solder balls have the tendency to agglomerate between the neighboring electrodes resulting short circuit. Regarding the short circuit issue, nanofiber incorporated ACFs were introduced in the past [11–15] in our group using electrospinning technique [16–19].

In this paper, we will introduce Sn58Bi (melting point: 138°C) incorporated nanofiber/solder ACF. Commonly used solder ball such as SAC305 (96.5% Sn, 3% Ag, and 0.5% Cu with a melting point of 217°C) requires high bonding temperature (~250°C) in order to form stable metallurgical joints. This high temperature can cause thermal mismatch of the substrate during bonding process which leads to electrode misalignment. By using Sn58Bi solder ball instead of SAC305 solder ball, it is possible to lower the bonding temperature which will also lower the thermal mismatch between the top

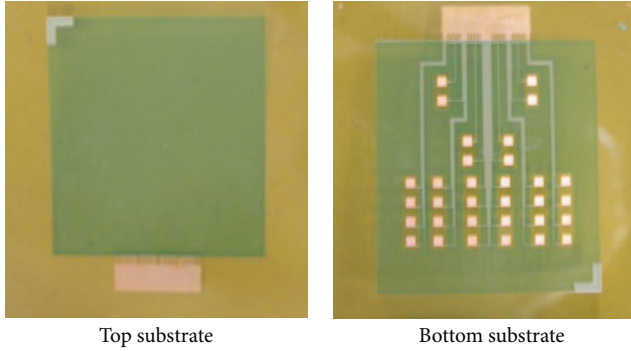


FIGURE 1: The images of 100 μm pitch top and bottom flexible printed substrates (FPCs).

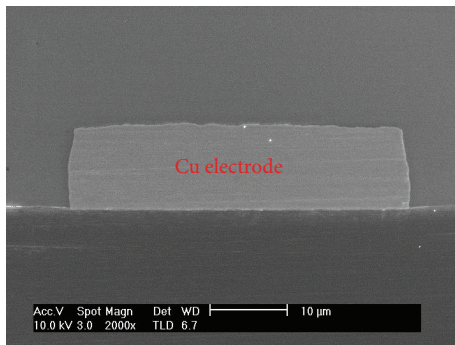


FIGURE 2: The SEM image of the copper electrode of 100 μm pitch FPC.

and bottom substrate as well as forming stable solder joint in fine pitch FOF assembly.

2. Experimental

2.1. Material Preparation and Equipment

2.1.1. Test Vehicle Preparation. Polyimide base 100 μm pitch flexible printed circuits (FPCs) were designed as shown in Figure 1. Both top and bottom flexible substrates contain 96 electrodes and the height of each electrode was around 12 μm shown in Figure 2. The main bonding area of the FPC was 2 mm \times 10 mm. The electrodes of the FPCs were copper electrodes. The copper electrodes were then treated with 100 nm thick organic solderability preservative (OSP) material in order to prevent any additional oxidation. The bottom FPC contains six contact resistance measurement points and four insulation resistance measurement points.

2.1.2. PVDF Nanofiber/Sn58Bi Solder ACF Formation. Nanofibers containing Sn58Bi solder balls were electrospun using the electrospinning equipment shown in Figure 3. Electrospinning is a common method used to produce nanofibers, where voltage is applied to the syringe needle generating a charge at the tip of the needle. As the polymer solution is charged, this will act as a driving force for the polymer solution to migrate from the tip of the needle to

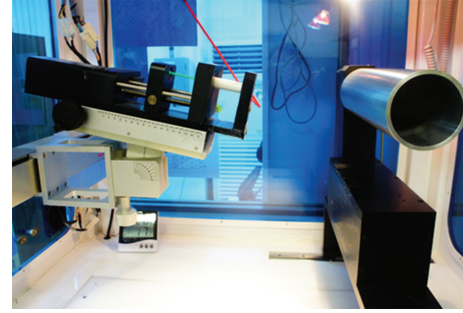


FIGURE 3: The Image of the electrospinning apparatus.

the ground collector producing nanofibers. The nanofiber diameter can be controlled by changing the polymer concentration, applied voltage, working distance, pump rate, and so forth. The compositions of the ACF materials are shown in Table 1. For the optimized PVDF nanofiber/solder ACF, the polymer solution consisted of 15 wt.% of PVDF, 42 wt.% dimethylacetamide (DMAC), and 28 wt.% acetone along with 15 wt.% Sn58Bi solder balls. After the polymer solution was well mixed with solder balls, the mixed polymer solution was then transported to the syringe followed by the electrospinning process. The PVDF nanofiber was electrospun at 10 KV while working distance, pumping rate, and needle diameter were fixed as 10 cm, 20 $\mu\text{L}/\text{min}$, and 250 μm . Then the Sn58Bi solder ball incorporated PVDF nanofiber layer was fabricated and the fiber layer was laminated between two nonconductive films (NCFs) with a thickness of 10 μm using the roll and vacuum laminator resulting in final PVDF nanofiber/Sn58Bi solder ACFs with a thickness of 25 μm .

2.1.3. Vertical Ultrasonic Bonding Apparatus. Solder ball normally contains native oxide, which prevents solder joint to form well. By applying vertical ultrasonic bonding, this native oxide layer can be broken during the bonding process. The vertical ultrasonic (U/S) bonding apparatus was developed previously, and Figure 4(a) shows the one used in this experiment. The longitudinal vibration frequency of the bonder was 40 KHz and the output power was 400 W. Also, the U/S vibration amplitude ranged from 4 to 13 μm . The U/S bonding apparatus have 3 important regions: bonding region, preparation region, and aligning region. The U/S vibration is applied at room temperature and the vibration is mainly applied on the bonding horn located in the bonding region shown in Figure 4(b). The size of the U/S horn was 22 mm \times 3 mm which covers the ACF bonding area of FOF assembly. And 200 μm thick silicone interposer was placed between the horn and the FPC. The schematic of the ultrasonic bonding process is shown in Figure 5.

2.2. Optimization of Vertical Ultrasonic Bonding Condition. In this experiment, the bonding condition is divided into prebonding condition and main bonding condition. The bonding conditions were decided based on the resin curing temperature, Sn58Bi solder ball melting temperature, and

TABLE I: The material composition of conventional Ni ACFs, conventional Sn58Bi solder ACFs, and PVDF nanofiber/Sn58Bi solder ACFs.

ACF type	Conventional ACF	Solder ACF	Nanofiber solder ACF
Conductive particle content (wt.%)	30 wt.% Ni ball	20 wt.% Sn58Bi solder ball	15 wt.% Sn58Bi solder ball
Conductive particle size (μm)	8 μm	5~15 μm	5~15 μm
Nanofiber material	—	—	PVDF
Resin type	Epoxy	Epoxy	Epoxy

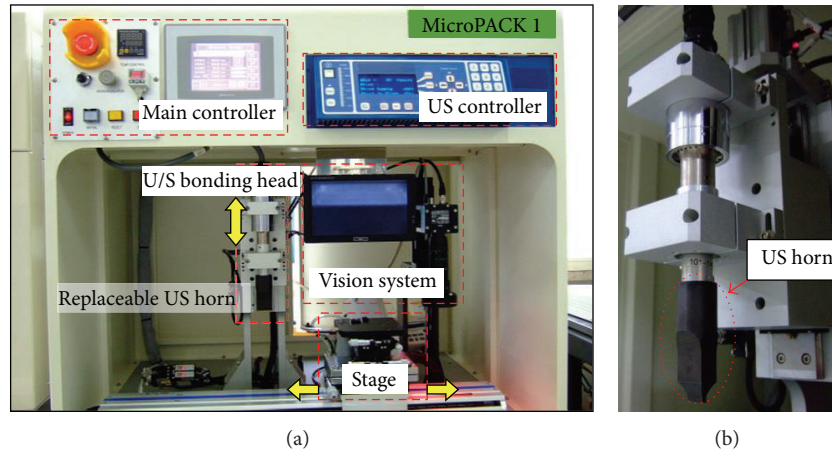


FIGURE 4: The image of (a) U/S bonding apparatus and (b) U/S horn for FOF bonding.

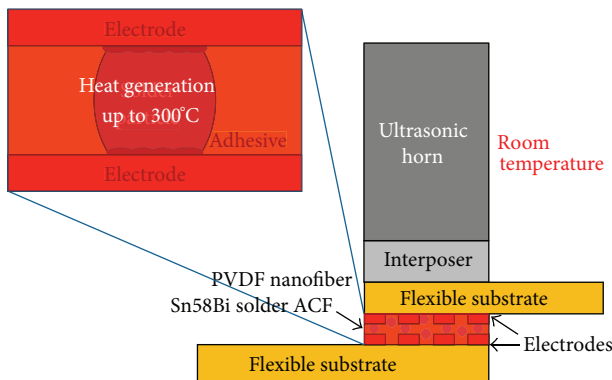


FIGURE 5: The schematic image of the ultrasonic FOF bonding process.

PVDF melting temperature which was determined by the DSC curve. The prebonding condition was selected so that the conductive particles were captured between the top and bottom electrodes before the main bonding preventing any resin capture during the main bonding process. The main bonding condition was selected so that the solder ball melting occurs while fully curing the resin. Lee et al. performed FOF assembly using 250°C as a bonding temperature due to the use of SAC305 solder ball which has a melting point of 217°C. However, high bonding temperature can result high thermal mismatch resulting electrode misalignment. Thus, in this experiment, both 200°C and 250°C were considered as bonding temperature candidates for comparison. For comparison, the main bonding pressure and time was fixed to

3 MPa 5 sec bonding. Thermal mismatch between the top and bottom FPCs was observed through the optical microscope. In order to measure the total misalignment length one side of the electrode was aligned perfectly while the other side is misaligned. The misalignment value was then compared with the dimensional change of the FPC using the thermal mechanical analysis (TMA) in order to confirm the bonding temperature effect on the thermal mismatch. In addition, the degree of curing was measured through the Fourier transform infrared spectroscopy (FT-IR).

2.3. Characterization of Nanofiber Effects on ACF Joint Properties

2.3.1. Conductive Particle Movement Analysis. During the prebonding process, conductive particles tend to move due to polymer resin flow. The conductive particle movements were observed before and after prebonding through the microscopic image. Since it is difficult to observe the conductive particles directly through the metal electrodes using the optical microscope, we use a 26 μm thick transparent PI film on one side and 100 μm pitch FPC on the other side in order to observe the particle movement through the microscope. The number of conductive particles for conventional Ni ACFs, conventional Sn58Bi solder ACFs, and PVDF nanofiber/Sn58Bi solder ACFs was counted and recorded in order to confirm the nanofiber effect on the solder movement. The number of conductive particles captured was then converted to the particle capture rate for comparison.

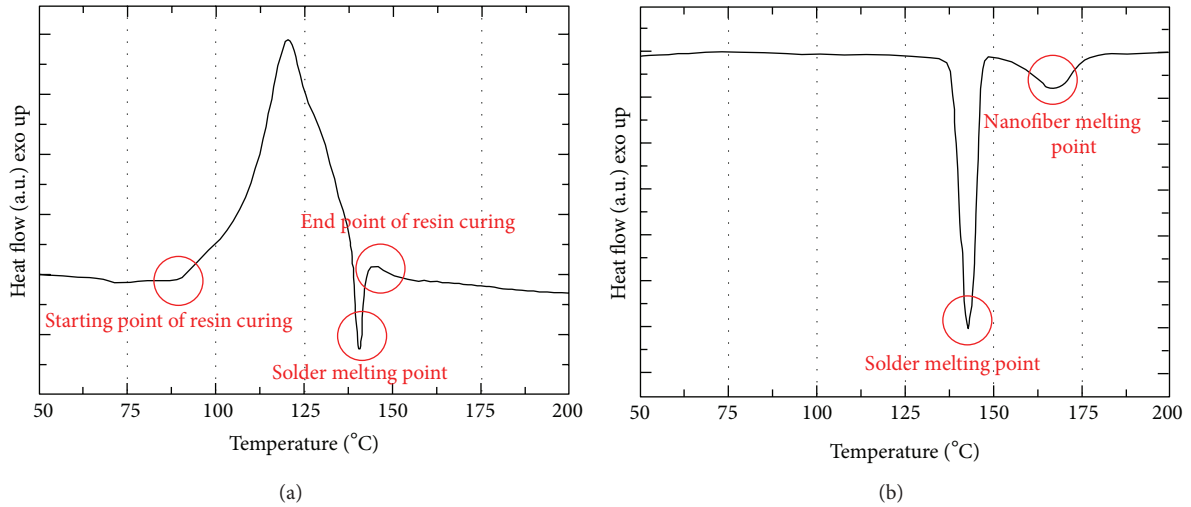


FIGURE 8: The DSC curve of (a) epoxy base resin containing Sn58Bi solder balls and (b) PVDF nanofiber containing Sn58Bi solder balls.

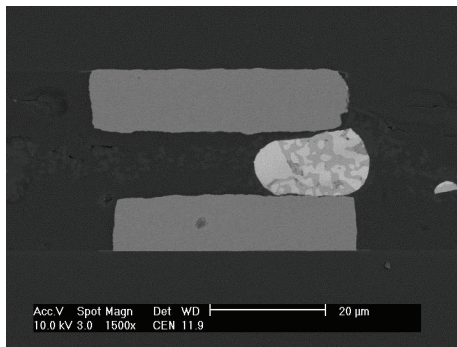


FIGURE 9: The SEM image of joint formation area after the prebonding condition.

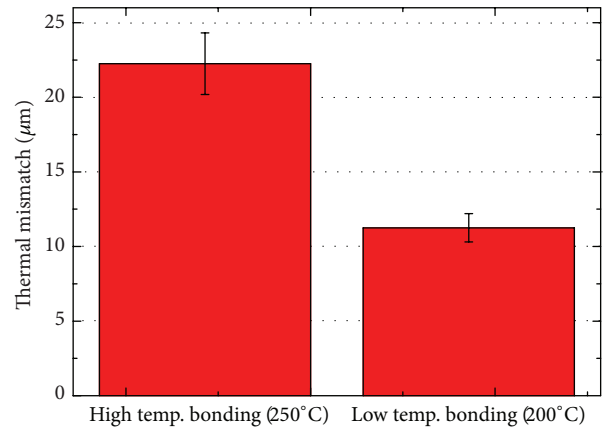


FIGURE 11: The thermal mismatch results of 200°C and 250°C bonding temperature.

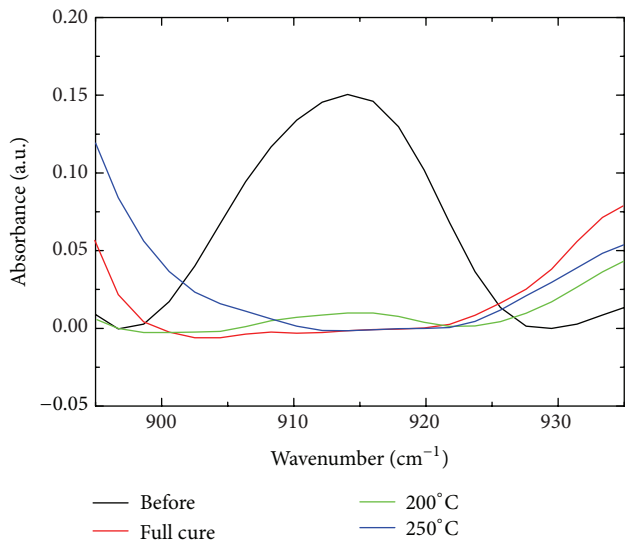


FIGURE 10: The FT-IR results of 200°C and 250°C bonding temperatures.

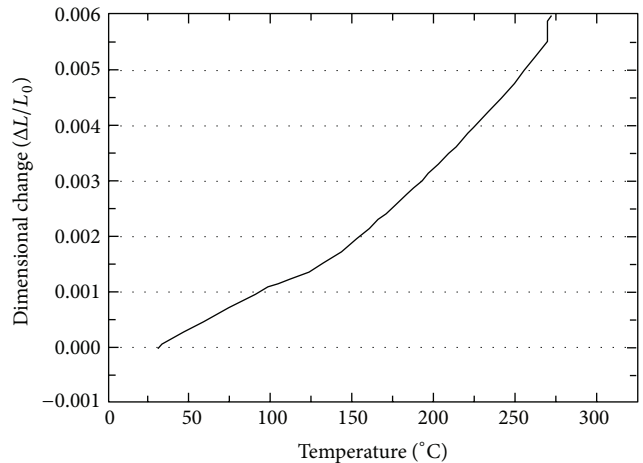


FIGURE 12: The dimensional change curve of FPC substrate using TMA.

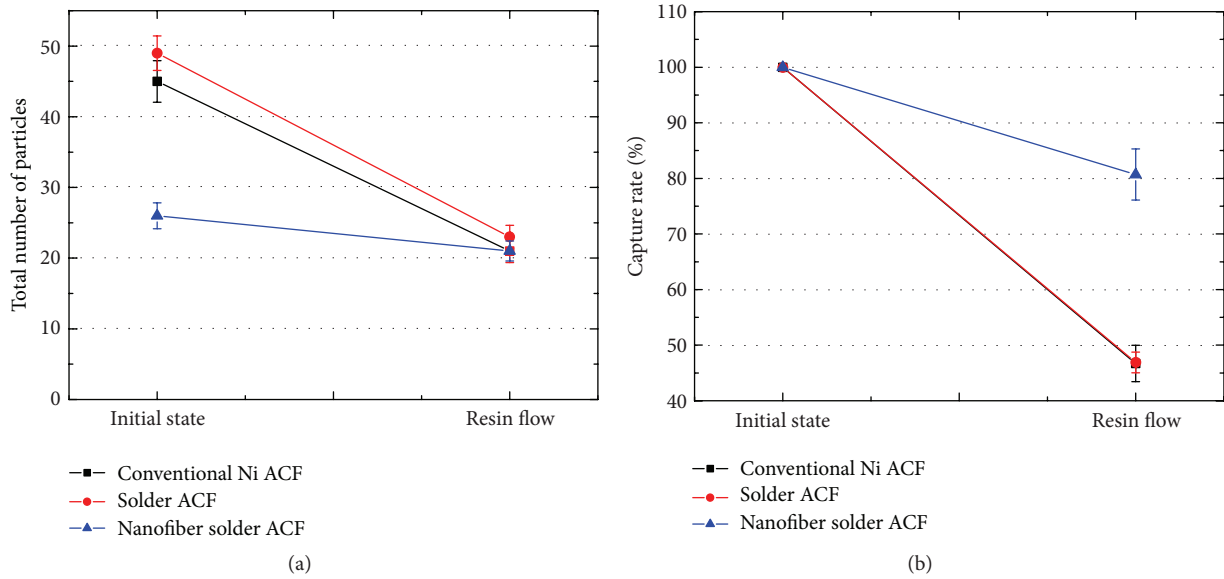


FIGURE 13: The conductive particle movement analysis results of conventional Ni ACFs, conventional Sn58Bi solder ACFs, and PVDF nanofiber/Sn58Bi solder ACFs. (a) Number of conductive particles on the electrode and (b) conductive particle capture rates before and after bonding.

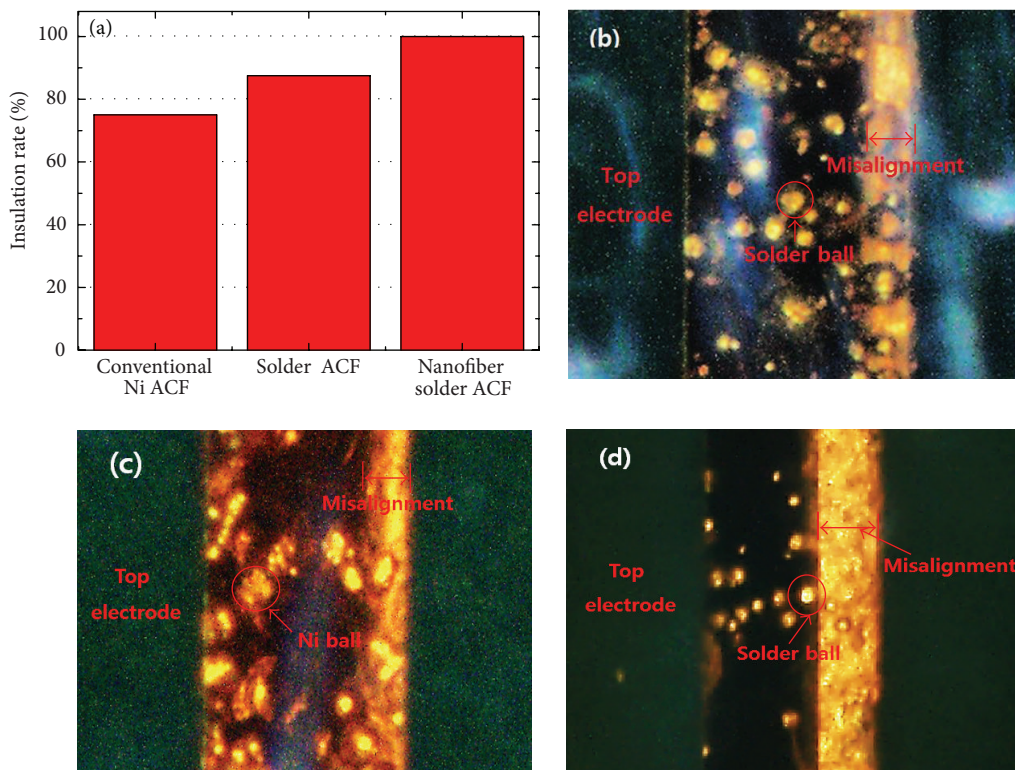


FIGURE 14: (a) The insulation resistance results of conventional Ni ACFs, conventional Sn58Bi solder ACFs, and PVDF nanofiber/Sn58Bi solder ACFs. (b) The optical image of the short circuit region between the neighboring electrodes of the conventional Sn58Bi solder ACFs. (c) The optical image of the short circuit region between the neighboring electrodes of the conventional Ni ACFs. (d) The optical image of the neighboring electrodes of PVDF nanofiber/Sn58Bi solder ACFs.

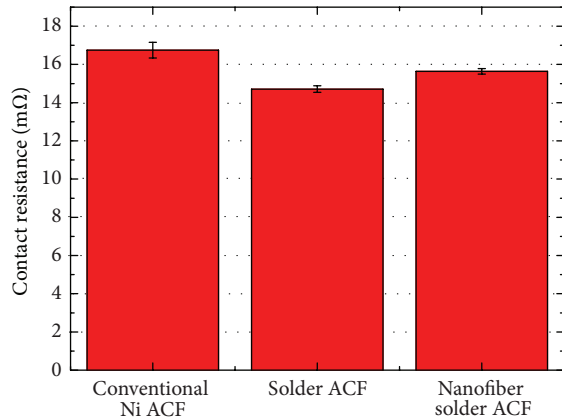


FIGURE 15: The contact resistance of conventional Ni ACFs, conventional Sn58Bi solder ACFs, and PVDF nanofiber/Sn58Bi solder ACFs.

Figure 9. It is shown that the film thickness was reduced down to $10\ \mu\text{m}$, where solder ball is closely in contact with the top and bottom electrodes. And then the main bonding was performed to melt the Sn58Bi solder ball and PVDF nanofiber and cure ACF resin finally. As mentioned before for comparison the main bonding pressure and time were set to 3 MPa 5 sec bonding for comparison. In order to select the main bonding temperature, degree of curing and thermal mismatch were measured. The FT-IR results for 200°C and 250°C bonded samples are shown in Figure 10. As the resin is cured, the integrated area near $915\ \text{cm}^{-1}$ tends to decrease. For both 200°C and 250°C bonded samples, more than 90% resin curing occurred. However when observing the PI film thermal mismatch result after the main bonding process shown in Figure 11, 250°C bonded sample showed an average thermal mismatch value of $22\ \mu\text{m}$ where 200°C bonded sample showed an average thermal mismatch value of $11\ \mu\text{m}$. Since the top and bottom FPCs are of the same material, it is expected that the misalignment is due to the thermal gradient. When observing through the thermodetector, the temperature difference between the top flex and the bottom flex was around 150°C . The misalignment values were compared with the dimensional change results of FPCs using the thermal mechanical analysis (TMA) shown in Figure 12. By lowering the bonding temperature to 200°C , the thermal mismatch between the top and bottom FPC was lowered which eventually improved the electrode misalignment.

3.3. Characterization of Nanofiber Effects on ACF Joint Properties

3.3.1. *Conductive Particle Movement Analysis.* The results of conductive particle movement analysis are shown in Figure 13. For conventional Ni ACFs and conventional Sn58Bi solder ACFs, the number of conductive particles located on the electrode area before prebonding was 45 and 49 for $10000\ \mu\text{m}^2$ area. However, after the prebonding

process, the number of conductive particles reduced down to 21 and 23 resulting 47% capture rate for both ACFs. In contrast, for the PVDF nanofiber/Sn58Bi solder ACFs, 26 solder balls were counted before the prebonding process, and 21 solder balls were captured after the prebonding process, resulting in 81% capture rate. By using PVDF nanofiber, the conductive particle capture rate was increased by 33% compared with the conventional Ni ACFs and conventional Sn58Bi solder ACFs because of the suppression of solder ball movement during the prebonding process.

3.3.2. *Electrical Property Analysis.* PVDF nanofiber forms an insulation coating around the solder ball acting as an insulation layer. The insulation property results for conventional Ni ACFs, conventional Sn58Bi solder ACFs, and PVDF nanofiber/Sn58Bi solder ACFs are shown in Figure 14(a). For conventional Ni ACFs and conventional Sn58Bi solder ACFs, conductive particles tend to agglomerate between the electrodes resulting in short circuit after the bonding process. Conventional Ni ACFs and conventional Sn58Bi solder ACFs showed 75% and 87.5% insulation rate, while no short circuit was observed for the PVDF nanofiber/Sn58Bi solder ACFs, showing 100% insulation property which in other words is 0% short circuit. The optical images of the short circuit region are shown in Figures 14(b) and 14(c). Also, the optical image for the PVDF nanofiber/Sn58Bi solder ACF is shown in Figure 14(d). It was shown that, even though the solder balls tend to agglomerate, the solder ball showed no direct contact due to the nanofiber. This result clearly proves the excellent insulation property of PVDF nanofiber/Sn58Bi solder ACFs compared with conventional Ni ACFs and conventional Sn58Bi solder ACFs. In addition, the average contact resistances of conventional Ni ACFs, conventional Sn58Bi solder ACFs, and PVDF nanofiber Sn58Bi solder ACFs were 16.7 mΩ, 14.7 mΩ, and 15.6 mΩ, respectively, as shown in Figure 15. For conventional Ni ACFs, the Ni ball forms a physical contact with the electrodes preserving its shape, while, for conventional Sn58Bi solder ACFs and PVDF nanofiber/Sn58Bi solder ACFs, the solder ball spreads out forming a metallurgical joint with the electrodes allowing larger contact area. This is why conventional Ni ACF showed the highest contact resistance.

3.3.3. *ACF Joint Analysis.* The conductive particles form contact joints which act as an electrical pathway. The SEM images for conventional Ni ACFs, Sn58Bi conventional solder ACFs, and PVDF nanofiber/Sn58Bi solder ACFs joints are shown in Figure 16. It is shown that both conventional Sn58Bi solder ACFs and PVDF nanofiber/Sn58Bi solder ACFs form excellent solder metallurgical joint which forms Cu-Sn intermetallic compounds (IMC) layer where conventional Ni ACFs only form physical contact resulting less stable joints. Also, the contact areas for conventional Sn58Bi solder ACF and PVDF nanofiber/Sn58Bi solder ACF joints were larger than that for the conventional Ni ACFs resulting stable contact resistances as well as good reliability explained later.

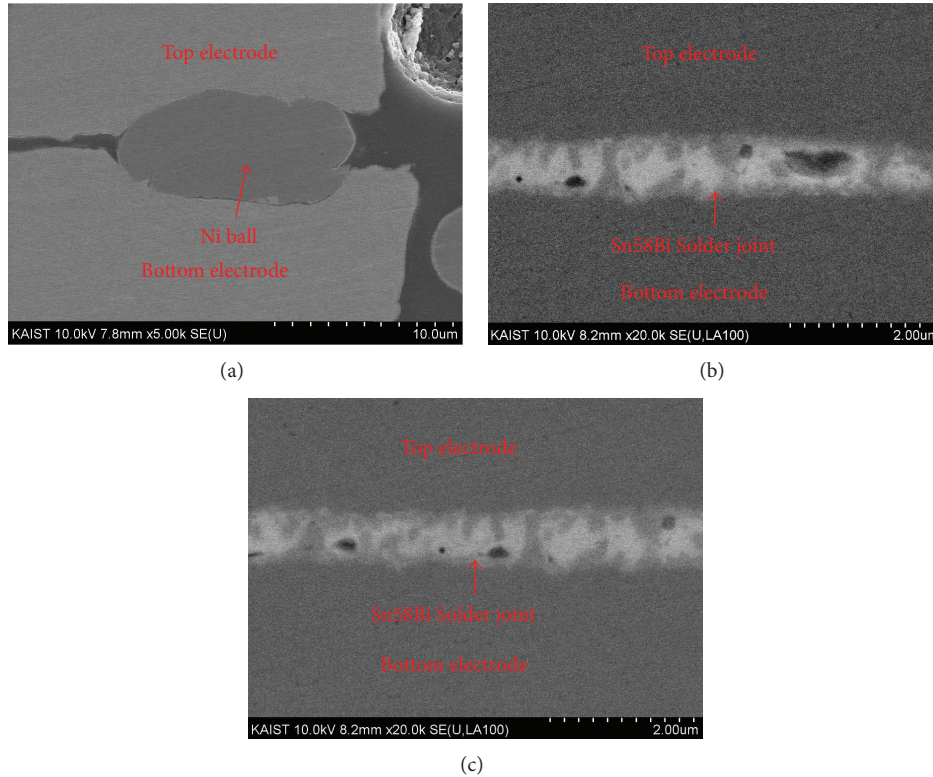


FIGURE 16: The SEM images of solder ball contact joints of (a) conventional Ni ACF joint, (b) conventional Sn58Bi solder ACF joint, and (c) PVDF nanofiber/Sn58Bi solder ACF joint.

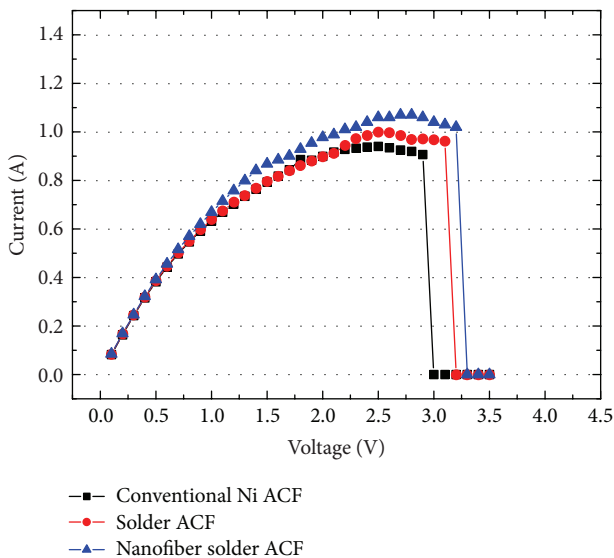


FIGURE 17: The power carrying capability of conventional Ni ACFs, conventional Sn58Bi solder ACFs, and PVDF nanofiber Sn58Bi solder ACFs.

3.4. Reliability Evaluations on Vertical Ultrasonic Bonded ACF Joints

3.4.1. Current Carrying Capability. The current carrying capability results of conventional Ni ACFs, conventional

Sn58Bi solder ACFs, and PVDF nanofiber/Sn58Bi solder ACFs are shown in Figure 17. Conventional Ni ACFs were able to carry 0.94 A at 2.9 volts bias where conventional Sn58Bi solder ACFs and PVDF nanofiber/Sn58Bi solder ACFs were able to carry near 0.99 A and 1.07 A at 3.1 and 3.2 volts bias. For conventional Sn58Bi solder ACFs and PVDF nanofiber/Sn58Bi solder ACFs, higher solder joint contact area was observed resulting higher current carrying capability compared with the conventional Ni ACF. However, the main failure occurred at the FPC line damage rather than the solder joint failure. Still it was shown that PVDF nanofiber Sn58Bi solder ACFs have excellent current carrying capability compared to that of the conventional Ni ACF.

3.4.2. Pressure Cooker Test. Joint stability of the FOF assembly ACF joints was tested by a pressure cooker test (PCT). The pressure cooker test (PCT) results of conventional Ni ACFs, conventional Sn58Bi solder ACFs, and PVDF nanofiber/Sn58Bi solder ACFs are shown in Figure 18. For both Sn58Bi solder ACFs and PVDF nanofiber/Sn58Bi solder ACFs, no open circuits were observed even after 48 hours showing stable joint formation where conventional Ni ACFs showed open circuit even after 16 hours of PCT. This is due to the unstable joint stability of the conventional Ni ACF which forms a physical contact between the Ni ball and the electrodes.

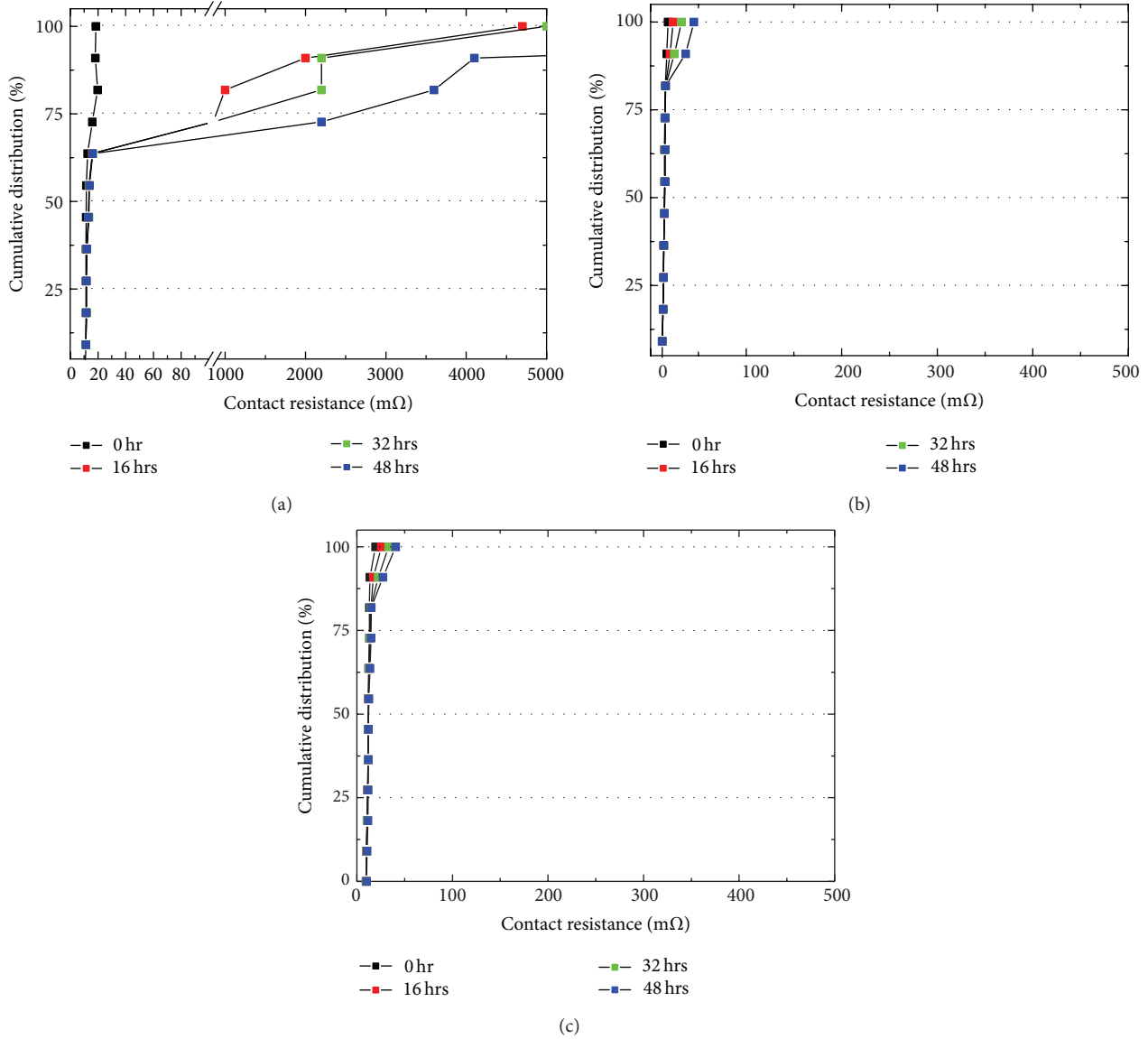


FIGURE 18: Pressure cooker test results of (a) conventional Ni ACFs, (b) conventional Sn58Bi solder ACFs, and (c) PVDF nanofiber/Sn58Bi solder ACFs.

4. Conclusion

Fine pitch flex-on-flex (FOF) assembly was successfully demonstrated using PVDF nanofiber/Sn58Bi solder ACFs and vertical ultrasonic bonding method. By using Sn58Bi solder ball instead of SAC305 solder ball, the bonding temperature was reduced from 250°C to 200°C resulting improved thermal mismatch. When looking at the conductive particle movement analysis after the bonding process, PVDF nanofiber/Sn58Bi solder ACFs showed 33% capture rate improvement compared with the conventional Ni ACFs and conventional Sn58Bi solder ACFs. Also, PVDF nanofiber/Sn58Bi solder ACFs showed 100% insulation property. It is clearly shown that PVDF nanofiber successfully suppresses the conductive solder ball movement and acts as

an insulating layer around the solder ball. When observing the reliability results, conventional Sn58Bi solder ACFs and PVDF nanofiber/Sn58Bi solder ACFs showed preferable reliability results compared to those of conventional Ni ACFs. This is because conventional Sn58Bi solder ACFs and PVDF nanofiber/Sn58Bi solder ACFs contain stable metallurgical solder joints along with the high contact area.

Overall, PVDF nanofiber/Sn58Bi solder ACFs showed excellent solder movement suppressing capability as well as insulation property while lowering the bonding temperature improving the thermal mismatch which eventually improves the electrode misalignment for fine pitch FOF assembly. Currently, the bonding temperature was set to 200°C due to the melting point of the nanofiber polymer material and resin curing. If we select a nanofiber polymer material with a low

melting point (below 150°C) and also use a fast curing resin, it is possible to lower the bonding temperature even down to 150°C. However, more research needs to be done to meet the right mechanical properties and melting temperature of the nanofiber polymer material in order to lower the bonding temperature. This nanofiber solder ACF technology will provide great potential use for future advanced fine pitch electronic assemblies.

References

- [1] C. Beelen-Hendrikx and M. Verguld, "Trends in electronic packaging and assembly for portable consumer products," in *Proceedings of the 3rd Electronics Packaging Technology Conference*, pp. 24–32, December 2000.
- [2] M.-J. Yim and K.-W. Paik, "Design and understanding of anisotropic conductive films (ACF's) for LCD packaging," *IEEE Transactions on Components Packaging and Manufacturing Technology A*, vol. 21, no. 2, pp. 226–234, 1998.
- [3] H. Kristiansen and J. Liu, "Overview of conductive adhesive interconnection technologies for LCD's," *IEEE Transactions on Components Packaging and Manufacturing Technology A*, vol. 21, no. 2, pp. 208–214, 1998.
- [4] J. Liu, A. Tolvgård, J. Malmödin, and Z. Lai, "A reliable and environmentally friendly packaging technology—flip-chip joining using anisotropically conductive adhesive," *IEEE Transactions on Components and Packaging Technologies*, vol. 22, no. 2, pp. 186–190, 1999.
- [5] I. Watanabe, Y. Gotoh, and K. Kobayashi, "Packaging technologies using anisotropic conductive adhesive films in FPDs," in *Proceedings of the 21st International Display Research Conference in Conjunction with the 8th International Display Workshops (Asia Display/IDW '01)*, pp. 553–556, Nagoya, Japan, October 2001.
- [6] P. Savolainen, I. Saarinen, and O. Rusanen, "High-density interconnections in mobile phones using ACF," in *Proceedings of the 4th IEEE International Conference on Polymers and Adhesives in Microelectronics and Photonics*, pp. 99–104, Portland, Ore, USA, September 2004.
- [7] K. Lee, H. J. Kim, I. Kim, and K. W. Paik, "Ultrasonic anisotropic conductive films (ACFs) bonding of flexible substrates on organic rigid boards at room temperature," in *Proceedings of the 57th Electronic Components and Technology Conference (ECTC '07)*, pp. 480–486, Reno, Nev, USA, June 2007.
- [8] K. Lee, I. J. Saarinen, L. Pykari, and K. W. Paik, "High power and high reliability flex-on-board assembly using solder anisotropic conductive films combined with ultrasonic bonding technique," *IEEE Transactions on Components, Packaging and Manufacturing Technology*, vol. 1, no. 12, pp. 1901–1907, 2011.
- [9] M. N. Tolunay, P. R. Dawson, and K. K. Wang, "Heating and bonding mechanisms in ultrasonic welding of thermoplastics," *Polymer Engineering and Science*, vol. 23, no. 13, pp. 726–733, 1983.
- [10] C. J. Nonhof and G. A. Luiten, "Estimates for process conditions during the ultrasonic welding of thermoplastics," *Polymer Engineering and Science*, vol. 36, no. 9, pp. 1177–1183, 1996.
- [11] Y. W. Chiu, Y. C. Chan, and S. M. Lui, "Study of short-circuiting between adjacent joints under electric field effects in fine pitch anisotropic conductive adhesive interconnects," *Microelectronics Reliability*, vol. 42, no. 12, pp. 1945–1951, 2002.
- [12] K. L. Suk, "Effects of nanofiber materials of nanofiber anisotropic conductive adhesives (nanofiber ACAs) for ultra-fine pitch electronic assemblies," in *Proceedings of the 63rd IEEE Electronic Components and Technology Conference*, pp. 118–123, Las Vegas, Nev, USA, May 2013.
- [13] S. H. Lee, K. L. Suk, and K. W. Paik, "Study on fine pitch flex-on-flex assembly using nanofiber/solder anisotropic conductive film and ultrasonic bonding method," *IEEE Transactions on Advanced Packaging*, vol. 2, no. 12, pp. 2108–2114, 2012.
- [14] K. L. Suk, C. K. Chung, and K. W. Paik, "Effects of nanofiber on the electrical properties of anisotropic conductive adhesives (ACAs)," *Journal of Nanoscience and Nanotechnology*, vol. 13, no. 1, pp. 351–355, 2013.
- [15] K. L. Suk, J. H. Han, J. Y. Lee, and K.-W. Paik, "Advancing electronic packaging using microsolder balls: making 25-nm pitch interconnection possible," *IEEE Nanotechnology Magazine*, vol. 7, no. 1, pp. 24–30, 2013.
- [16] Z.-M. Huang, Y.-Z. Zhang, M. Kotaki, and S. Ramakrishna, "A review on polymer nanofibers by electrospinning and their applications in nanocomposites," *Composites Science and Technology*, vol. 63, no. 15, pp. 2223–2253, 2003.
- [17] D. Li and Y. Xia, "Electrospinning of nanofibers: reinventing the wheel?" *Advanced Materials*, vol. 16, no. 14, pp. 1151–1170, 2004.
- [18] K. Gao, X. Hu, C. Dai, and T. Yi, "Crystal structures of electrospun PVDF membranes and its separator application for rechargeable lithium metal cells," *Materials Science and Engineering B*, vol. 131, no. 1–3, pp. 100–105, 2006.
- [19] H. Na, Y. Zhao, X. Liu, C. Zhao, and X. Yuan, "Structure and properties of electrospun poly(vinylidene fluoride)/polycarbonate membranes after hot-press," *Journal of Applied Polymer Science*, vol. 122, no. 2, pp. 774–781, 2011.

Research Article

On the Nature of Electric Current in the Electrospinning Process

Baturalp Yalcinkaya,¹ Fatma Yener,¹ Oldrich Jirsak,¹ and Funda Cengiz-Callioglu²

¹ Department of Nonwovens, Faculty of Textile Engineering, Technical University of Liberec, Studentska 2, 461 17 Liberec, Czech Republic

² Textile Engineering Department, Engineering Faculty, Suleyman Demirel University, Cunur, 32260 Isparta, Turkey

Correspondence should be addressed to Baturalp Yalcinkaya; baturalpyalcinkaya@hotmail.com

Received 8 July 2013; Accepted 23 October 2013

Academic Editor: Tong Lin

Copyright © 2013 Baturalp Yalcinkaya et al. This is an open access article distributed under the Creative Commons Attribution License, which permits unrestricted use, distribution, and reproduction in any medium, provided the original work is properly cited.

The electric currents between electrodes in the electrospinning process are based on the movement of charge carriers through the spinning space. The majority of the charge carriers are formed by ionization of the air close to the metallic needle and to the polymer jet. The salt contained in the polymer solution contributes to the concentration of charge carriers, depending on its amount. The conductivity of polymer jets does not significantly affect the current since the jets do not link the electrodes.

1. Introduction

Electric current was studied across various electrospinning (ES) techniques, namely, in the needle ES [1–14], rod ES [15, 16], and roller ES [17]. In the needle ES, two sorts of experimental arrangement were employed: the “point-plate” geometry [7, 9, 11] and “parallel-plate” geometry [4, 6, 9, 13]. Advantages of the latter geometry are explained in [8]. It mainly consists of an easier interpretation of measured data in the uniform electric field of the parallel-plate spinner.

In the above mentioned works, the dependence of the electric current in the jet on various independent process parameters was studied, such as solution feed, solution conductivity, applied voltage, the diameter of the hollow needle, relative humidity, and some geometrical characteristics. The results of these experiments were formulated in a number of both phenomenological and theoretical equations, such as the dependence of the current in a jet on independent ES parameters [6], as shown in (1) and (2).

The empirical equation (1) says that the current was found to scale as

$$I_{\text{total}} \approx EQ^{0.5}K^{0.4}, \quad (1)$$

where I_{total} is the current flowing through a jet, E is the field strength, Q is the flow rate, and K is the conductivity of the solution. Equation (1) may be applied to various polymer

solutions in nonaqueous solvents. Theoretical Equation (2) describes current I in a jet as

$$I = \pi h^2 KE + \frac{2\sigma Q}{h}, \quad (2)$$

where h is the radius of the jet, K , Q , and E as in (1) above and σ is the surface charge density.

The first term in (2) refers to the conduction current and the second to the advection of the surface charge.

It is the aim of the present work to study the dependence of current on various process parameters in more detail and to explain the results in terms of the mechanism of charge transport.

2. Experimental

In the experimental part, one preliminary test and four groups of experiments were performed as follows.

Preliminary Test. Measurement of changes in the current depending on the measuring device's needle protrusion length.

Group of Experiments 1. Measurement of changes in the current caused by polymer concentration, solution viscosity, solution conductivity, and voltage for both nonaqueous and aqueous polymer solutions.

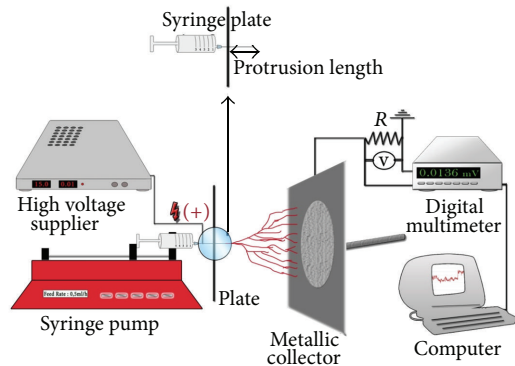


FIGURE 1: The “parallel-plate” spinner.

Because the results showed some discrepancies (see “Section 3”), additional experiments were performed to explain these discrepancies, as follows.

Group of Experiments 2. Measurement of jet length.

Group of Experiments 3. Measurement of the current in the “point-plate” and “parallel-plate” spinners using collectors of various sizes. These measurements were performed with and without polymer solutions.

Group of Experiments 4. Measurement of the current dependent on needle protrusion length, on jet length, and on their sum.

Two polymers and two solvents were used in these experiments to prepare a series of nonaqueous and aqueous solutions. It is known from previous works [6] that the nonaqueous and aqueous solutions show considerably different behaviour in the electrospinning process. The samples in both series differed in polymer concentration, viscosity, and conductivity as follows:

- (1) polyurethane (PU), Larithane LS 1086 produced by Novotex, Italy, dimethylformamide (DMF), purchased from Fluka, and tetraethylammonium bromide (TEAB), purchased from Fluka;
- (2) poly(ethylene oxide) (PEO), mol. weight 400,000 Da, purchased from Scientific Polymer Products, distilled water, and TEAB (as above).

The electric conductivity of the solutions was measured using a Radelkis OK-102/1 conductivity meter and the zero-shear viscosity was measured using a HAAKE Roto Visco rheometer at 25°C. The list of samples, including their conductivities and viscosities, is shown in Table 1 through 4.

The solutions were electrospun in the “parallel-plate” spinner (Figure 1). The parallel plates were made of steel, with a diameter of 280 mm. In a “parallel-plate” spinner, the needle penetrates through a small orifice in one plate. It is in contact with the plate so that the plate is charged to the same potential as the needle. The distance between the tip of the needle and the charged plate is called the “needle protrusion length.”

In the preliminary test, the current was measured as a function of the protrusion length. The protrusion of the

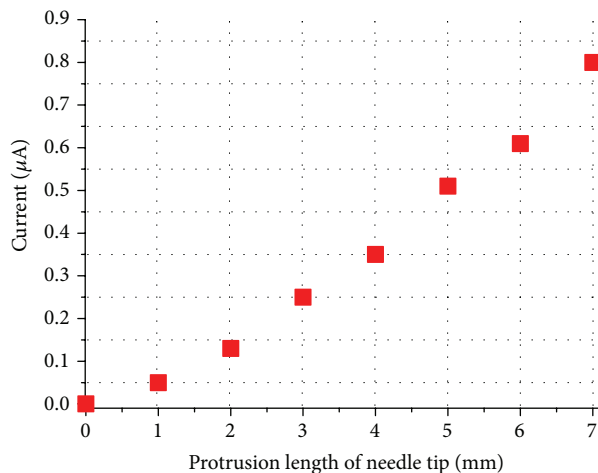


FIGURE 2: Dependence of the current on needle protrusion length in the “parallel-plate” spinner (the value of the current in the corresponding “point-plate” spinner, 20 μA , is not shown in Figure 2).

needle from the charged plate was mentioned by Shin et al. [4] and Fallahi et al. [10] as an important parameter of the spinner, and its effect on the current was found to be rather strong in the study of Shin et al. [4] and Yener et al. [17]. The dependence of the current on the protrusion length can be seen as a characteristic of the spinner. It was measured in the following conditions: polymer solution: 20% PU in DMF + 1.27% TEAB, feed rate of 0.5 mL/hour, voltage of 35 kV, and a distance of 105 mm between the tip of the needle and the collector. During the experiment, the protrusion length was increased from 0 to 7 mm and the charged plate was then removed so that the device was converted from “parallel-plate” to “point-plate” geometry. In “parallel-plate” geometry, the current grew with increasing protrusion length (Figure 2) from a value close to zero to ca. 0.7 μA . After the charged plate had been removed, the value of the current jumped to 20 μA (not shown in Figure 2).

In the first group of experiments, the current was measured as a function of various independent parameters. The results are shown in Tables 4 and 5.

The spinning conditions were based on previous results so that nanofibers of a good quality were produced in all of the experiments: a protruding length of 7 mm, an outer needle diameter of 0.6 mm, and a feed rate of 0.5 mL/hour. Some other conditions, such as polymer concentrations and the distance between the tip of the needle and the collector plate, were different for PU and PEO solutions (see below). During the spinning process, the current was measured and the data were stored in a computer as described in [17].

In the second group of experiments, the length of the jets (Figure 3) was measured using the photographic records. A Sony Full HD NEX-VG10E Handy cam (14.2 megapixels)-E18-200 mm Lens camera was used in the experiments. The results are shown in Tables 7 and 8.

In the third group of experiments, the current between the tip of the needle and the collector was measured as follows:

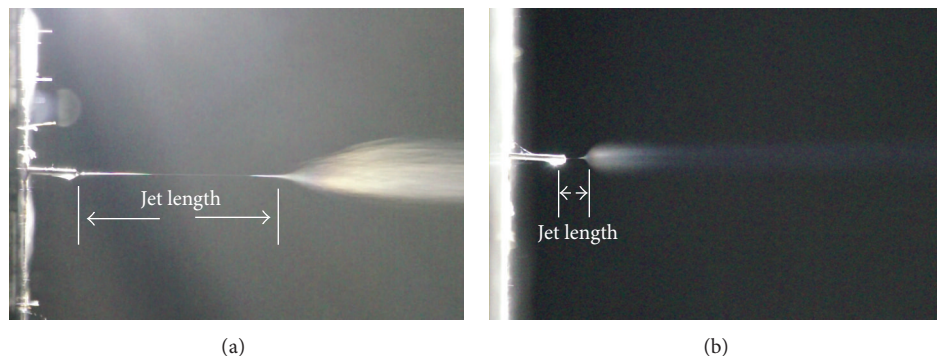


FIGURE 3: Photographic records of the polymer jet: (a) 20% PU, 35 kV and (b) 15% PU + 1.27% TEAB, 35 kV.

- (i) in both “parallel-plate” and “point plate” spinners,
- (ii) with four collector electrodes differing from each other in size, namely,
 - (a) diameter of 280 mm (area 61,600 mm²),
 - (b) diameter of 80 mm (area 5,000 mm²),
 - (c) diameter of 10 mm (area 78.5 mm²),
 - (d) diameter of 2.5 mm (area 4.9 mm²).

The experiments were variously carried out using the following:

- (i) a low conductive solution (17.5% PU, conductivity 0.04 mS/cm),
- (ii) a high conductive solution (17.5% PU + 1.27% TEAB, conductivity 1.6 mS/cm),
- (iii) no solution,
- (iv) three different values of voltages being applied: 25, 27.5, and 30 kV,
- (v) the distance from the tip of the needle to the collector being 105 mm,
- (vi) the solution feed being 0.5 mL/hour.

The results of these experiments are shown in Tables 9 and 10.

In the fourth group of experiments, the current was measured at various values of needle protrusion length. The length of jets was also measured as described above. The results are shown in Tables 11 and 12 and in Figures 7–11.

3. Results and Discussion

In the preliminary test, the dependence of the current on the “needle protrusion length” (Figure 2) was found to be rather strong. At the zero protrusion length, which can be understood as “pure” parallel-plate geometry, spinning hardly occurs and the current is close to zero. On the other hand, an extremely high protrusion length (represented by the point-plate geometry) exhibited currents as high as 20 μ A. Thus, the dependence of the current on the “needle protrusion length” seems to be good characteristic of needle electrospinning devices.

TABLE 1: Samples of PU solutions and their conductivity.

Concentration of PU (%)	Conductivity (mS/cm)			
	Concentration of TEAB (%)			
	0	0.4	0.8	1.27
15	0.046	0.672	1.188	1.72
17.5	0.04	0.58	1.044	1.6
20	0.038	0.46	0.892	1.38

TABLE 2: Samples of PU solutions and their zero-shear viscosity.

Concentration of PU (%)	Viscosity (Pa·s)			
	Concentration of TEAB (%)			
	0	0.4	0.8	1.27
15	0.493	0.492	0.514	0.536
17.5	1.062	1.017	1.141	1.143
20	2.159	2.354	2.599	2.642

A list of the polymer solutions used in these experiments and their basic properties is shown in the following tables.

Tables 1 and 2 illustrate PU solutions in DMF containing 15, 17.5, and 20 weight percent of polymer and 0, 0.4, 0.8, and 1.27 weight percent of TEAB. Tables 3(a) and 3(b) show PEO solutions in water containing 3, 4, 5, and 6 weight percent of polymer and 0 or 1 weight percent of TEAB.

The data in Tables 1–3 shows anticipated facts, namely, the following:

- (i) the conductivity of solutions grows with the salt content;
- (ii) the conductivity of solutions containing salt falls when viscosity increases;
- (iii) the viscosity of solutions increases with an increase in polymer concentration;
- (iv) the viscosity of solutions is only moderately influenced by the salt content.

The results of the first group of experiments, the values of the current measured during the spinning at various levels of voltage are shown in Tables 4 and 5.

TABLE 3: Samples of PEO solutions and their conductivity and viscosity.

(a)	
Solutions (%) PEO + TEAB	Conductivity (mS/cm)
3 + 0	0.17
4 + 0	0.18
5 + 0	0.19
3 + 1	4.88
4 + 1	4.60
5 + 1	4.28
6 + 1	4.16

(b)	
Solutions (%) PEO + TEAB	Viscosity (Pa.s)
3 + 0	0.062
4 + 0	0.118
5 + 0	0.233
3 + 1	0.046
4 + 1	0.117
5 + 1	0.212
6 + 1	0.332

TABLE 4: Current during spinning of PU solutions. Distance between tip of needle and collector: 105 mm.

Solutions (%) PU + TEAB	Current (μA) Voltages (kV)				
	25	27.5	30	32.5	35
15 + 0	0	0.039	0.081	0.11	0.14
15 + 0.4	0.025	0.071	0.11	0.13	0.22
15 + 0.8	0.050	0.076	0.12	0.20	0.30
15 + 1.27	0.12	0.21	0.33	0.48	0.55
17.5 + 0	0.019	0.061	0.11	0.13	0.18
17.5 + 0.4	0.089	0.13	0.20	0.33	0.42
17.5 + 0.8	0.10	0.17	0.22	0.40	0.56
17.5 + 1.27	0.15	0.22	0.39	0.56	0.79
20 + 0	0.025	0.091	0.13	0.16	0.20
20 + 0.4	0.10	0.16	0.23	0.36	0.53
20 + 0.8	0.11	0.19	0.29	0.41	0.76
20 + 1.27	0.17	0.27	0.42	0.69	0.91

Note that the electrospinning process and the current between electrodes can be influenced by the electric resistance of the electrospun nanofiber layer and/or take-up fabric depending on their thickness and resistivity. The presented experiments have been conducted in a relatively short time; therefore, the resistances were negligible.

The values of the currents in Tables 4 and 5 show some unexpected relationships (a)–(c) as follows.

TABLE 5: Current during spinning of PEO solutions. Distance between tip of needle and collector: 150 mm.

Solutions (%) PEO + TEAB	Current (μA) Voltages (kV)				
	25	27.5	30	32.5	35
3 + 0	0.38	0.55	0.72	0.92	1.33
4 + 0	0.21	0.29	0.43	0.51	0.66
5 + 0	0.15	0.25	0.35	0.44	0.59
3 + 1	1.28	1.63	1.80	2.26	2.57
4 + 1	1.57	1.76	2.14	2.46	2.70
5 + 1	1.73	2.00	2.38	2.68	3.03
6 + 1	1.87	2.30	2.62	3.13	3.86

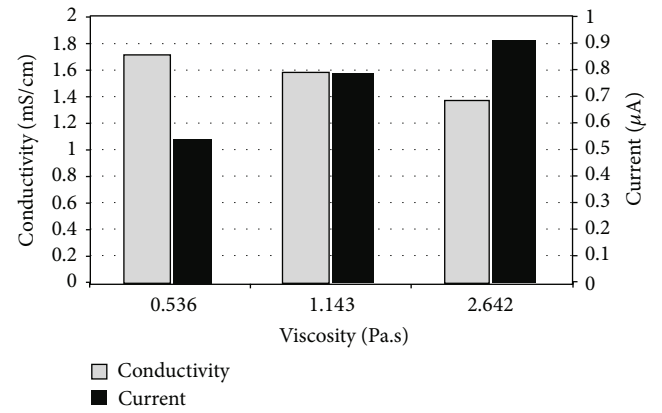


FIGURE 4: Dependence of solution conductivity and measured current in ES on solution viscosity. Solutions: PU 15, 17.5, and 20%, all containing 1.27% of TEAB.

- (a) The electric conductivity of all solutions containing salt decreases as viscosity/polymer concentration increases. This is easy to explain given the lower mobility of ions in more viscous solutions. In contrast, the current measured during the ES process grew with increasing viscosity. This was observed at all the values of voltage and salt content (in the PU solutions), in both the aqueous and nonaqueous solutions, and is in conflict with (1) and (2).

To make the situation more comprehensible for readers, Figure 4 gives a representation of the unexpected relations.

- (b) The growth of the measured current in proportion to the applied voltage is much steeper than that predicted by (1) and (2).
- (c) The calculation of the current from (2) yields much larger values than those measured experimentally.

Since it is difficult to estimate the surface charge density σ in (2), we have calculated the current from the first part of (2) only as follows:

$$I = \pi h^2 KE. \quad (3)$$

TABLE 6: Values of current (in μS) calculated from (3).

Conductivity of solution (mS/cm)	Current (μA) Jet diameter $2h$ (mm)		
	0.5	0.2	0.1
0.05	98	15.7	3.92
0.1	196	31.4	7.85
0.2	392	62.8	15.7
0.5	980	157	39.2
1	1960	314	78.5
5	9800	1570	392

TABLE 7: Length of jets, polyurethane solutions.

Solutions (%) PU + TEAB	Jet length (mm)				
	Voltages (kV)				
	25	27.5	30	32.5	35
15 + 0		3.69	5.11	5.60	6.15
15 + 0.4	1.55	1.51	1.52	1.76	1.99
15 + 0.8	1.30	1.43	1.32	1.50	1.67
15 + 1.27	1.00	1.10	1.27	1.30	1.56
17.5 + 0	4.63	5.45	7.16	13.46	15.68
17.5 + 0.4	3.07	2.74	2.69	2.58	3.60
17.5 + 0.8	2.81	2.67	2.60	2.62	2.68
17.5 + 1.27	3.02	2.82	2.80	2.27	2.68
20 + 0	5.90	8.08	8.13	15.67	18.42
20 + 0.4	3.30	3.01	3.48	3.50	4.14
20 + 0.8	3.08	2.95	2.73	2.67	3.45
20 + 1.27	3.30	2.95	2.90	2.77	2.98

TABLE 8: Length of jets, PEO solutions.

Solutions (%) PEO + TEAB	Jet length (mm)				
	Voltages (kV)				
	25	27.5	30	32.5	35
3 + 0	21.32	22.33	22.32	22.31	21.29
4 + 0	26.55	28.04	30.67	28.75	35.00
5 + 0	51.36	54.38	54.81	51.92	57.47
3 + 1	20.14	19.75	22.46	17.71	20.98
4 + 1	22.51	21.63	21.36	20.94	22.18
5 + 1	32.79	30.99	33.88	38.92	32.20
6 + 1	35.24	34.67	37.54	40.30	39.42

For this calculation, the jets were approximated by a cylinder of diameter $2h$. According to the data in the literature [8] as well as to our own measurements, the jet diameter can be estimated as being between 0.1 and 0.5 mm. Therefore, the current was calculated for jet diameters of 0.1, 0.2, and 0.5 mm.

The conductivities of the solutions were chosen as follows: 0.05, 0.1, 0.5, 1, and 5 mS/cm; these were chosen to correspond to the values in Tables 1 and 3. A value of 100 000 V/m was

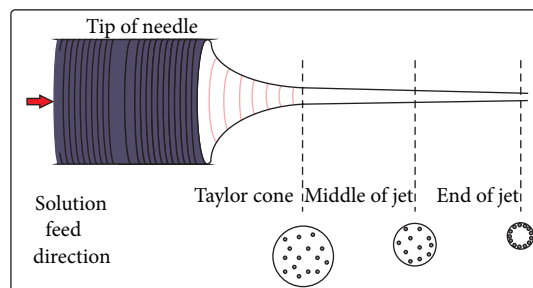


FIGURE 5: Radial movement of ions in a jet.

given for E . The calculated values of the current are shown in Table 6.

The values of the current in Table 6 are significantly larger than the experimental values, corresponding to solutions of similar conductivities in Tables 4 and 5. The difference amounts to approximately 3 decimal orders.

Further measurements carried out within the second group of experiments were inspired by the Ph.D. thesis of Dao [18], who measured the length of jets and their dependence on various spinning parameters, the viscosity of polymer solutions, among others. The results of the measurements are given in Tables 7 and 8.

The results in Tables 7 and 8 can be summarized as follows:

- (i) very short (1 mm) as well as very long (60 mm) jets were observed and the measurements are well reproducible;
- (ii) the length of the jets does not depend on the applied voltage except in cases of very low salt content or low conductivity (observed at PU only);
- (iii) the length of the jets decreases with increased salt content (observed at PU, but not measured at PEO);
- (iv) the length of the jets significantly increases with growing solution viscosity.

Dao [18] offered the following interpretation of the above dependencies: in the polymer solutions, ions are randomly distributed in bulk. In the jet, due to repulsive forces, ions move radially toward the jet surface. The velocity of the movement is limited by the solution's viscosity. When the concentration of ions at the jet surface reaches a critical value, the jet is converted into nanofibers via whipping instability and/or splitting. Thus, low viscosity and high salt content help to create critical ions concentration in less time, which leads to shorter jets (shown in Figure 5). Nevertheless, neither Dao's theory nor the presented experiments offer an explanation for the substantial difference between the PU and PEO jet lengths.

Let us go back now to unexpected relationships (a)–(c) mentioned previously. Two attempts have been made to explain the measured data.

The first attempt was based on the model shown in Figure 6. In the model, the space between the tip of the needle and the collector electrode consists of two sub-spaces,

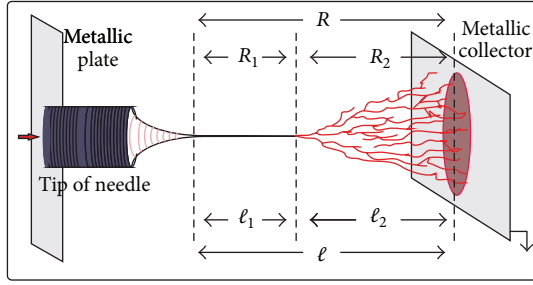


FIGURE 6: Model of spinning space.

namely, of jet sub-space and fibers sub-space. The size of the space is expressed as

$$\ell = \ell_1 + \ell_2, \quad (4)$$

where ℓ_1 is the length of the jet sub-space and ℓ_2 is the length of the fibers sub-space. Electric resistance of the space is found by the following equation:

$$R = R_1 + R_2 = \rho_1 \ell_1 + \rho_2 \ell_2, \quad (5)$$

where ρ_1 and ρ_2 are resistivities in (Ωm^{-1}) of both sub-spaces. Let us suppose that resistivity ρ_1 depends on the conductivity and diameter of the jet according to (3). The resistivity of the fiber sub-space ρ_2 is connected to the transport of charges with polymer fibers, salt molecules, and ions, evaporated solvent, and plasma particles created in the strong electric field and is probably much greater than ρ_1 . Therefore, longer jets lead to shorter ℓ_2 , smaller R_2 , smaller total resistance R , and a greater current.

The total resistance R was calculated using Ohm's law and R_1 from the solution conductivity, length, and diameter of the jet. The same jet diameters of 0.2 mm were used in the calculations for all of the jets and then, the values of R_2 , ρ_1 , and ρ_2 were calculated using (4) and (5).

An example of calculation is as follows.

Data: voltage $U = 10^4$ V, current $I = 1 \mu\text{A}$, solution conductivity $K = 1 \text{ mS cm}^{-1} = 0.1 \text{ S m}^{-1}$, $l = 100$ mm, $l_1 = 10$ mm, $l_2 = 90$ mm, and jet radius $h = 0.1$ mm.

Then, one has the following:

total conduction of spinning space $R = U/I = 10^{10} \Omega$,

conduction of the jet $K_1 = K \times \pi h^2 / l_1 = \pi \times 10^{-7} \text{ S}$,

resistance of the jet $R_1 = 1/K_1 = 3.2 \times 10^6 \Omega$,

resistance of fiber space $R_2 = R - R_1 = 0.99968 \times 10^{10} \Omega$,

resistivities: $\rho_1 = 3.2 \times 10^8 \Omega\text{m}^{-1}$, $\rho_2 = 1.111 \times 10^{11} \Omega\text{m}^{-1}$.

The calculations did not support the model in Figure 6. The following results were observed.

- (i) The resistances R_2 amounted to $3\text{--}200 \times 10^9$ Ohms for the sample solutions taken into experiments. Compared to that, the calculated jet resistances R_1 were

TABLE 9: Current (μA) in the “parallel-plate” spinner.

Solutions	Collector diameter (mm)	Current (μA)		
		Voltages (kV)		
		25	27.5	30
No solution	280	0	0	0
	80	0	0	0
	10	0	0	0
	2.5	0	0	0
Low conducting 17.5% PU 0.04 mS/cm	280	0.019	0.061	0.110
	80	0.014	0.041	0.072
	10	0.009	0.032	0.054
	2.5	0	0.648	2.035
High conducting 17.5% PU + 1.27% TEAB 1.6 mS/cm	280	0.150	0.222	0.395
	80	0.106	0.174	0.334
	10	0.070	0.119	0.297
	2.5	1.613	2.359	3.126

found to be 4 to 6 decimal orders smaller ($0.2\text{--}4 \times 10^6$ Ohms) so that total resistance R is almost equal to R_1 . This also justifies the use of a single value for the jet diameter—0.2 mm—in the calculations: the values of R_2 would be almost the same if the diameter was plus or minus one decimal order.

- (ii) The values of ρ_1 and ρ_2 were expected to be constant in the groups of solutions containing the same polymer and equal concentration of salt. As the calculations revealed, this was not the case. The differences in total resistances (and current) cannot be explained by different lengths of relatively high conductive jets.

In the second attempt to explain the above discrepancies, the role of plasma particles was studied. The plasma particles generated by the ionization of air in a strong electric field move between electrodes (through both jet sub-space and fibers sub-space as seen in Figure 6) and serve as charge carriers, contributing to the total electric current. Plasma particles can be formed at the collector electrode if it is small enough as well as at the tip of the needle and the polymer jet, depending on the needle protrusion length and jet length. To evaluate the effect of plasma particles, the third and fourth group of experiments were performed.

The third group of experiments consisted of spinning, using collector electrodes of various diameters. The parameters of the experiments are described in the experimental section. The results are shown in Tables 9 and 10.

The results in Tables 9 and 10 show the following.

- (i) The values of the current are considerably larger in the “point-plate” spinner than in the “parallel-plate” spinner. This is due to the high intensity of the electric field at the tip of the needle, which leads to the formation of additional plasma particles as charge carriers.
- (ii) In the “parallel-plate” spinner, plasma particles are formed with the collector of the smallest diameter

TABLE 10: Current (μA) in the “point-plate” spinner.

Solutions	Collector diameter (mm)	Current (μA)		
		Voltages (kV)		
		25	27.5	30
No solution	280	5.40	7.33	8.86
	80	5.19	7.15	8.61
	10	2.03	2.54	3.46
	2.5	8.63	12.02	16.30
Low conducting 17.5% PU 0.04 mS/cm	280	7.04	10.40	15.52
	80	4.94	6.94	8.05
	10	2.71	3.48	4.71
	2.5	5.53	6.92	11.85
High conducting 17.5% PU + 1.27% TEAB 1.6 mS/cm	280	7.79	12.63	16.59
	80	5.53	6.97	9.08
	10	3.25	4.14	8.77
	2.5	8.75	12.06	15.34

TABLE 11: Dependence of the current on needle protrusion length and jet length in PU solutions.

Solutions (%) PU + TEAB	Protrusion length (mm)	Jet length (mm)	Protrusion length + jet length (mm)	Average current (μA)
15 + 1.27	0	0	0	0
	2	0	2	0
	4	1.62	5.62	0.101
	6	1.43	7.43	0.255
	8	1.29	9.29	0.763
	10	1.22	11.22	1.117
	12	0.98	12.98	1.452
17.5 + 1.27	0	0	0	0
	2	5.02	7.02	0.113
	4	4.17	8.17	0.295
	6	2.91	8.91	0.573
	8	2.92	10.92	1.019
	10	2.95	12.95	1.418
	12	2.81	14.81	1.667
20 + 1.27	0	0	0	0
	2	5.71	7.71	0.226
	4	4.36	8.36	0.444
	6	3.08	9.08	0.718
	8	3.11	11.11	1.172
	10	3.01	13.01	1.561
	12	3.01	15.01	1.840

(2.5 mm) only. This yields the highest values of current when compared with the other collectors. The smallest collector increases current even in the “point-plate” spinner.

TABLE 12: Dependence of the current on needle protrusion length and jet length in PEO solutions.

Solutions (%) PEO + TEAB	Protrusion length (mm)	Jet length (mm)	Protrusion length + jet length (mm)	Average current (μA)
3 + 1	0	0	0	0
	2	22.38	24.38	0.582
	4	21.56	25.56	0.611
	6	20.15	26.15	1.668
	8	19.23	27.23	2.104
	10	17.88	27.88	2.445
4 + 1	12	17.51	29.51	3.240
	0	0	0	0
	2	31.76	33.76	0.558
	4	30.54	34.54	1.391
	6	29.12	35.12	1.913
	8	27.37	35.37	2.310
5 + 1	10	26.23	36.23	2.874
	12	24.43	36.43	3.859
	0	0	0	0
	2	37.83	39.83	0.682
	4	36.94	40.94	1.732
	6	36.91	42.91	2.069
6 + 1	8	36.22	44.22	2.586
	10	35.47	45.47	3.279
	12	33.99	45.99	4.130
	0	0	0	0
	2	47.29	49.29	1.375
	4	46.42	50.42	2.140
6 + 1	6	45.88	51.88	2.590
	8	45.84	53.84	3.045
	10	44.37	54.37	3.672
	12	42.83	54.83	4.566

(iii) Plasma particles are not formed at collectors with 10 mm diameters and larger.

(iv) With these larger collectors, the current increases with the increasing collector diameter due to the increased area for charge carriers to move in the cone between the needle tip and collector. Thus, a greater collector diameter makes the resistance R_2 smaller.

The process of the air ionization and formation of plasma particles in the strong electric field has been studied and described by many authors [19–22]. To explain the role of needle protrusion length and jet length in forming plasma particles, current and length of jets were measured in the fourth group of experiments. Needle protrusion length was an independent parameter in the experiments.

Note: it is obvious from Tables 11 and 12 that an increase in the needle protrusion length leads to a shorter jet length. This

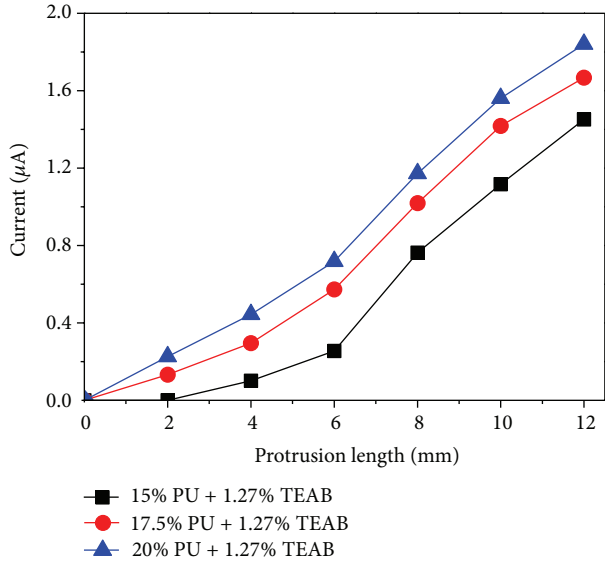


FIGURE 7: Dependence of current on needle protrusion length in PU solutions.

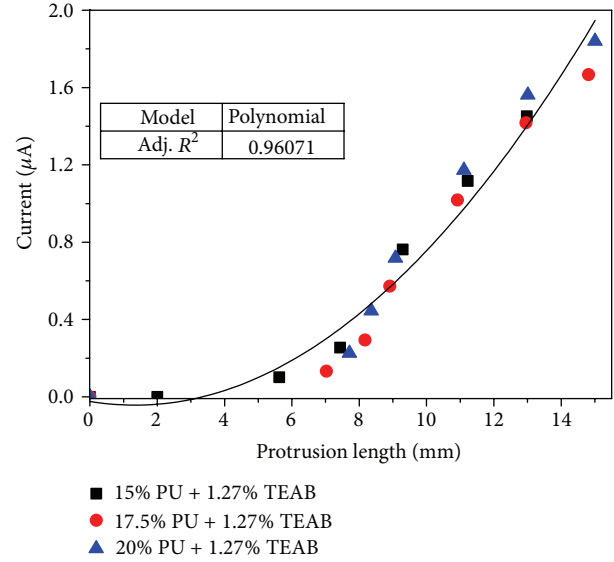


FIGURE 9: Dependence of current on the sum of needle protrusion length and jet length in PU solutions.

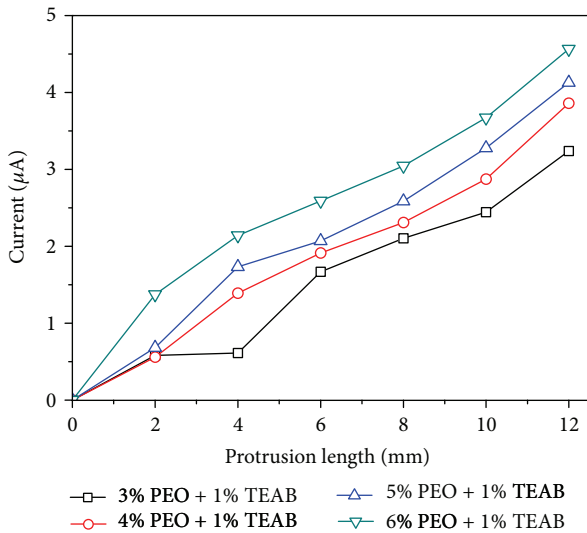


FIGURE 8: Dependence of current on needle protrusion length in PEO solutions.

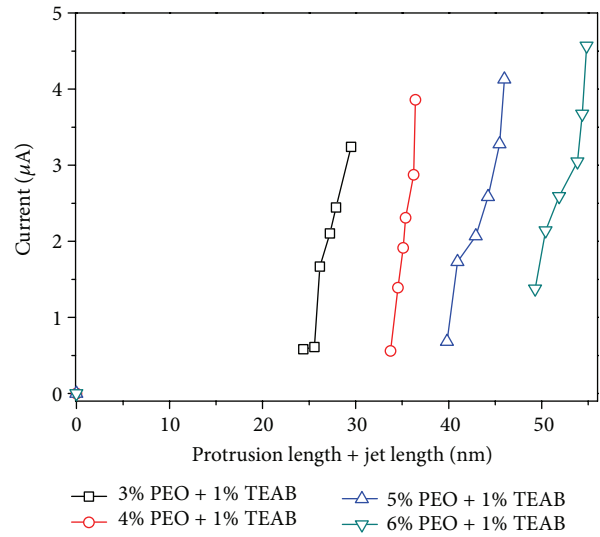


FIGURE 10: Dependence of current on the sum of needle protrusion length and jet length in PEO solutions.

is caused by the deformation of the electric field in the vicinity of highly conductive needle and resultant smaller elongation of the jet.

The results, shown in Tables 11 and 12 and in Figures 7 and 8, indicate that both needle protrusion length and jet length contribute to an increase in the current. Therefore, the current is plotted against the sum of the protruding length and the jet length in Figures 9 and 10.

The graphs in Figures 9 and 10 show significant differences in the behaviour between PU and PEO solutions. PU solutions create short (1–6 mm) jets and the current depends on the sum of the protrusion length and the jet length. Conversely, PEO solutions create much longer (17–48 mm)

jets, and the effect of the jet length on the formation of plasma particles is less than that of the needle protrusion length.

To evaluate the role of jet length in PEO solutions relative to that of needle protrusion length, the current was plotted against the value of the protrusion length + ($N \times$ jet length). The optimum value of coefficient $N = 0.16$ was found based on the correlation coefficient in the polynomial model for the above relation—see Figure 11.

4. Conclusions

The results of the experiments show that the value of the electric current in the electrospinning process is mainly based

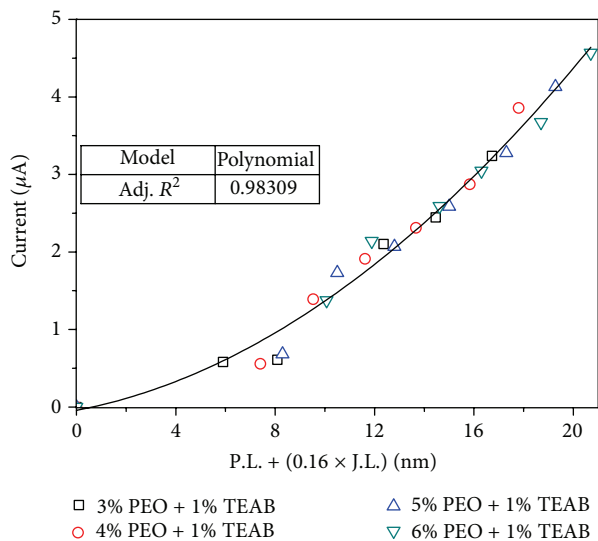


FIGURE 11: Dependence of current on protrusion length + ($N \times$ jet length), $N = 0.16$ in PEO solutions.

on the movement of charge carriers between the spinning and collector electrodes. The charge carriers are mainly formed by the ionization of air in the vicinity of small objects, such as the protruding part of the needle, a jet, or a collector electrode, provided it is small enough. The number of charge carriers depends on the strength of the electric field, that is, on the voltage applied and the size of electrodes. The salts contained in polymer solutions are another source of charge carriers. Nevertheless, the plasma particles formed by the ionization of air are the dominant source of charge carriers. As the data in Table 10 show, a rather strong current can be observed between the electrodes even without any feed of polymer solution. Charge carriers move between the electrodes through the “sub-spaces” shown in Figure 6. Thus, the idea of the total resistance of spinning space R as a sum of R_1 and R_2 is not relevant to the explanation of the nature of the electric current.

The plasma particles moving between the electrodes create the effect known as “electric wind.” This effect can be stopped by a sheet of paper.

Equation (1), describing the experimentally found dependence of current on E , Q , and K , is in agreement with our experiments: increasing E enhances the ionization process considerably, while increasing Q and K is linked with greater amounts of salts as a source of charge carriers.

On the other hand, (2) describes the conductivity of the jet itself, which has no relation to the total current measured during the electrospinning process.

5. Future Work

Further research may be conducted on some particular points, including the following:

- (i) the effect of specific polymers, solvents, and salts on the length of jets;

- (ii) the effect of the same variables on the ionization of air;
- (iii) the effect of jet length on the ionization of air and so forth;
- (iv) the effect of environmental conditions on the current.

Acknowledgment

The authors are thankful for the Ministry of Education, Youth, and Sports of the Czech Republic (student’s grant competition TUL in specific university research in 2012, Project no. 4866, and 2013, Project no. 48004) for their financial support.

References

- [1] M. M. Hohman, M. Shin, G. Rutledge, and M. P. Brenner, “Electrospinning and electrically forced jets. I. Stability theory,” *Physics of Fluids*, vol. 13, no. 8, pp. 2201–2220, 2001.
- [2] M. M. Hohman, M. Shin, G. Rutledge, and M. P. Brenner, “Electrospinning and electrically forced jets. II. Applications,” *Physics of Fluids*, vol. 13, no. 8, pp. 2221–2236, 2001.
- [3] Y. M. Shin, M. M. Hohman, M. P. Brenner, and G. C. Rutledge, “Electrospinning: a whipping fluid jet generates submicron polymer fibers,” *Applied Physics Letters*, vol. 78, no. 8, pp. 1149–1151, 2001.
- [4] Y. M. Shin, M. M. Hohman, M. P. Brenner, and G. C. Rutledge, “Experimental characterization of electrospinning: the electrically forced jet and instabilities,” *Polymer*, vol. 42, no. 25, pp. 9955–9967, 2001.
- [5] S. J. Kim, C. K. Lee, and S. I. Kim, “Effect of ionic salts on the processing of poly(2-acrylamido-2-methyl-1-propane sulfonic acid) nanofibers,” *Journal of Applied Polymer Science*, vol. 96, no. 4, pp. 1388–1393, 2005.
- [6] P. K. Bhattacharjee, T. M. Schneider, M. P. Brenner, G. H. McKinley, and G. C. Rutledge, “On the measured current in electrospinning,” *Journal of Applied Physics*, vol. 107, no. 4, Article ID 044306, pp. 1–8, 2010.
- [7] J. M. Deitzel, J. Kleinmeyer, D. Harris, and N. C. B. Tan, “The effect of processing variables on the morphology of electrospun nanofibers and textiles,” *Polymer*, vol. 42, no. 1, pp. 261–272, 2001.
- [8] D. Fallahi, M. Rafizadeh, N. Mohammadi, and B. Vahidi, “Effects of feed rate and solution conductivity on jet current and fiber diameter in electrospinning of polyacrylonitrile solutions,” *E-Polymers*, vol. 9, no. 1, pp. 1250–1257, 2013.
- [9] R. Samatham and K. J. Kim, “Electric current as a control variable in the electrospinning process,” *Polymer Engineering & Science*, vol. 46, no. 7, pp. 954–959, 2006.
- [10] D. Fallahi, M. Rafizadeh, N. Mohammadi, and B. Vahidi, “Effect of applied voltage on jet electric current and flow rate in electrospinning of polyacrylonitrile solutions,” *Polymer International*, vol. 57, no. 12, pp. 1363–1368, 2008.
- [11] M. M. Demir, I. Yilgor, E. Yilgor, and B. Erman, “Electrospinning of polyurethane fibers,” *Polymer*, vol. 43, no. 11, pp. 3303–3309, 2002.
- [12] S. A. Theron, E. Zussman, and A. L. Yarin, “Experimental investigation of the governing parameters in the electrospinning of polymer solutions,” *Polymer*, vol. 45, no. 6, pp. 2017–2030, 2004.

- [13] D. Fallahi, M. Rafizadeh, N. Mohammadi, and B. Vahidi, "Effect of applied voltage on surface and volume charge density of the jet in electrospinning of polyacrylonitrile solutions," *Polymer Engineering & Science*, vol. 50, no. 7, pp. 1372–1376, 2010.
- [14] M. M. Munir, F. Iskandar, K. Khairurrijal, and K. Okuyama, "A constant-current electrospinning system for production of high quality nanofibers," *Review of Scientific Instruments*, vol. 79, no. 9, Article ID 093904, 2008.
- [15] P. Pokorný, P. Mikes, and D. Lukas, "Measurement of electric current in liquid jet," in *Proceedings of the Nanocon International Conference*, pp. 12–14, Olomouc, Czech Republic, October 2010.
- [16] F. Cengiz-Callioğlu, O. Jirsak, and M. Dayik, "Electric current in polymer solution jet and spinnability in the needleless electrospinning process," *Fibers and Polymers*, vol. 13, no. 10, pp. 1266–1271, 2012.
- [17] F. Yener, B. Yalcinkaya, and O. Jirsak, "On the measured current in needle and needleless electrospinning," *Journal of Nanoscience and Nanotechnology*, vol. 13, no. 7, pp. 4672–4679, 2013.
- [18] A. T. Dao, *The role of rheological properties of polymer solutions in needleless electrostatic spinning [Ph.D. thesis]*, Department of Nonwovens, Technical University of Liberec, Liberec, Czech Republic, 2010.
- [19] J. J. Lowke and R. Morrow, "Theory of electric corona including the role of plasma chemistry," *Pure & Applied Chemistry*, vol. 66, no. 6, pp. 1287–1294, 1994.
- [20] G. F. L. Ferreira, O. N. Oliveira Jr., and J. A. Giacometti, "Point-to-plane corona: current-voltage characteristics for positive and negative polarity with evidence of an electronic component," *Journal of Applied Physics*, vol. 59, no. 9, pp. 3045–3049, 1986.
- [21] A. Jaworek and A. Krupa, "Corona discharge from a multipoint electrode in flowing air," *Journal of Electrostatics*, vol. 38, no. 3, pp. 187–197, 1996.
- [22] V. E. Kalayci, P. K. Patra, Y. K. Kim, S. C. Ugbohue, and S. B. Warner, "Charge consequences in electrospun polyacrylonitrile (PAN) nanofibers," *Polymer*, vol. 46, no. 18, pp. 7191–7200, 2005.

Research Article

Improved Methane Sensing Properties of Co-Doped SnO₂ Electrospun Nanofibers

Weigen Chen,¹ Qu Zhou,¹ Lingna Xu,¹ Fu Wan,¹ Shudi Peng,² and Wen Zeng^{1,3}

¹ State Key Laboratory of Power Transmission Equipment & System Security and New Technology, Chongqing University, Chongqing 400030, China

² Chongqing Electric Power Research Institute, Chongqing 401123, China

³ College of Materials Science and Engineering, Chongqing University, Chongqing 400030, China

Correspondence should be addressed to Weigen Chen; weigench@cqu.edu.cn and Qu Zhou; zhouqu@cqu.edu.cn

Received 11 July 2013; Revised 23 September 2013; Accepted 7 October 2013

Academic Editor: Gajanan S. Bhat

Copyright © 2013 Weigen Chen et al. This is an open access article distributed under the Creative Commons Attribution License, which permits unrestricted use, distribution, and reproduction in any medium, provided the original work is properly cited.

Co-doped SnO₂ nanofibers were successfully synthesized via electrospinning method, and Co-doped SnO₂ nanospheres were also prepared with traditional hydrothermal synthesis route for comparison. The synthesized SnO₂ nanostructures were characterized by X-ray powder diffraction, scanning electron microscopy, transmission electron microscopy, energy dispersive X-ray spectroscopy, and X-ray photoelectron spectra. Planar-type chemical gas sensors were fabricated and their sensing properties to methane were investigated in detail. Gas sensors based on these two samples demonstrate the highest CH₄ sensing response at an operating temperature of 300°C. Compared with traditional SnO₂ nanospheres, the nanofiber sensor shows obviously enhanced gas response, higher saturated detection concentration, and quicker response-recovery time to methane. Moreover, good stability, prominent reproducibility, and excellent selectivity are also observed based on the nanofibers. These results demonstrate the potential application of Co-doped SnO₂ nanofibers for fabricating high performance methane sensors.

1. Introduction

As an interesting chemically and thermally stable n-type semiconductor with wide band gap energy and large exciton binding energy, tin oxide (SnO₂) has attracted increasing attention and been extensively studied for catalysis [1], solar cells [2], optoelectronics [3], lithium-ion batteries [4], chemical sensors [5, 6], and so on [7–9]. Moreover, it has been proved to be a highly sensitive material for the detection of both reducing and oxidizing gases [10, 11]. Since the gas sensing properties of SnO₂-based sensors are closely related to the reactions between gas molecules and SnO₂ surfaces, interest in tailoring the microstructure and morphology of SnO₂ nanostructures has been greatly stimulated [12–14]. Over the past years, many scientific and technological efforts have been made to improve the sensitivity, response-recovery characteristic, selectivity, and stability of SnO₂-based sensors [15–17].

Recently, one-dimensional (1D) [18, 19] and quasi-one-dimensional [20] SnO₂ nanostructures with different morphologies including nanorods [21], nanotubes [22], nanowires [23], nanobelts [24], nanosheets [25], and nanofibers [26, 27] have been successfully fabricated and reported. Taking advantage of the small grain size, large surface-to-volume ratio, high density of surface sites, special hole, and pore structure, these novel low-dimensional SnO₂ nanostructures demonstrate excellent gas sensing performances than those of traditional SnO₂ nanoparticles or thin films. Currently, electrospinning [10, 11, 28, 29], sol-gel method [5], thermal evaporation technology [30], hydrothermal method [31], and chemical vapor deposition [32] are the main methods used to synthesize low-dimensional oxide nanostructures. Among all the fabrication techniques, electrospinning [17, 28] has been demonstrated as a relatively facile and versatile method for the large-scale synthesis of 1D

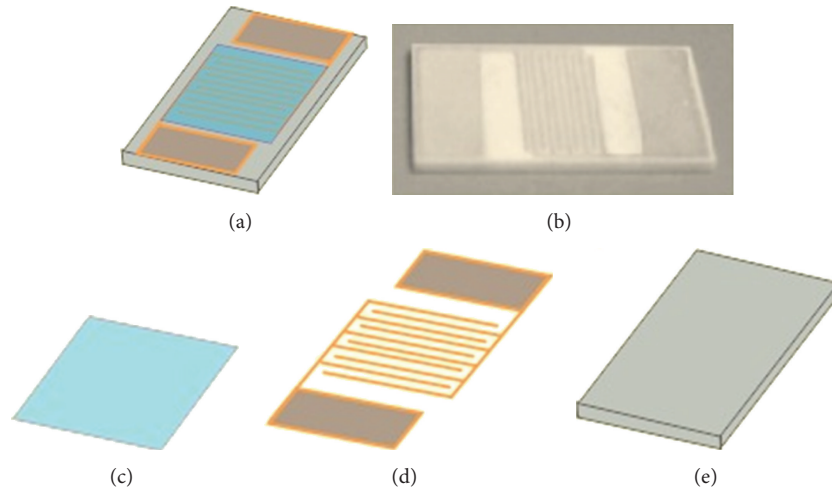


FIGURE 1: Structure chart of the planar sensor. (a) A top view of the substrate, (b) fabricated gas sensor, (c) sensing materials, (d) Ag-Pd interdigital electrodes, and (e) ceramic substrate.

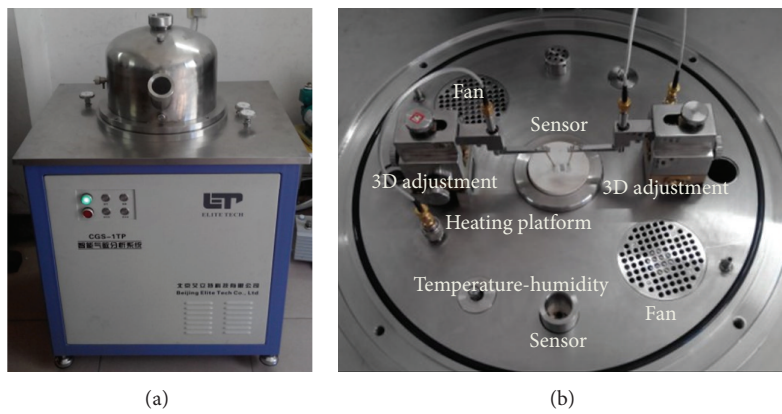


FIGURE 2: (a) The CGS-1TP gas sensing analysis system and (b) a photograph of the operating platform.

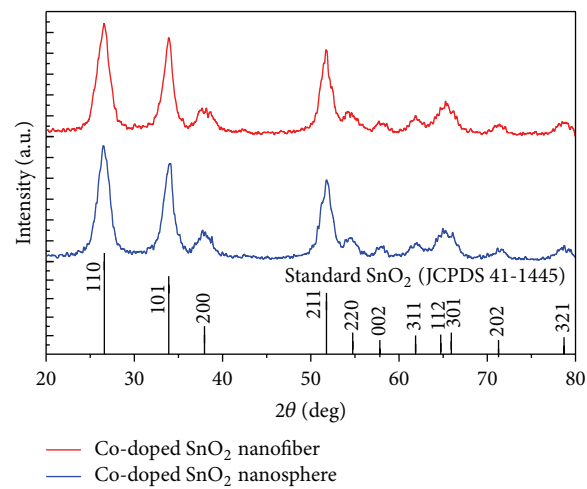


FIGURE 3: XRD diffraction patterns of the prepared ZnO nanostructures.

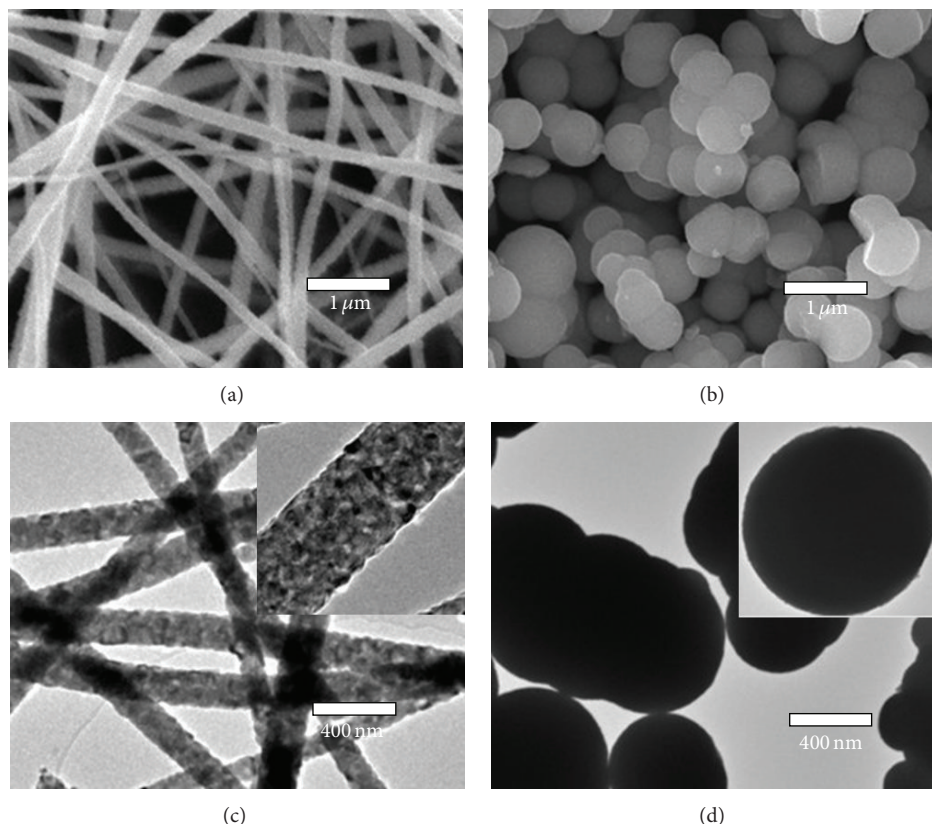


FIGURE 4: SEM images of (a) nanofibers, (b) nanospheres and TEM images of (c) nanofibers, (d) nanospheres. The inserts show the TEM images of individual fiber and sphere.

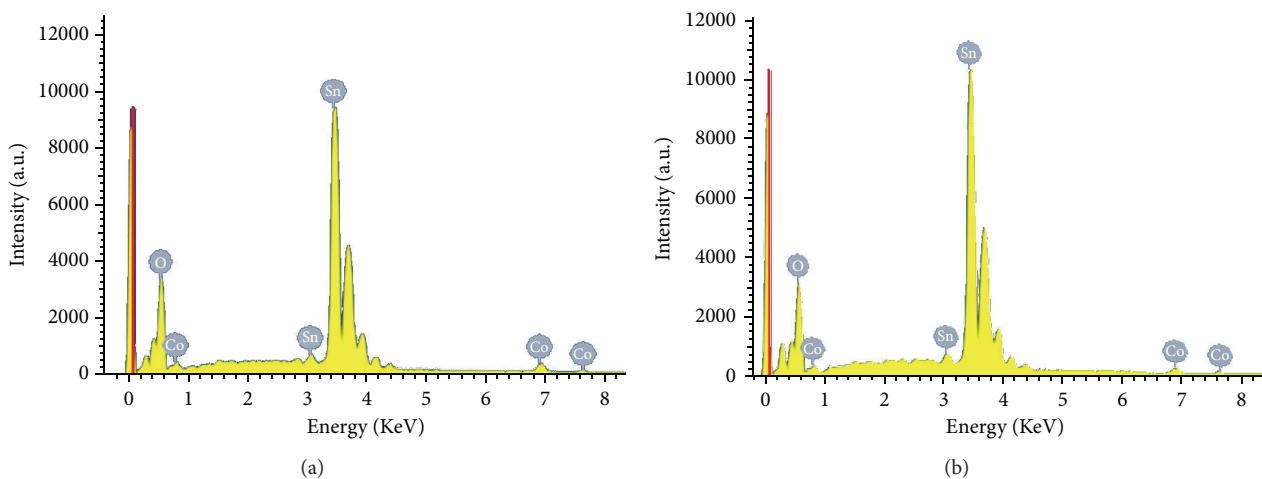


FIGURE 5: EDS spectra of 3 at% Co-doped SnO_2 (a) nanofibers and (b) nanospheres.

nanostructures that are exceptionally long in length, uniform in diameter, and large in surface area.

On the other hand, doping oxide sensors with various elements, for example, noble metals [33], rare-earth metals [34, 35], transition metals [36–38], and metal oxides [39–41], has been proved to be another effective method to improve sensing properties. Transition metal Co is a widely used dopant which acts as an activating catalyst to accelerate the

chemical reaction process and consequently improve the performances [42–44]. Up to now, there are many reports on synthesis of 1D SnO_2 nanofibers and their gas sensing properties. However, most of these gas sensors focus on HCHO [45], $\text{C}_2\text{H}_5\text{OH}$ [46, 47], $\text{C}_6\text{H}_5\text{OH}$ [13], CO [48], NO [49], H_2 [44], H_2S [50], and NH_3 [11], and rare studies concern CH_4 , a very important fault characteristic gas for transformer fault diagnosis and condition assessment. Meanwhile, a systematic

comparison of gas sensing performances between 1D SnO₂ nanofibers and traditional nanospheres may be one missing possibility along this direction.

In this paper, we reported a simple and facile approach to fabricate high-quality Co-doped SnO₂ nanofibers by electrospinning. Gas sensors were fabricated with the synthesized SnO₂ nanostructures and their sensing properties toward CH₄ are systematically investigated. The as-prepared Co-doped SnO₂ nanofibers exhibit excellent sensing characteristics, such as high sensitivity, rapid response-recovery time, and good stability than that of traditional nanospheres.

2. Experimental

Ethanol (>95%), N, N-dimethyl formamide (>95%, DMF), CoCl₂·2H₂O, and SnCl₂·2H₂O were used and purchased from Chongqing Chuandong Chemical Reagent Co., Ltd (China). Poly(vinyl pyrrolidone) (PVP, Mw = 1,300,000) was obtained from Aldrich. All chemicals were analytical grade and used as received without any further purification.

In a typical procedure of Co-doped SnO₂ nanofibers [11, 13, 15, 26, 29], 0.4 g of SnCl₂·2H₂O was dissolved in 4.42 g of DMF and 4.42 g of ethanol under vigorous stirring at 90°C for 30 min. Subsequently, 1.0 g PVP and appropriate quantity of CoCl₂·2H₂O (3 at%) were added into the above solution under vigorous stirring for 2 h until the salt was completely dissolved. Then the well-mixed precursor solution was loaded into a glass syringe with a needle of 1 mm in diameter at the tip and connected to a high-voltage DC power supply (ES 30-0.1P, Gamma High Voltage Research Inc.), which was capable of generating DC voltages of up to 30 kV. In our experiment, an optimal voltage of 10 kV was provided between the tip of the spinning nozzle and the collector at a distance of 20 cm. Finally, the fibers were peeled off from the collector with tweezers and placed in a crucible. The conversion of tin dichloride to SnO₂ and the removal of organic constituents PVP in the as-spun nanofibers were achieved by calcining at 600°C for 5 h in air.

Traditional Co-doped SnO₂ nanospheres (3 at%) were synthesized via hydrothermal method and the synthesis process is similar to our previous works [6, 12, 40]. Typically, 20 mL of absolute ethanol and distilled water (V/V, 1/1), 3.0 mmol SnCl₂·2H₂O, 0.09 mmol CoCl₂·2H₂O, and 20 mmol ammonia hydroxide were mixed together in a 100 mL capacity beaker and magnetically stirred at room temperature for 60 min. Then the fully mixed precursor was transferred into a 50 mL Teflon-lined stainless steel autoclave, sealed, and heated at 180°C for 16 h in an electric furnace for hydrothermal reaction. Finally, the product was harvested by centrifugation, washed with distilled water and absolute ethanol several times, and dried at 100°C in air for 24 h.

The crystalline structures of the prepared SnO₂ nanofibers and nanospheres were investigated by X-ray powder diffraction (XRD, Rigaku D/Max-1200X) with Cu K α radiation (40 kV, 200 mA and $\lambda = 1.5418 \text{ \AA}$). The microstructures and morphologies were characterized by means of field emission scanning electron microscope (FESEM, Hillsboro equipped with energy dispersive X-ray

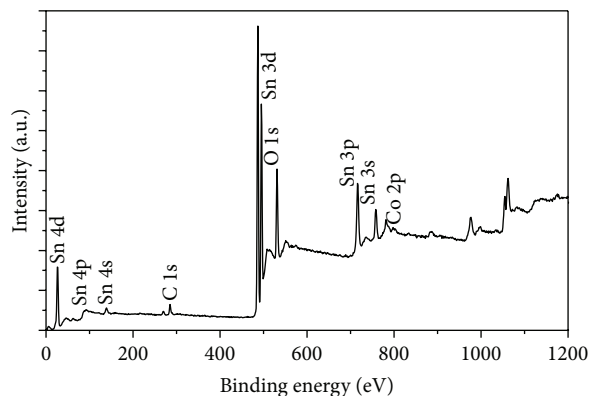


FIGURE 6: XPS survey spectra of 3 at% Co-doped SnO₂ nanofibers.

(EDS) spectroscopy) and transmission electron micrographs (TEM, Hitachi S-570). Analysis of the X-ray photoelectron spectra (XPS) was performed on an ESCLAB MKII using Al as the exciting source.

Gas sensors were fabricated by screen-printing technique with planar ceramic substrates, purchased from Beijing Elite Tech Co., Ltd, China. Figure 1 shows the schematic diagram of the planar sensor. It can be clearly seen in Figure 1 that the sensor consists of three kinds of significant components: ceramic substrate, Ag-Pd interdigital electrodes, and sensing materials. The length, width, and height of the planar ceramic substrate are suggested to be about 13.4, 7, and 1 mm, respectively. The as-prepared nanostructures were mixed with deionized water and absolute ethanol in a weight ratio of 100 : 20 : 10 to form a paste. Then the paste was subsequently screen-printed onto the planar ceramic substrate to form a sensing film with a thickness of about 50 μm . Finally, the fabricated sensor was dried in air at 80°C to volatilize the organic solvent and further aged in an aging test chamber for 36 h.

Gas sensing properties were investigated by a Chemical Gas Sensor-1 Temperature Pressure (CGS-1TP) intelligent gas sensing analysis system (Beijing Elite Tech Co., Ltd.) [41]. It could offer an external temperature control ranging from room temperature to 500°C with adjustment precision of 1°C. As seen in Figure 2(b) two adjustable probes were pressed on the sensor electrodes to collect electrical signals. When the sensor resistance was stable, certain amount of target gas was injected into the test chamber (18 L in volume) by a microinjector through a rubber plug. After its resistance value reached a new constant value, the test chamber was opened to recover. The sensor resistance and sensitivity were collected and analyzed by the system. And the environmental temperature, relative humidity, and working temperature were automatically recorded by the analysis system.

The sensitivity (S) was defined as $S = R_a/R_g$ [11, 13], where R_a was the sensor resistance in air and R_g in a mixture of target gas and air. The time taken by the sensor to achieve 90% of the total resistance change was designated as the response time in the case of gas adsorption or the recovery time in the case of gas desorption.

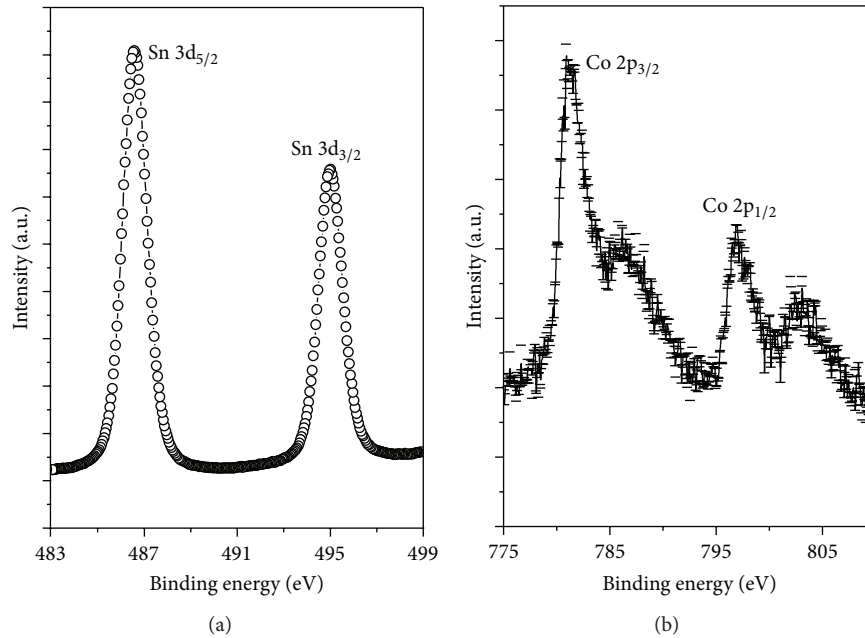


FIGURE 7: The Sn 3d (a) and Co 2p (b) binding energy spectra of 3 at% Co-doped SnO₂ nanofibers.

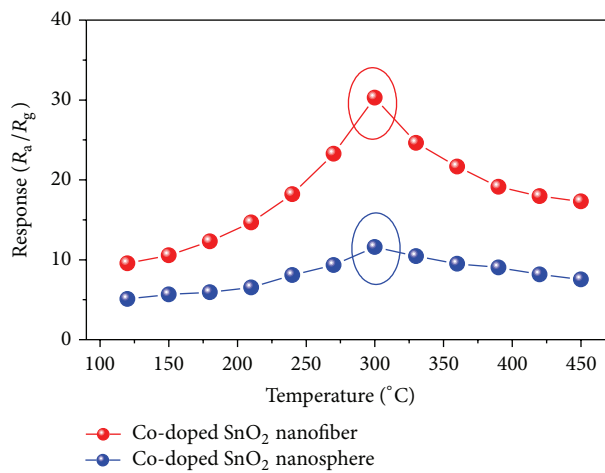


FIGURE 8: Responses of the SnO₂-based sensors to 50 ppm of CH₄ at different operating temperatures.

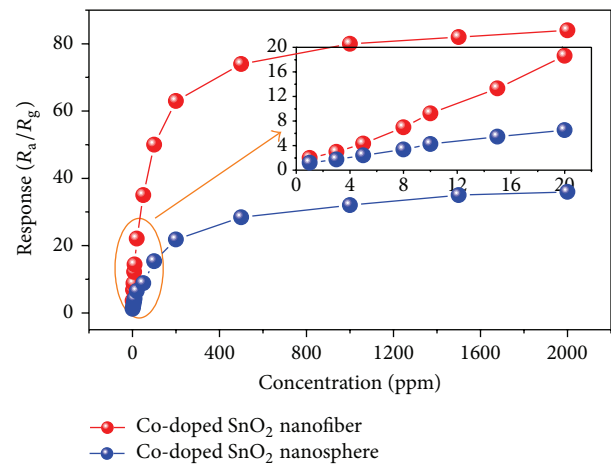


FIGURE 9: Responses of the SnO₂-based sensors to different concentrations of CH₄ at 300°C; the inserts show the relationship in the range of 1–20 ppm.

3. Results and Discussion

Figure 3 shows the XRD patterns of the as-prepared Co-doped SnO₂ nanofibers and nanospheres after calcinations. It can be clearly seen in Figure 3 that the synthesized samples are polycrystalline in nature. The prominent peaks of (110), (101), and (211) and other smaller peaks coincide with the corresponding peaks of rutile SnO₂ given in the standard data file (JCPDS File no. 41-1445). Due to the high dispersion and the low amount of Co ions (3 at%) doped in the synthesized samples, there is no indication of the presence of Co or other metal oxide diffraction peaks, implying a high purity of our products.

The overall surface morphologies of the products were performed firstly by SEM as shown in Figures 4(a) and 4(b). As shown in Figure 4(a) the disordered and bended nanofibers are randomly distributed to form a fibrous nonwoven. The average diameter of the as-spun nanofibers ranges from 200 to 120 nm, and the length of the fibers ranges from hundreds of nanometers to several ten micrometers. Figure 4(b) displays the typical SEM image of Co-doped SnO₂ nanospheres, where one can clearly note that the beautiful nanospheres are uniformly distributed across the whole sample and no other morphologies are detected. These nanospheres are rather dispersed and highly uniform in size and shape with an average diameter of 500 nm. Further

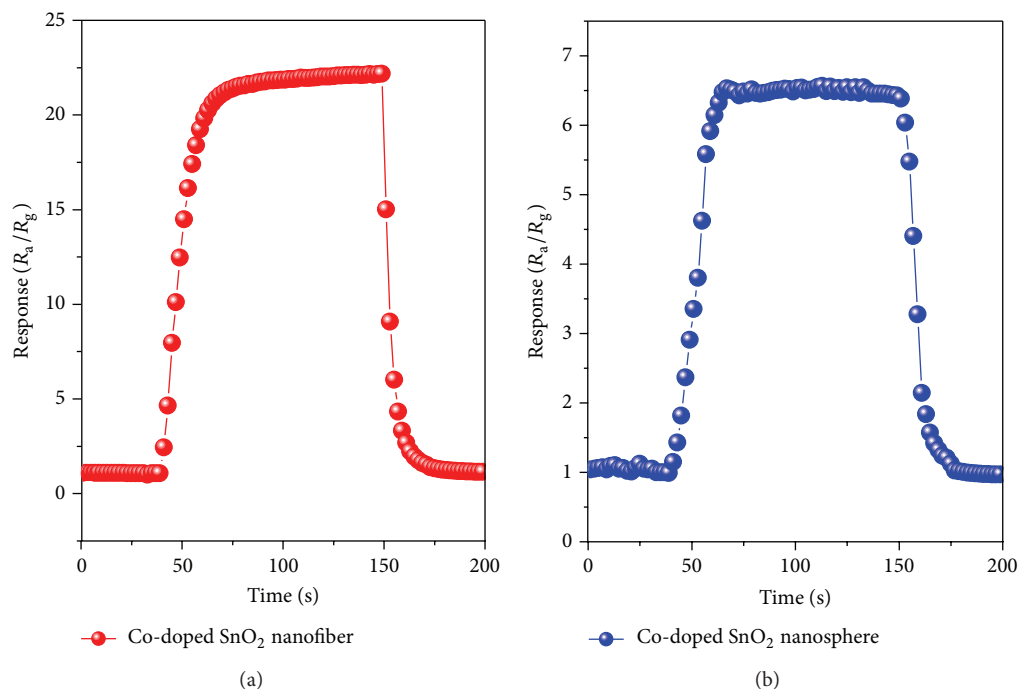


FIGURE 10: Response transients of Co-doped SnO₂ nanofibers (a) and nanospheres to 20 ppm of CH₄ at 300°C.

morphology characterization was examined by TEM and shown in Figures 4(c) and 4(d). The insets present the corresponding TEM images of individual fiber and sphere.

To check whether dopants have been successfully doped into the synthesized nanostructures, energy dispersive X-ray spectroscopy (EDS) measurement was conducted. Figures 5(a) and 5(b) show the EDS spectra of the as-prepared 3 at% Co-doped SnO₂ nanofibers and nanospheres, which confirm the availability of Co dopant on the SnO₂ matrix.

To further verify the existence of Co element and its valences in the synthesized samples, XPS data of the as-spun SnO₂ nanofibers is collected and presented in Figures 6 and 7. Figure 6 shows the wide spectrum, confirming the existence of Sn, O, and Co. The binding energies in Figure 7(a) at 486.5 and 493.8 eV correspond to Sn⁴⁺ of SnO₂. From the narrow spectrum of Co element as shown in Figure 7(b), the peak at 780.7 and 796.8 eV is identified as Co 2p_{3/2} and 2p_{1/2}, respectively, which possibly can be attributed to Co²⁺ ions [8]. Meanwhile the positions of the Co 2p_{3/2} and Co 2p_{1/2} peaks ruled out the presence of metallic Co and Co₂O₃ in the Co-doped SnO₂ nanofibers [9]. Moreover, the composition of the Co dopant in our products is calculated to be about 2.88 at%, which matches well its nominal concentration. Thus, based on the EDS and XPS results, the Co²⁺ ions are believed to be successfully incorporated into the SnO₂ nanocrystals.

The responses of the nanofiber and nanosphere sensors to 50 ppm of CH₄ gas as a function of operating temperature are measured and shown in Figure 8. For each sensor, the response is measured to increase rapidly with increasing operating temperature and arrive to the maximum and then decreases with a further rise of the operating temperature. The optimum operating temperatures of the nanofibers and

nanospheres are both suggested to be about 300°C with response values of 30.28 and 11.59, respectively.

The concentration dependence of Co-doped SnO₂ nanofibers and nanospheres was investigated in the range of 1–2000 ppm of CH₄ and the plots of the gas response against gas concentration are shown in Figure 9. As displayed in Figure 9, the gas response increases linearly with increasing the CH₄ concentration below 100 ppm but increases more slowly from 100 to 500 ppm, which indicates that the sensor becomes more or less saturated. Finally, the sensor reaches saturation after exposure to more than 2000 ppm. Although a similar trend was also observed for pure Co-doped SnO₂ nanospheres, the responses are much weaker. The inset in Figure 9 shows the response characteristics of the sensors to 1–20 ppm of CH₄, which indicates that the nanofibers sensor is much more favorable to detect CH₄ with a low concentration.

It is well known that response and recovery characteristics are important for evaluating the performances of semiconductor oxide sensors. Figure 10 shows the response transients of the two sensors exposed to 20 ppm of CH₄ gas at 300°C. According to the response-recovery time definition in Section 2, the response time and recovery time of nanofibers sensor were calculated to be 15 s and 12 s, and they were 22 s and 18 s for nanospheres.

To investigate the stability and repeatability of the Co-doped SnO₂ nanofibers sensor, it was sequentially exposed to different levels of CH₄ gas as shown in Figure 11 (3, 5, 8, 10, 20, and 50 ppm) and equal concentration as shown in Figure 12 (20, 20, 20, 20, and 20 ppm). As shown in Figures 11 and 12, the sensor response increases rapidly when exposed to certain concentration of CH₄ and decreases dramatically

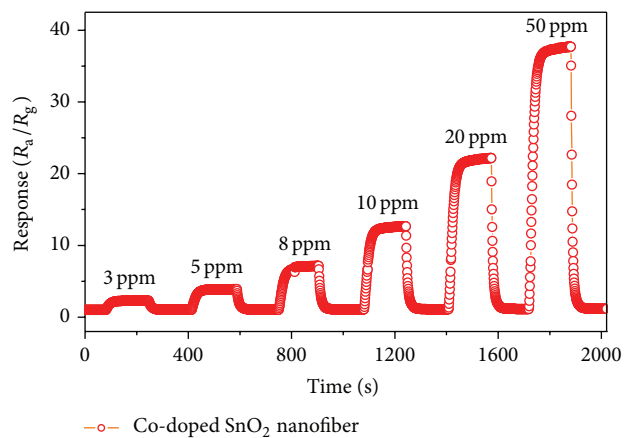


FIGURE 11: Dynamic CH_4 sensing transients of the Co-doped SnO_2 nanofiber sensor at 300°C .

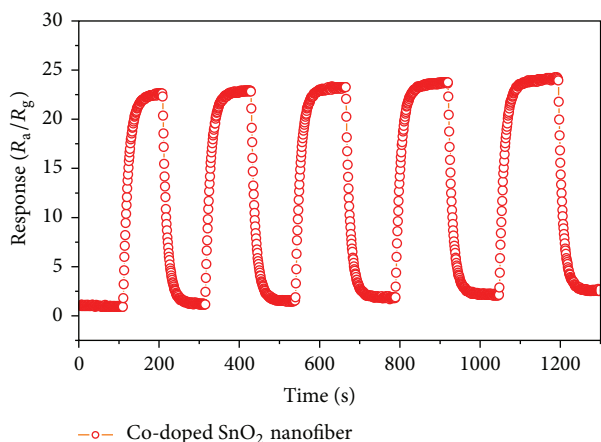


FIGURE 12: Reproducibility of the Co-doped SnO_2 nanofiber sensor on successive exposure (5 cycles) to 20 ppm of CH_4 at 300°C .

when exposed to air for recovering. Meanwhile, the gas response of the sensor always returns to its initial value during the continuous test period, implying a very satisfying reproducibility of the prepared sensor.

Figure 13 depicts the histogram of the gas response of the Co-doped SnO_2 nanofiber sensor to 50 ppm of various gases, including CH_4 , CH_3OH , $\text{C}_2\text{H}_5\text{OH}$, NH_3 , NO , and CO at 300°C . One can clearly see in Figure 13 that this sensor shows obvious CH_4 sensing response than other potential interface gases, which can be mainly attributed to the effect of sensor operating temperature on the activity of gas molecules.

A possible sensing mechanism is depicted as follows to understand the gas sensing reaction process of SnO_2 -based sensor against CH_4 gas and explain the enhanced CH_4 sensing properties of the as-spun nanofibers. It is well known to all that SnO_2 belongs to typical n-type semiconductor sensing materials and its sensing properties are dominantly controlled by the change of SnO_2 surface resistance, especially the adsorption and desorption of oxygen on the surface of sensing materials [5]. Owing to the nonstoichiometry of the as-synthesized SnO_2 nanostructures, many oxygen vacancies

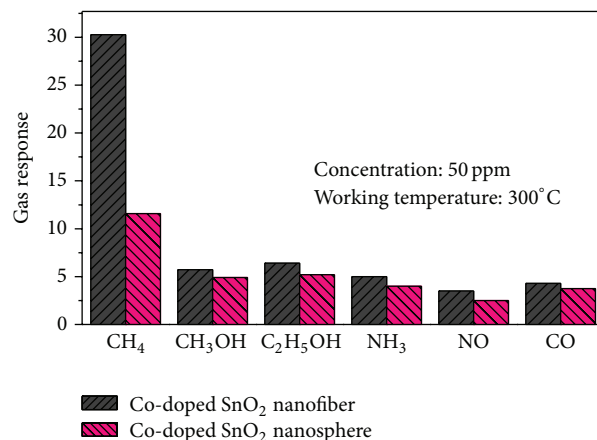


FIGURE 13: Selectivity of the Co-doped SnO_2 nanofiber sensor on successive exposure to 20 ppm of various gases at 300°C .

are formed in SnO_2 crystal [6]. When the sensor is aged in ambient air, free oxygen could be absorbed on its surface and act as a trap capturing electrons from the conduction band of SnO_2 to generate chemisorbed oxygen species, namely, O_2^- , O^{2-} , and O^- . These chemisorbed oxygen species would cause an energy band bending of SnO_2 and depletion layers are formed around the surface area, increasing the energy barrier of SnO_2 and decreasing its carrier concentration and electron mobility [11]. Thus, a less conductive SnO_2 -based sensor is measured. When the sensor is exposed to ambient CH_4 , chemical reactions take place between the CH_4 molecules and the chemisorbed O_2^- , O^{2-} , and O^- , which releases the trapped electrons back to the conduction band, increasing the carrier concentration and electron mobility; thus a decreased resistance is found in our measurements [12].

Many former papers have reported and demonstrated that Co is an effective dopant to improve the gas sensing properties of metal oxide semiconductor materials, which is mainly due to the excellent electronic and chemical sensitization [42–44]. The improved CH_4 sensing properties of Co-doped SnO_2 nanofibers measured above are mainly based on the unique fiber structure [13]. Compared with traditional nanospheres, the as-spun 1D SnO_2 nanofibers possess larger surface to volume ratio, providing much more reaction sites for the target gas adsorption. Moreover, there are many nanofiber-nanofiber junctions in the netlike SnO_2 nanofibers [43]. Such junctions could form a depleted layer around the intersection, which promotes the oxygen species adsorption onto the interfacial region significantly. Then electron capture and release could undergo in a relatively easier way, accelerating the electron flow; as a result, more efficient charge transfer takes place and enhanced CH_4 sensing properties are observed.

4. Conclusions

In that summary, 3 at% Co-doped SnO_2 nanofibers have been synthesized via a simple electrospinning method and characterized by XRD, SEM, TEM, EDS, and XPS. The as-spun 3 at% Co-doped SnO_2 nanofibers exhibit high sensitivity,

supersaturated detection concentration, and rapid response and recovery against CH₄ than that of 3 at% Co-doped SnO₂ nanospheres, prepared by traditional hydrothermal synthesis route. In addition, the nanofiber sensor demonstrates excellent selectivity, prominent stability, and good reproducibility to CH₄. All results suggest that the as-spun 3 at% Co-doped SnO₂ nanofibers sensors are potential candidates for CH₄ detection. Furthermore, this method may be extendable to develop high performance semiconductor sensors monitoring other fault characteristic gases dissolved in transformer oil.

Acknowledgments

This work has been supported in part by the National Natural Science Foundation of China (no. 51277185 and 51202302), National Special Fund for Major Research Instrumentation Development (no. 2012YQ16000705), and the Funds for Innovative Research Groups of China (no. 51021005).

References

- [1] J. Yu, D. Zhao, X. L. Xu, X. Wang, and N. Zhang, "Study on RuO₂/SnO₂: novel and active catalysts for CO and CH₄ oxidation," *ChemCatChem*, vol. 4, no. 8, pp. 1122–1132, 2012.
- [2] J. F. Qian, P. Liu, Y. Xiao et al., "TiO₂-coated multilayered SnO₂ hollow microspheres for dye-sensitized solar cells," *Advanced Materials*, vol. 21, no. 36, pp. 3663–3667, 2009.
- [3] L.-B. Luo, F.-X. Liang, and J.-S. Jie, "Sn-catalyzed synthesis of SnO₂ nanowires and their optoelectronic characteristics," *Nanotechnology*, vol. 22, no. 48, Article ID 485701, 2011.
- [4] J. S. Chen, L. A. Archer, and X. W. D. Lou, "SnO₂ hollow structures and TiO₂ nanosheets for lithium-ion batteries," *Journal of Materials Chemistry*, vol. 21, no. 27, pp. 9912–9924, 2011.
- [5] W. Zeng, T. M. Liu, D. J. Liu, and E. J. Han, "Hydrogen sensing and mechanism of M-doped SnO₂ (M=Cr³⁺, Cu²⁺ and Pd²⁺) nanocomposite," *Sensors and Actuators B*, vol. 160, no. 1, pp. 455–462, 2011.
- [6] W. G. Chen, Q. Zhou, T. Y. Gao, X. P. Su, and F. Wan, "Pd-doped SnO₂-based sensor detecting characteristic fault hydrocarbon gases in transformer oil," *Journal of Nanomaterials*, vol. 2013, Article ID 127345, 9 pages, 2013.
- [7] H. Huang, C. K. Lim, M. S. Tse, J. Guo, and O. K. Tan, "SnO₂ nanorod arrays: low temperature growth, surface modification and field emission properties," *Nanoscale*, vol. 4, no. 5, pp. 1491–1496, 2012.
- [8] K. Srinivas, M. Vithal, B. Sreedhar, M. M. Raja, and P. V. Reddy, "Structural, optical, and magnetic properties of nanocrystalline Co doped SnO₂ based diluted magnetic semiconductors," *The Journal of Physical Chemistry C*, vol. 113, no. 9, pp. 3543–3552, 2009.
- [9] X. F. Liu, J. Iqbal, S. L. Yang, B. He, and R. H. Yu, "Nitrogen doping-mediated room-temperature ferromagnetism in insulating Co-doped SnO₂ films," *Applied Surface Science*, vol. 256, no. 14, pp. 4488–4492, 2010.
- [10] W. G. Chen, Q. Zhou, F. Wan, and T. Y. Gao, "Gas sensing properties and mechanism of nano-SnO₂-based sensor for hydrogen and carbon monoxide," *Journal of Nanomaterials*, vol. 2012, Article ID 612420, 9 pages, 2012.
- [11] H. G. Zhang, Z. Y. Li, L. Liu et al., "Enhancement of hydrogen monitoring properties based on Pd-SnO₂ composite nanofibers," *Sensors and Actuators B*, vol. 147, no. 1, pp. 111–115, 2010.
- [12] Q. Qi, T. Zhang, L. Liu, X. J. Zheng, and G. Y. Lu, "Improved NH₃, C₂H₅OH, and CH₃COCH₃ sensing properties of SnO₂ nanofibers by adding block copolymer P123," *Sensors and Actuators B*, vol. 141, no. 1, pp. 174–178, 2009.
- [13] K. J. Choi and H. W. Jang, "One-dimensional oxide nanostructures as gas-sensing materials: review and issues," *Sensors*, vol. 10, no. 4, pp. 4083–4099, 2010.
- [14] Q. Qi, T. Zhang, L. Liu, and X. J. Zheng, "Synthesis and toluene sensing properties of SnO₂ nanofibers," *Sensors and Actuators B*, vol. 137, no. 2, pp. 471–475, 2009.
- [15] W. G. Chen, Q. Zhou, and S. D. Peng, "Hydrothermal synthesis of Pt-, Fe-, and Zn-doped SnO₂ nanospheres and carbon monoxide sensing properties," *Advances in Materials Science and Engineering*, vol. 2013, Article ID 578460, 8 pages, 2013.
- [16] Z. J. Wang, Z. Y. Li, T. T. Jiang, X. R. Xu, and W. Wang, "Ultrasensitive hydrogen sensor based on Pd⁰-loaded SnO₂ electrospun nanofibers at room temperature," *ACS Applied Materials & Interfaces*, vol. 5, no. 6, pp. 2013–2021, 2013.
- [17] L. L. Wang, H. M. Dou, Z. Lou, and T. Zhang, "Encapsulated nanoreactors (Au@ SnO₂): a new sensing material for chemical sensors," *Nanoscale*, vol. 5, no. 7, pp. 2686–2691, 2011.
- [18] J. Fang, H. T. Niu, T. Lin, and X. G. Wang, "Applications of electrospun nanofibers," *Chinese Science Bulletin*, vol. 53, no. 15, pp. 2265–2286, 2008.
- [19] S. Barth, F. Hernandez-Ramirez, J. D. Holmes, and A. Romano-Rodriguez, "Synthesis and applications of one-dimensional semiconductors," *Progress in Materials Science*, vol. 55, no. 6, pp. 563–627, 2010.
- [20] Y. N. Xia, P. D. Yang, Y. G. Sun et al., "One-dimensional nanostructures: synthesis, characterization, and applications," *Advanced Materials*, vol. 15, no. 5, pp. 353–389, 2003.
- [21] J. G. Lu, P. C. Chang, and Z. Y. Fan, "Quasi-one-dimensional metal oxide materials-synthesis, properties and applications," *Materials Science and Engineering R*, vol. 52, no. 1–3, pp. 49–91, 2006.
- [22] Y. J. Chen, X. Y. Xue, Y. G. Wang, and T. H. Wang, "Synthesis and ethanol sensing characteristics of single crystalline SnO₂ nanorods," *Applied Physics Letters*, vol. 87, no. 23, Article ID 233503, pp. 1–3, 2005.
- [23] Z. W. Pan, Z. R. Dai, and Z. L. Wang, "Nanobelts of semiconducting oxides," *Science*, vol. 291, no. 5510, pp. 1947–1949, 2001.
- [24] B. Wang, L. F. Zhu, Y. H. Yang, N. S. Xu, and G. W. Yang, "Fabrication of a SnO₂ nanowire gas sensor and sensor performance for hydrogen," *The Journal of Physical Chemistry C*, vol. 112, no. 17, pp. 6643–6647, 2008.
- [25] Y. B. Shen, T. Yamazaki, Z. F. Liu et al., "Microstructure and H₂ gas sensing properties of undoped and Pd-doped SnO₂ nanowires," *Sensors and Actuators B*, vol. 135, no. 2, pp. 524–529, 2009.
- [26] C. Wang, Y. Zhou, M. Y. Ge, X. B. Xu, Z. Zhang, and J. Z. Jiang, "Large-scale synthesis of SnO₂ nanosheets with high lithium storage capacity," *Journal of the American Chemical Society*, vol. 132, no. 1, pp. 46–47, 2010.
- [27] Y. Zhang, X. He, J. Li, Z. Miao, and F. Huang, "Fabrication and ethanol-sensing properties of micro gas sensor based on electrospun SnO₂ nanofibers," *Sensors and Actuators B*, vol. 132, no. 1, pp. 67–73, 2008.

- [28] X. Song, Z. Wang, Y. Liu, C. Wang, and L. Li, "A highly sensitive ethanol sensor based on mesoporous ZnO-SnO₂ nanofibers," *Nanotechnology*, vol. 20, no. 7, Article ID 075501, 2009.
- [29] T. Lin, D. Lukas, and G. S. Bhat, "Nanofiber manufacture, properties, and applications," *Journal of Nanomaterials*, vol. 2013, 1 page, Article ID 368191, 2013.
- [30] J. Doshi and D. H. Reneker, "Electrospinning process and applications of electrospun fibers," *Journal of Electrostatics*, vol. 35, no. 2-3, pp. 151-160, 1995.
- [31] Z. R. Dai, Z. W. Pan, and Z. L. Wang, "Novel nanostructures of functional oxides synthesized by thermal evaporation," *Advanced Functional Materials*, vol. 13, no. 1, pp. 9-24, 2003.
- [32] L. Tan, L. Wang, and Y. Wang, "Hydrothermal synthesis of SnO₂ nanostructures with different morphologies and their optical properties," *Journal of Nanomaterials*, vol. 2011, Article ID 529874, 10 pages, 2011.
- [33] Y. Liu, E. Koep, and M. Liu, "A highly sensitive and fast-responding SnO₂ sensor fabricated by combustion chemical vapor deposition," *Chemistry of Materials*, vol. 17, no. 15, pp. 3997-4000, 2005.
- [34] L. L. Wang, Z. Lou, R. Wang, T. Fei, and T. Zhang, "Ring-like PdO-NiO with lamellar structure for gas sensor application," *Journal of Materials Chemistry*, vol. 22, no. 25, pp. 12453-12456, 2012.
- [35] H. Bastami, E. Taheri-Nassaj, P. F. Smet, K. Korthout, and D. Poelman, "(Co, Nb, Sm)-doped tin dioxide varistor ceramics sintered using nanopowders prepared by coprecipitation method," *Journal of the American Ceramic Society*, vol. 94, no. 10, pp. 3249-3255, 2011.
- [36] Q. Qi, T. Zhang, X. Zheng et al., "Electrical response of Sm₂O₃-doped SnO₂ to C₂H₂ and effect of humidity interference," *Sensors and Actuators B*, vol. 134, no. 1, pp. 36-42, 2008.
- [37] W. Zeng, T. Liu, Z. Wang, S. Tsukimoto, M. Saito, and Y. Ikuhara, "Selective detection of formaldehyde gas using a Cd-doped TiO₂-SnO₂ sensor," *Sensors*, vol. 9, no. 11, pp. 9029-9038, 2009.
- [38] X. Liu, J. Zhang, X. Guo, S. Wu, and S. Wang, "Enhanced sensor response of Ni-doped SnO₂ hollow spheres," *Sensors and Actuators B*, vol. 152, no. 2, pp. 162-167, 2011.
- [39] K. M. Kim, H. M. Jeong, H. R. Kim, K. Choi, H. J. Kim, and J. H. Lee, "Selective detection of NO₂ using Cr-doped CuO nanorods," *Sensors*, vol. 12, no. 6, pp. 8013-8025, 2012.
- [40] Z. Lou, J. N. Deng, L. L. Wang, R. Wang, T. Fei, and T. Zhang, "A class of hierarchical nanostructures: ZnO surface-functionalized TiO₂ with enhanced sensing properties," *RSC Advances*, vol. 3, no. 9, pp. 3131-3136, 2013.
- [41] W. Zeng, T. Liu, and Z. Wang, "Enhanced gas sensing properties by SnO₂ nanosphere functionalized TiO₂ nanobelts," *Journal of Materials Chemistry*, vol. 22, no. 8, pp. 3544-3548, 2012.
- [42] X.-J. Zhang and G.-J. Qiao, "High performance ethanol sensing films fabricated from ZnO and In₂O₃ nanofibers with a double-layer structure," *Applied Surface Science*, vol. 258, no. 17, pp. 6643-6647, 2012.
- [43] Z. Li and Y. Dzenis, "Highly efficient rapid ethanol sensing based on Co-doped In₂O₃ nanowires," *Talanta*, vol. 85, no. 1, pp. 82-85, 2011.
- [44] L. Liu, S. Li, J. Zhuang et al., "Improved selective acetone sensing properties of Co-doped ZnO nanofibers by electrospinning," *Sensors and Actuators B*, vol. 155, no. 2, pp. 782-788, 2011.
- [45] L. Liu, C. Guo, S. Li, L. Wang, Q. Dong, and W. Li, "Improved H₂ sensing properties of Co-doped SnO₂ nanofibers," *Sensors and Actuators B*, vol. 150, no. 2, pp. 806-810, 2010.
- [46] H. Du, J. Wang, M. Su, P. Yao, Y. Zheng, and N. Yu, "Formaldehyde gas sensor based on SnO₂/In₂O₃ hetero-nanofibers by a modified double jets electrospinning process," *Sensors and Actuators B*, vol. 166, no. 2, pp. 746-752, 2012.
- [47] L. Liu, S. C. Li, L. Y. Wang, C. C. Guo, and Q. Y. Dong, "Enhancement ethanol sensing properties of NiO-SnO₂ nanofibers," *Journal of the American Ceramic Society*, vol. 94, no. 3, pp. 771-775.
- [48] X. Song and L. Liu, "Characterization of electrospun ZnO-SnO₂ nanofibers for ethanol sensor," *Sensors and Actuators A*, vol. 154, no. 1, pp. 175-179, 2009.
- [49] X. J. Yue, T. S. Hong, W. Xiang, K. Cai, and X. Xu, "High performance micro CO sensors based on ZnO-SnO₂ composite nanofibers with anti-humidity characteristics," *Chinese Physics Letters*, vol. 29, no. 12, Article ID 120702, pp. 1-4, 2012.
- [50] J.-A. Park, J. Moon, S.-J. Lee, S. H. Kim, H. Y. Chu, and T. Zyung, "SnO₂-ZnO hybrid nanofibers-based highly sensitive nitrogen dioxides sensor," *Sensors and Actuators B*, vol. 145, no. 1, pp. 592-595, 2010.

Research Article

Synthesis and Characterization of Drug-Loaded Poly(ϵ -caprolactone)/Silica Hybrid Nanofibrous Scaffolds

Kwan-Ha Shin,¹ Young-Hag Koh,^{1,2} and Hyoun-Ee Kim³

¹ Department of Dental Laboratory Science and Engineering, Korea University, Seoul 136-703, Republic of Korea

² Department of Orthopaedics, Korea University Medical Center, Guro Hospital, Seoul 152-703, Republic of Korea

³ Department of Materials Science and Engineering, Seoul National University, Seoul 151-742, Republic of Korea

Correspondence should be addressed to Young-Hag Koh; kohyh@korea.ac.kr

Received 19 July 2013; Revised 27 September 2013; Accepted 27 September 2013

Academic Editor: Raghavendra Hegde

Copyright © 2013 Kwan-Ha Shin et al. This is an open access article distributed under the Creative Commons Attribution License, which permits unrestricted use, distribution, and reproduction in any medium, provided the original work is properly cited.

We produced drug-loaded poly(ϵ -caprolactone) (PCL)/silica hybrid nanofibrous scaffolds with various silica sol contents (0 vol%, 10 vol%, 15 vol%, and 20 vol%) using electrospinning and examined their physicochemical properties, mechanical properties, drug release behavior, and *in vitro* biocompatibility to evaluate their potential application for guided bone regeneration (GBR). The loading efficiency of tetracycline hydrochloride (TCH) drug was remarkably enhanced by hybridizing the PCL solution with the silica sol. All produced hybrid scaffolds had a highly nanofibrous structure, in which the silica phase was homogeneously hybridized with the PCL polymer, while preserving their intrinsic characteristics. This led to considerable increases in hydrophilicity and mechanical properties (e.g., ultimate tensile strength and elastic modulus). In addition, the release rate and cumulative maximum amounts of the TCH from the hybrid scaffolds significantly increased with increasing the silica content, while all produced hybrid nanofibrous scaffolds showed good biocompatibility assessed by *in vitro* cell tests.

1. Introduction

Fundamentally, extracellular matrix (ECM) plays a crucial regulatory role in guiding cells attachment, growth, migration and differentiation as well as formation of new tissues [1, 2]. This encouraged materials scientists and engineers to design and create new biomaterials that can mimic the micro-/nanostructure and chemical composition of the native ECM [3]. One of the most promising approaches for this goal is to use electrospinning (ES), which can create a nanofibrous structure with high porosity and surface-to-volume ratio. This biomimetic nanofibrous structure with biocompatible surfaces can provide a favorable environment for guided bone regeneration (GBR) [4–8]. In addition, nanofibrous scaffolds can deliver drugs in a controlled manner [9–14], which is expected to prevent damages caused by infection, thereby accelerating bone healing process when used as a bone scaffold [15, 16].

As a scaffolding material, poly(ϵ -caprolactone) (PCL), one of the most widely used biodegradable polymers, has

been extensively examined owing to its proper strength and flexibility [17–20]. However, PCL polymer has low stiffness, hydrophobic nature, and limited cell affinity [8]. Thus, considerable effort has been made to incorporate bioactive inorganic particles into PCL nanofibers for improving the biocompatibility *in vitro* and *in vivo* [21–23]. More recently, sol-gel derived silica has gained increasing interest as an alternative inorganic phase, since it can be homogeneously hybridized with biodegradable polymers at the molecular level [24–29]. These organic/inorganic hybrids can more closely mimic the chemical composition and nanostructure of the native bone ECM, leading to significantly enhanced mechanical properties and biocompatibility [30].

In this study, we produced drug-loaded PCL/silica hybrid nanofibrous scaffolds using ES and examined their physicochemical properties, mechanical properties, drug release behavior, and *in vitro* biocompatibility to evaluate their potential application for GBR. For this goal, PCL solutions were directly hybridized with various amounts of the silica sol (0 vol%, 10 vol%, 15 vol%, and 20 vol% in relation to PCL)

containing tetracycline hydrochloride (TCH) used as a drug. The nanofibrous structure, chemical composition, and chemical structure were characterized by a range of analysis tools, including field emission scanning electron microscope (FE-SEM), energy dispersive spectroscopy (EDS), and attenuated total reflection Fourier transform infrared spectroscopy (ATR-FTIR). The mechanical properties were examined by tensile strength tests. The release behavior of the TCH from the PCL/silica hybrid nanofibrous scaffolds was examined. The *in vitro* biocompatibility was evaluated in terms of proliferation of preosteoblast cells.

2. Materials and Methods

2.1. Starting Materials. Unless specified otherwise, all reagents were purchased from Sigma-Aldrich (Sigma Aldrich, St. Louis, MO, USA).

2.2. PCL/Silica Hybrid Mixture Preparation. A PCL solution was prepared by dissolving 12 g PCL ($M_n = 80,000$ g/mol) in 100 mL of tetrahydrofuran (THF) at 40°C using a magnetic stirrer. Separately, a silica sol was synthesized through sol-gel process at room temperature by mixing tetraethyl orthosilicate ($\text{Si}(\text{OC}_2\text{H}_5)_4$; TEOS), distilled water, and ethanol at a molar ratio of 1:4:1 with the assistance of 1N HCl as a catalyst using a magnetic stirrer for 2 h. Subsequently, predetermined amounts of the silica sol (0 vol%, 10 vol%, 15 vol%, and 20 vol% in relation to PCL) were added to the PCL solutions and vigorously mixed by magnetic stirring for 30 min, after which, tetracycline hydrochloride (TCH) used as a drug with a concentration of 20 mg/mL was added to the PCL/silica hybrid mixtures, followed by magnetic stirring for 2 h at room temperature. The viscosity of the PCL/silica hybrid mixtures was measured using a viscometer (Brookfield Dial Reading Viscometer, Hwashin Instrument Co. Ltd., Republic of Korea).

2.3. Electrospinning Process. The prepared PCL/silica hybrid mixtures containing TCH were loaded into 10 mL syringes. Electrospinning was conducted at a flow rate of 2 mL/h and a tip-target distance of 10 cm, while a range of applied voltages (7–17 kV) were applied to achieve a uniform nanofibrous structure depending on the silica sol content (0 vol%, 10 vol%, 15 vol%, and 20 vol%). PCL/silica hybrid nanofibrous scaffolds produced were removed carefully from the mandrel and kept at room temperature in ambient condition more than 3 days to completely remove the solvents. For comparison purposes, dense PCL/silica hybrid films were also prepared by spin coating technique.

2.4. Nanofibrous Structure Evaluation. The morphology of the TCH-loaded PCL/silica hybrid nanofibrous scaffolds with various silica sol contents (0 vol%, 10 vol%, 15 vol%, and 20 vol%) was examined by field emission scanning electron microscopy (FE-SEM; JSM-6330F, JEOL, Japan). The diameters of the hybrid nanofibers were roughly measured from the SEM images. The chemical composition and structure of the hybrid nanofibrous scaffolds were characterized

by energy dispersive spectroscopy (EDS) attached to the FE-SEM and attenuated total reflection Fourier transform infrared spectroscopy (ATR-FTIR, Nicolet 6700, Thermo Scientific, USA), respectively. The nanostructure of the hybrid nanofibers was observed more closely using transmission electron microscopy (TEM) (JEM-2000EXII, JEOL, Japan) after the PCL/silica hybrid mixtures were directly electrospun onto a copper grid coated with an amorphous carbon film. Energy dispersive X-ray spectroscopy (EDS) analysis was carried out during the TEM observations to confirm the existence of silica in the hybrid nanofibers.

The final content of the silica phase in the hybrid nanofibrous scaffolds with various silica sol contents (0 vol%, 10 vol%, 15 vol%, and 20 vol%) was determined by thermogravimetric analysis (TGA; TA Instruments, New Castle, DE, USA). The hybrid nanofibrous scaffolds were heated up to 700°C at a heating rate of 10°C/min in a flowing nitrogen atmosphere. The weight losses of the specimens during the tests were monitored and used to calculate the final silica contents.

2.5. Hydrophilicity Measurement. The hydrophilicity of the TCH-loaded PCL/silica hybrid nanofibrous scaffolds with various silica sol contents (0 vol%, 10 vol%, 15 vol%, and 20 vol%) was evaluated using water contact angle measurements using an OCA15 contact angle analyzer (Dataphysics Co, Germany). A distilled water droplet size of $\sim 2 \mu\text{L}$ from a syringe was placed carefully onto the surface of the hybrid nanofibrous scaffolds at room temperature. After a period of 20 seconds, the contact angle was recorded. The mean value and standard deviation (SD) were calculated through testing at five different positions on the same sample.

2.6. Mechanical Properties Test. The mechanical properties of the TCH-loaded PCL/silica hybrid nanofibrous scaffolds were evaluated using tensile strength tests. The specimens with dimensions of 7.5 mm \times 10 mm \times 0.02 mm were tested at a crosshead speed of 1 mm/min using a screw-driven load frame (Oriental Testing Machine Co, Republic of Korea) at a temperature of $\sim 37^\circ\text{C}$ [31]. The stress versus strain responses of the specimens during the tensile strength tests were recorded. The tensile strength and strain at failure were obtained from stress versus strain curves. The elastic modulus was determined from the slope of the initial linear portion of the curves. Six specimens were tested to obtain the mean and standard deviation for each hybrid nanofibrous scaffold.

2.7. Drug Release Test. The drug release behavior of the TCH-loaded PCL/silica hybrid nanofibrous scaffolds with various silica sol contents (0 vol%, 10 vol%, 15 vol%, and 20 vol%) was examined. The specimens were immersed in 6 mL of phosphate buffered saline (PBS) solution (pH 7.4) and then placed in a water bath at 37°C for up to 48 h. At selected intervals, 3 mL aliquots were withdrawn and analyzed using an ultraviolet (UV) spectrophotometer (V-630; JASCO, Japan) at an optimal wavelength of 355 nm. An equal volume of fresh medium was added to the incubation solution. The release amount of the TCH was calculated

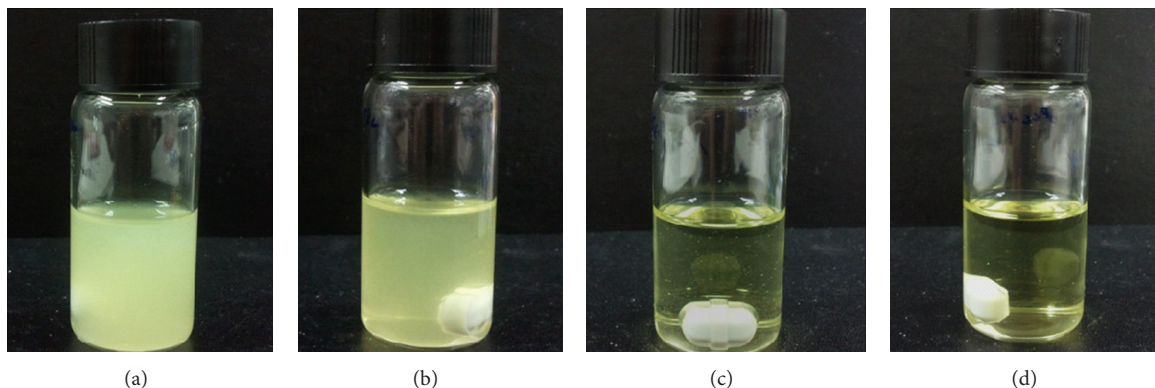


FIGURE 1: Typical optical image of the TCH-loaded PCL/silica hybrid mixtures with various silica sol contents (0 vol%, 10 vol%, 15 vol%, and 20 vol%).

from an absorbance-concentration calibration curve, which was constructed over the concentration range from 1 to 100 $\mu\text{g}/\text{mL}$, and the cumulative TCH release was represented after being normalized to its initial amount in the scaffolds, obtained by multiplying the weight of the preobtained nanofibrous scaffold by the theoretical weight percentage of TCH. The drug-release test was performed in triplicate, and data were reported as mean \pm standard deviation (SD).

2.8. In Vitro Biocompatibility Evaluation. The *in vitro* biocompatibility of the TCH-loaded PCL/silica hybrid nanofibrous scaffolds with various silica sol contents (0 vol%, 10 vol%, 15 vol%, and 20 vol%) was evaluated using a pre-osteoblast cell line (MC3T3-E1; ATCC, CRL-2593, Rockville, MD, USA). The MC3T3-E1 cells were cultured in Duebecco's modified eagle medium (DMEM; Welgene Co., Ltd., Seoul, Republic of Korea) supplemented with 5% fetal bovine serum (FBS) in a humidified incubator in an atmosphere containing 5% CO_2 at 37°C. Prior to the cell seeding, the specimens with dimensions of 1 mm \times 1 mm were sterilized under ultraviolet (UV) irradiation for 30 min and soaked in 70% ethanol for 4 h. Subsequently, the cells were plated on the specimens at a density of 3×10^4 cells/mL for cell attachment and a density of 1×10^4 cells/mL for cell proliferation and then cultured in a humidified incubator in an atmosphere containing 5% CO_2 at 37°C for up to 2 days.

The morphologies of the attached cells on the hybrid nanofibrous scaffolds after 6 h of culturing were examined by confocal laser scanning microscopy (CLSM; CI PLUS, Nikon, Tokyo, Japan). For these CLSM observations, the cells on the specimens were fixed in 4% paraformaldehyde in PBS for 10 min, washed in PBS, permeabilized with 0.1% Triton X-100 in PBS for 7 min, washed in PBS and stained with fluorescent phalloidin for 30 min. The cell nuclei were counterstained with DAPI for 5 min. The stained specimens were placed on a cover slide, and the cell morphology was observed.

The cell viability and growth of the hybrid nanofibrous scaffolds after 1 and 2 days of culturing were examined using an MTS (methoxyphenyl tetrazolium salt) assay with 3-(4, 5-dimethylthiazol-2-yl)-5-(3-carboxymethoxyphenyl)-2-(4-sulfophenyl)-2H-tetrazolium (MTS, Celltiter 96 Aqueous

Promega, Madison, WI, USA) for mitochondrial reduction. After 1 and 2 days of culturing, the specimens were washed by PBS and reacted with the MTS solution for 4 h. The quantity of the formazan product, which would be directly proportional to the number of living cells in the culture, was measured by the absorbance at 490 nm using a microplate reader (Model 550; Biorad, Hercules, CA, USA). Four species for each condition were tested to obtain mean and standard deviation. The continued cell proliferation on the TCH-loaded PCL/silica hybrid nanofibrous scaffolds was also evaluated after 7 days of culturing.

2.9. In Vitro Apatite-Forming Ability Evaluation. The *in vitro* apatite-forming ability of the TCH-loaded PCL/silica hybrid nanofibrous scaffolds with various silica sol contents (0 vol%, 10 vol%, 15 vol%, and 20 vol%) was characterized by soaking in a simulated body fluid (SBF) solution for 7 days. The specimens were immersed in the SBF at a concentration of 3 mg mL^{-1} in polyethylene bottles with the initial pH of the solutions being kept at 7.40. The specimens were then placed inside an incubator at a controlled temperature of 37°C for 7 days, extracted, washed three times with ethanol, and then dried at 37°C for 12 h. The formation of the apatite layer on the surface of the hybrid scaffold was examined using FE-SEM and EDS analyses.

2.10. Statistical Analysis. The statistical significance of differences in the data was analyzed using a one-way ANOVA test based on the software Origin Lab 8.0 (Microcal Co, USA). *P* values < 0.05 (*) were considered significant.

3. Results and Discussion

3.1. Hybridization of PCL-Silica-TCH. One of the most important steps for the production of PCL/silica hybrid nanofibrous scaffolds with a controlled release of drug is to prepare homogenous hybrid mixtures. Figure 1 shows a typical optical image of TCH-loaded PCL/silica hybrid mixtures with various silica sol contents (0 vol%, 10 vol%, 15 vol%, and 20 vol%). The TCH-loaded PCL solution was

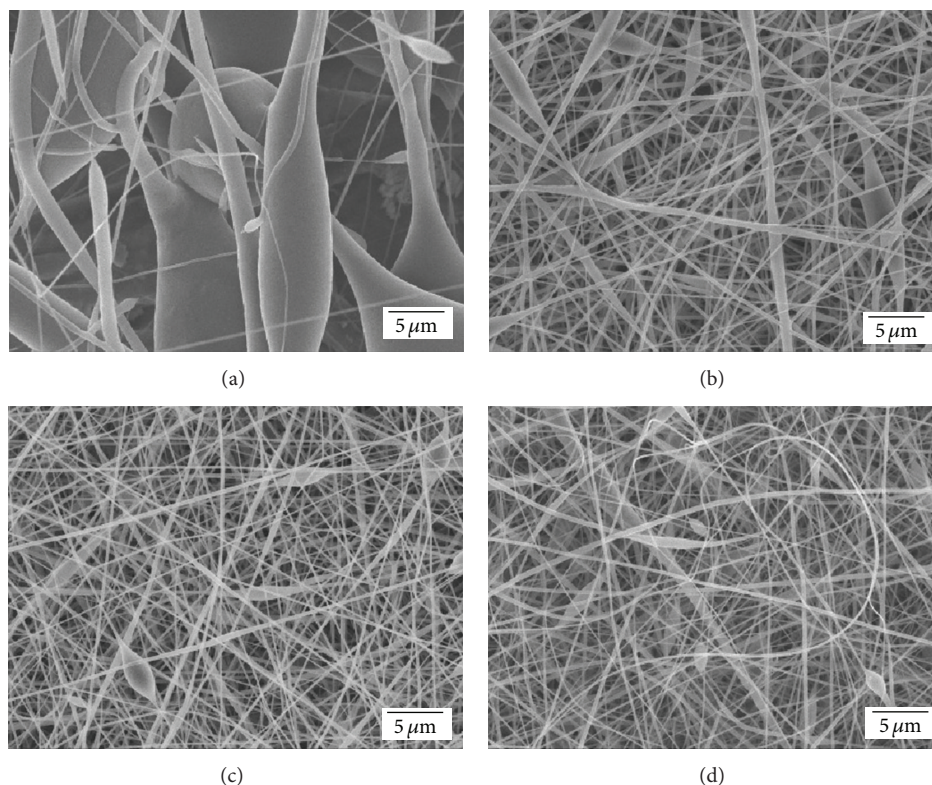


FIGURE 2: Typical FE-SEM images of the TCH-loaded PCL/silica hybrid nanofibrous scaffolds with various silica sol contents of (a) 0 vol%, (b) 10 vol%, (c) 15 vol%, and (d) 20 vol%.

cloudy. Conversely, the TCH-loaded PCL/silica hybrid mixtures turned clear with increasing the silica content. This finding suggests that the hybridization of the PCL solution with the silica sol is highly beneficial to the loading of the TCH drug, which is presumably due to a mesoporous structure of sol-gel derived silica [32].

3.2. Morphology and Nanostructure of Hybrid Nanofibrous Scaffolds. Figures 2(a)–2(d) show typical morphologies of the TCH-loaded PCL/silica hybrid nanofibrous scaffolds with various silica sol contents (0 vol%, 10 vol%, 15 vol%, and 20 vol%). The TCH-loaded PCL nanofibrous scaffold showed a relatively nonuniform fibrous structure (Figure 2(a)), containing large quantities of very thick and flattened fibers. In addition, the TCH drug tended to be segregated from the PCL solution during electrospinning process, resulting in a nonuniform distribution of the TCH drug in the PCL nanofibers. On the other hand, all produced PCL/silica hybrid scaffolds with various silica sol contents (10 vol%, 15 vol%, and 20 vol%) showed a highly uniform, nanofibrous structure (Figures 2(b)–2(d)). This finding suggests that the loading of the TCH drug can be significantly enhanced by hybridizing the PCL solution with the silica sol.

The diameter of the hybrid nanofibers decreased with increasing the initial silica sol content, as shown in Figures 3(A)–3(D). This was mainly attributed to a decrease in the viscosity of the PCL/silica hybrid mixtures. The measured viscosities of the PCL/silica hybrid mixtures with silica

contents of 0 vol%, 10 vol%, 15 vol%, and 20 vol% were 250, 33, 22, and 18 mPa·s, respectively.

The hybridization of the PCL polymer with silica phase was evaluated by TEM, as shown in Figures 4(a) and 4(b). The PCL/silica hybrid nanofibrous scaffold with a highest silica content of 20 vol% showed that the PCL polymer was uniformly hybridized with the silica phase on the nanoscale (Figure 4(a)). In addition, EDS analysis confirmed the presence of the silica phase in the hybrid nanofibers (Figure 4(b)). This finding suggests that PCL polymer can be uniformly hybridized with silica and TCH drug, allowing for the production of TCH-loaded hybrid nanofibrous scaffolds with a controlled micro-/nanostructure.

3.3. Chemical Composition. The presence of the silica phase in the TCH-loaded PCL/silica hybrid nanofibrous scaffolds with various silica sol contents (0 vol%, 10 vol%, 15 vol%, and 20 vol%) was confirmed by EDS analyses, as shown in Figures 5(a)–5(d). The PCL nanofibrous scaffold showed peaks associated with C and O elements (Figure 5(a)), while all produced PCL/silica hybrid nanofibrous scaffolds showed an additional strong peak corresponding to Si element (Figures 5(b)–5(d)). The relative intensities of the peaks associated with Si and O elements increased with increasing the silica content.

The final content of the silica phase in the PCL/silica hybrid nanofibrous scaffolds with various silica sol contents (0 vol%, 10 vol%, 15 vol%, and 20 vol%) was calculated by

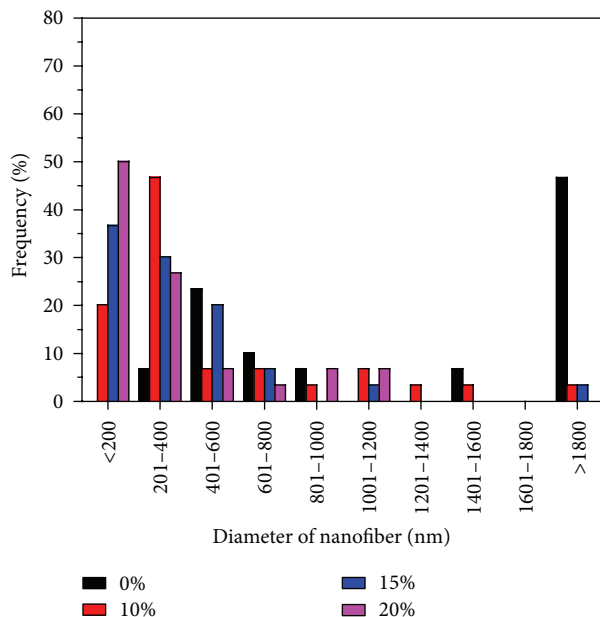


FIGURE 3: The diameter distributions of the PCL/silica hybrid nanofibers with various silica sol contents ((A) 0 vol%, (B) 10 vol %, (C) 15 vol%, and (D) 20 vol%).

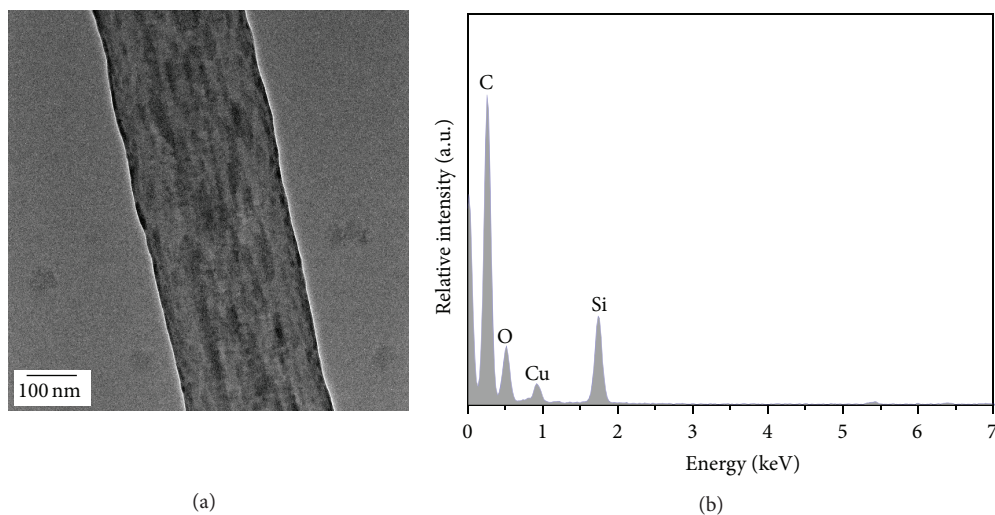


FIGURE 4: (a) TEM image of the PCL/silica hybrid nanofibers produced with a silica content of 20 vol% and (b) EDS spectrum of the nanofiber.

TGA analysis, as shown in Figures 6(A)–6(D). All specimens showed similar thermal behaviors only associated with thermal decomposition of the PCL polymer with negligible thermal change of the silica phase. More specifically, significant weight loss was observed at $\sim 380^{\circ}\text{C}$, attributed to thermal decomposition of the PCL polymer [33, 34]. The final content of the silica phase was 14.5 wt%, 21.0 wt%, and 27.6 wt% for the initial silica sol contents of 10 vol%, 15 vol%, and 20 vol%, respectively, which corresponded well to the originally intended values (i.e., 15.04 wt%, 22.91 wt%, and 28.10 wt%). This finding suggests that the silica phase can be homogeneously hybridized with the PCL polymer without any considerable loss during process.

3.4. Chemical Structure. The chemical structure of the TCH-loaded PCL/silica hybrid nanofibrous scaffolds with various silica sol contents (0 vol%, 10 vol%, 15 vol%, and 20 vol%) was investigated by ATR-FTIR to examine a chemical interaction between the PCL and silica phases, as shown in Figures 7(A)–7(D). The PCL nanofibrous scaffold showed typical bands of PCL polymer, namely, two dominant absorption peaks at 1725 and 1180 cm^{-1} , corresponding to the stretching vibrations of the carboxyl ($\text{C}=\text{O}$) [35] and ether groups ($\text{C}-\text{O}-\text{C}$) [36], respectively (Figure 7(A)). On the other hand, all produced PCL/silica hybrid nanofibrous scaffolds with various silica contents (10 wt%, 15 wt% and 20 wt%) showed additional bands at approximately 1078 , 795 and 453 cm^{-1} ,

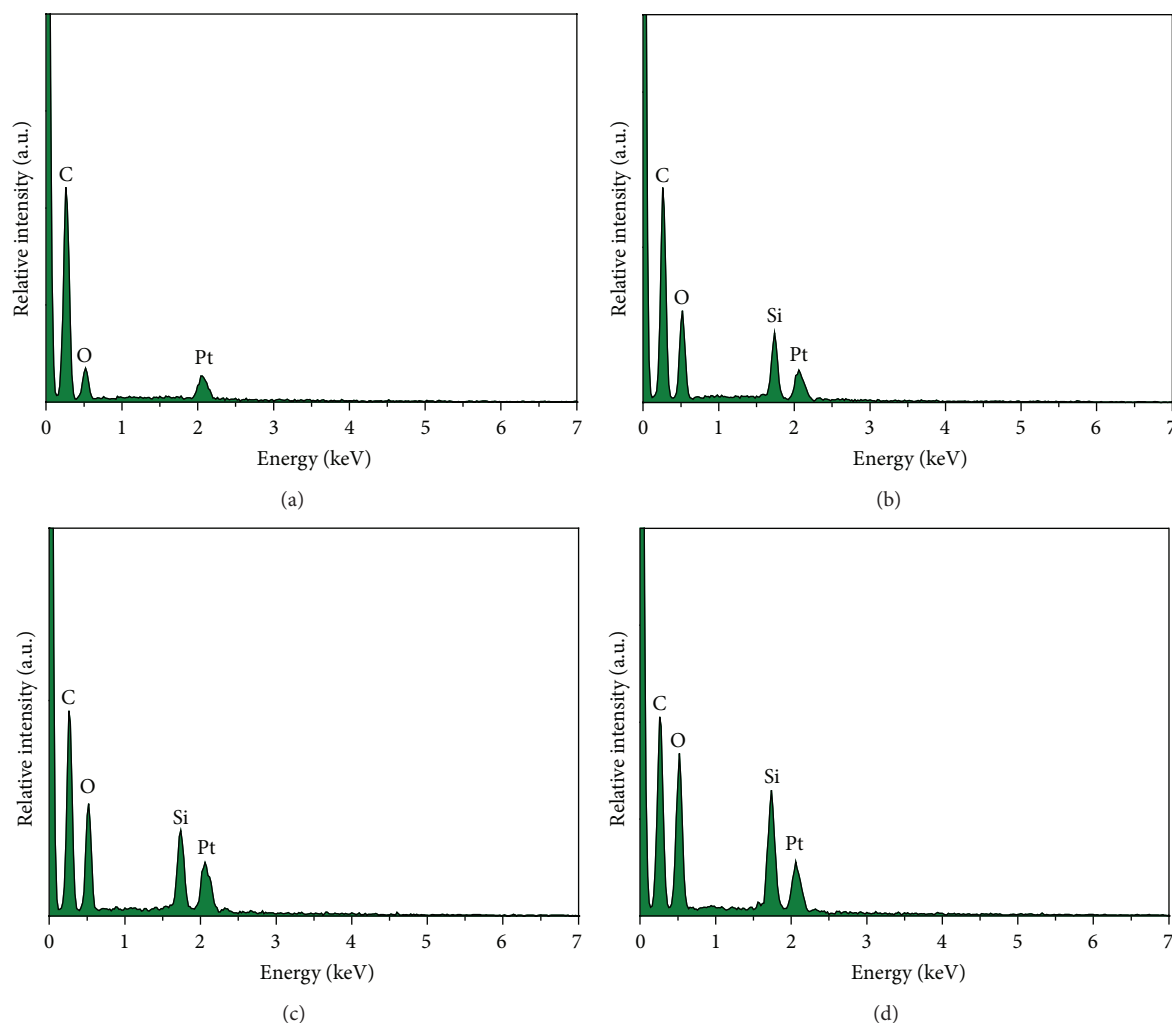


FIGURE 5: Typical EDS spectrums of the TCH-loaded PCL/silica hybrid nanofibrous scaffolds with various silica sol contents of (a) 0 vol%, (b) 10 vol%, (c) 15 vol%, and (d) 20 vol%.

which are representative of the various vibration modes of Si-O-Si bonds [37, 38].

No noticeable band shift was observed, suggesting that the intrinsic characteristics of the PCL and silica phases are preserved.

3.5. Hydrophilicity. The hydrophilicity of the TCH-loaded PCL/silica hybrid nanofibrous scaffolds with various silica contents (0 vol%, 10 vol%, 15 vol%, and 20 vol%) was evaluated by measuring the incident contact angle, as shown in Figure 8. The PCL and PCL/silica hybrid nanofibrous scaffold with an initial silica content of 10 wt% showed relatively high contact angles of $99 \pm 7^\circ$ and $101 \pm 3^\circ$, respectively. However, the PCL/silica hybrid nanofibrous scaffold with an initial silica content of 15 wt% showed a much lower contact angle of $64 \pm 3^\circ$. In addition, the PCL/silica hybrid nanofibrous scaffold with an initial silica content of 20 wt% showed a contact angle near zero; that is, a water droplet quickly spread and penetrated the nanofibrous structure, as is often the case with nanoporous PCL/silica xerogel membranes [39].

However, the contact angle of the dense PCL/silica hybrid films prepared by spin coating technique did not change much, that is, $59 \pm 6^\circ$, $48 \pm 6^\circ$, $51 \pm 4^\circ$, and $56 \pm 6^\circ$ for the hybrid films with silica contents of 0 vol%, 10 vol%, 15 vol%, and 20 vol%, respectively. This was presumably due to the phase separation of the silica phase from the PCL polymer, which differed from PCL/silica composites with a uniform distribution of the silica phase in the PCL polymer that showed significantly enhanced hydrophilicity [39]. However, it is reasonable to suppose that the nanofibrous structure is one of the critical factors for enhancing the hydrophilicity of the PCL/silica hybrid nanofibrous scaffolds.

3.6. Mechanical Properties. The mechanical properties of the TCH-loaded PCL/silica hybrid nanofibrous scaffolds were evaluated at a temperature of $\sim 37^\circ\text{C}$ using tensile strength tests. Figures 9(A)–9(D) show typical stress versus strain responses of the hybrid nanofibrous scaffolds with various silica sol contents (0 vol%, 10 vol%, 15 vol% and 20 vol%). The PCL nanofibrous scaffold showed a typical ductile

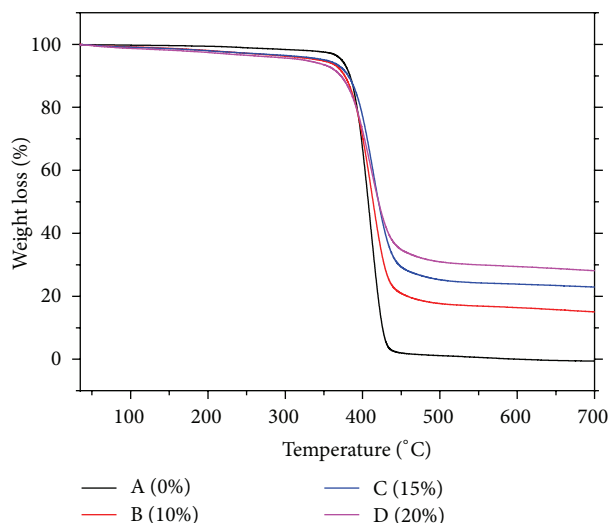


FIGURE 6: Weight losses of the TCH-loaded PCL/silica hybrid nanofibrous scaffolds with various silica sol contents of (A) 0 vol%, (B) 10 vol%, (C) 15 vol%, and (D) 20 vol% as a function of temperature.

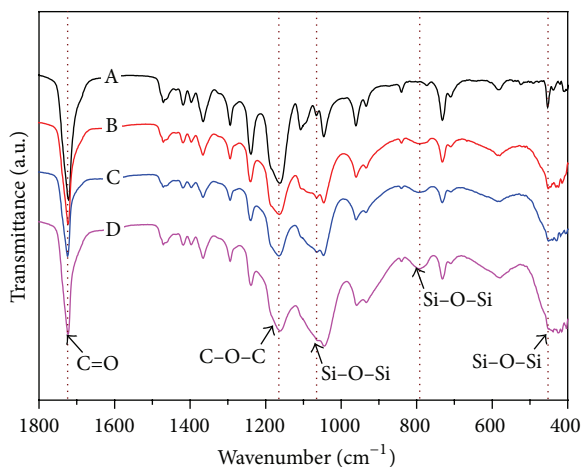


FIGURE 7: Typical ATR-FTIR spectrums of the TCH-loaded PCL/silica hybrid nanofibrous scaffolds with various silica sol contents of (A) 0 vol%, (B) 10 vol%, (C) 15 vol%, and (D) 20 vol%.

fracture behavior of ductile polymers (Figure 9(A)), but relatively low mechanical properties due to its nonuniform nanofibrous structure. On the other hand, the PCL/silica hybrid nanofibrous scaffolds with initial silica sol contents of 10 vol% and 15 vol%, showed much higher maximum stresses with rapid decreases in stress after fracture (Figures 9(B) and 9(C)). However, a higher silica content of 20 vol% considerably decreased the maximum stress and strain at failure (Figure 9(D)).

Table 1 summarizes the ultimate tensile strength, elastic modulus, and strain at failure of the TCH-loaded PCL/silica hybrid nanofibrous scaffolds with various silica sol contents (0 vol%, 10 vol%, 15 vol%, and 20 vol%). The hybrid nanofibrous scaffold with a silica sol content of 15 vol% showed

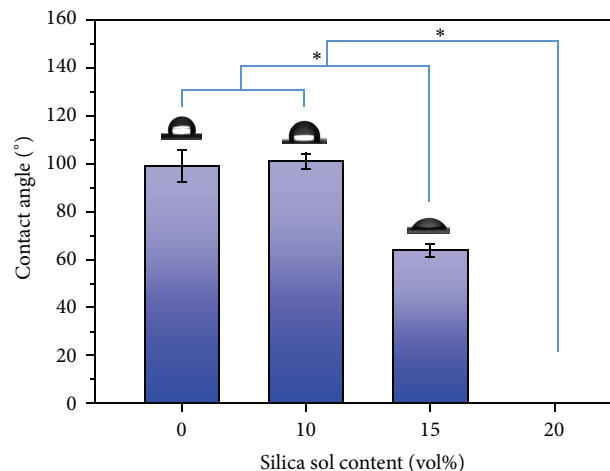


FIGURE 8: Contact angles of the TCH-loaded PCL/silica hybrid nanofibrous scaffolds as a function of the initial silica sol content. The insets show optical images of the water droplets on the hybrid nanofibrous scaffolds.

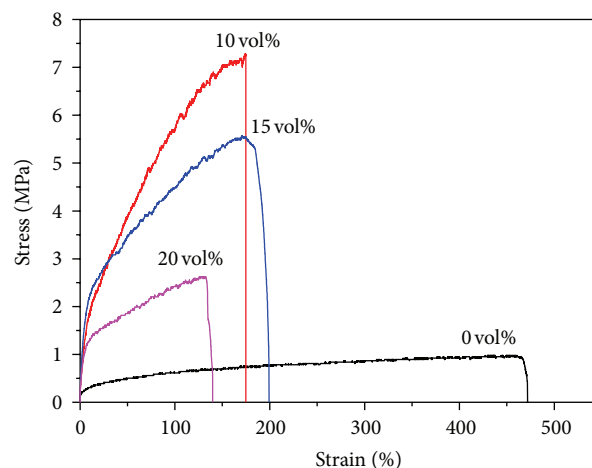


FIGURE 9: Typical stress versus strain responses of the TCH-loaded PCL/silica hybrid nanofibrous scaffolds with various silica sol contents ((A) 0 vol%, (B) 10 vol%, (C) 15 vol%, and (D) 20 vol%).

TABLE 1: Ultimate tensile strength, elastic modulus, and strain at failure of the TCH-loaded PCL/silica hybrid nanofibrous scaffolds with various silica sol contents (0 vol%, 10 vol%, 15 vol%, and 20 vol%).

Silica sol content (vol%)	Ultimate tensile strength (MPa)	Elastic modulus (MPa)	Strain at failure (%)
0	1.1 ± 0.2	1.3 ± 0.3	453 ± 96
10	7.4 ± 0.4	17.5 ± 1.7	193 ± 20
15	5.5 ± 0.3	19.8 ± 2.9	200 ± 35
20	2.8 ± 0.5	21.0 ± 2.2	97 ± 23

reasonably high ultimate tensile strength of 5.5 ± 0.3 MPa, elastic modulus of 19.8 ± 2.9 MPa and strain at failure of $200 \pm 35\%$. This finding suggests that the mechanical properties of the PCL nanofibrous scaffold can be significantly improved

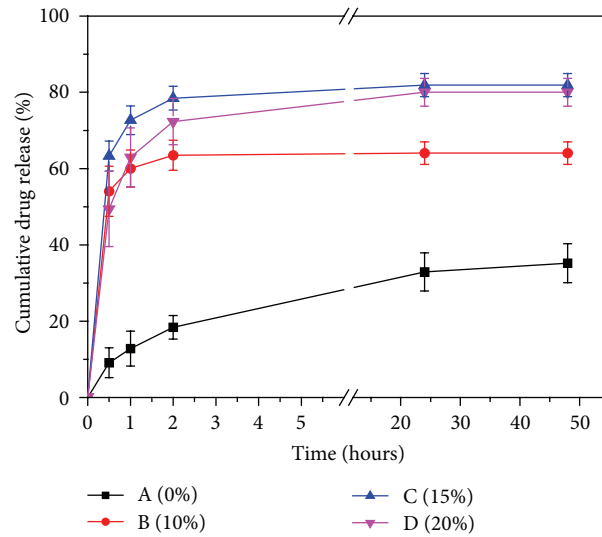


FIGURE 10: Cumulative drug-release profiles of the TCH-loaded PCL/silica hybrid nanofibrous scaffolds with various silica sol contents of (A) 0 vol%, (B) 10 vol%, (C) 15 vol%, and (D) 20 vol%.

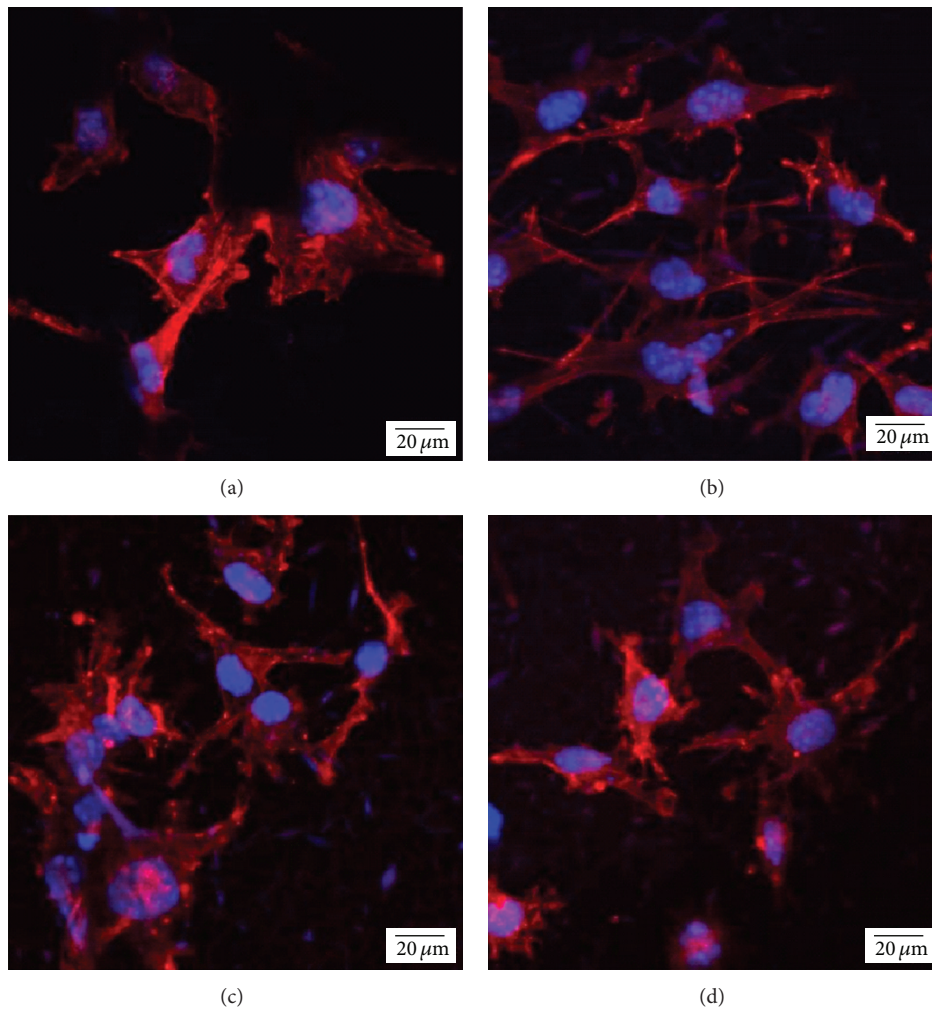


FIGURE 11: Typical CLSM images of the MC3T3-E1 cells attached on the TCH-loaded PCL/silica hybrid nanofibrous scaffolds with various silica sol contents of (a) 0 vol%, (b) 10 vol%, (c) 15 vol%, and (d) 20 vol% after 6 h of culturing.

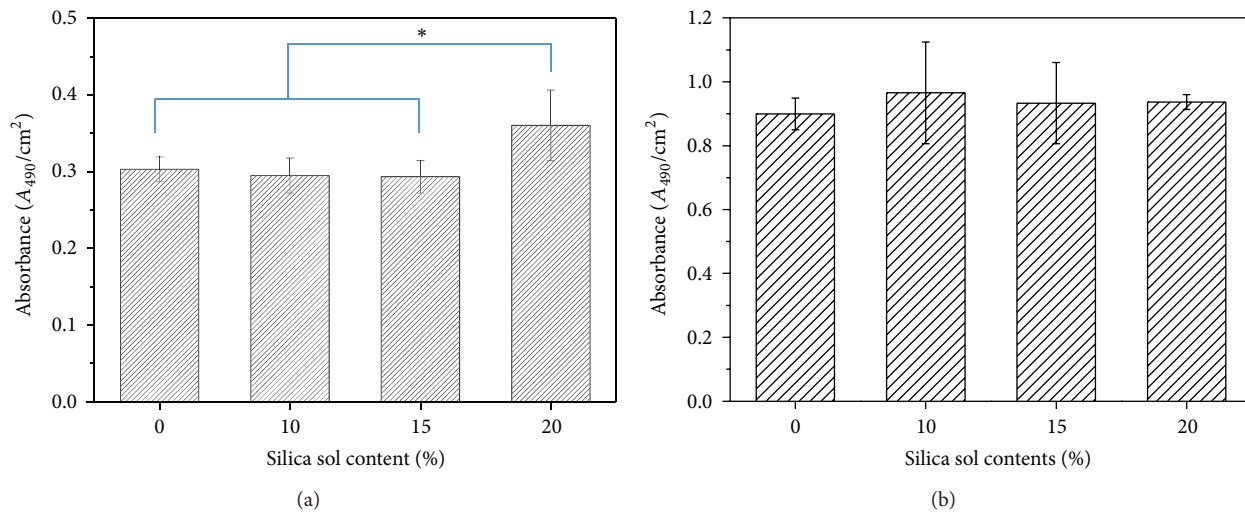


FIGURE 12: Cell viabilities of the MC3T3-E1 cells on the TCH-loaded PCL/silica hybrid nanofibrous scaffolds (a) after 1 day and (b) 2 days of culturing.

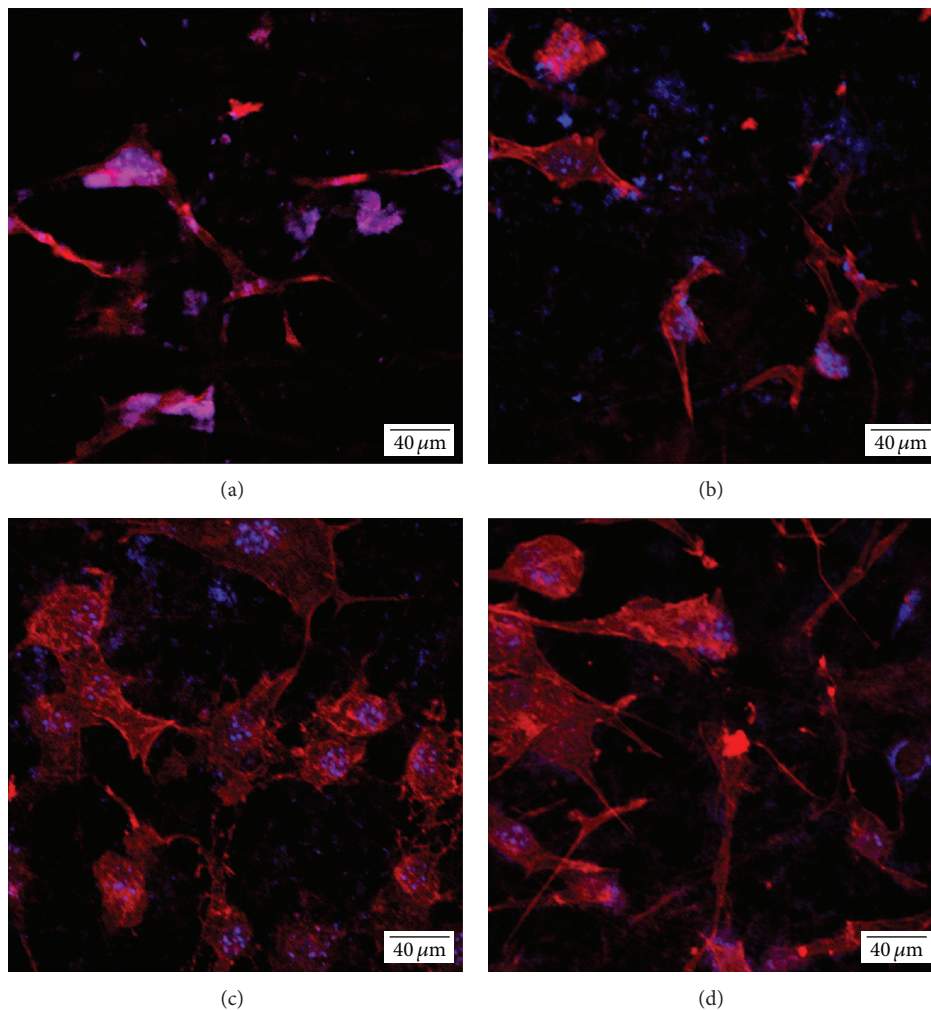


FIGURE 13: CLSM images of the MC3T3-E1 cells on the TCH-loaded PCL/silica hybrid nanofibrous scaffolds with various silica sol contents of (a) 0 vol%, (b) 10 vol%, (c) 15 vol%, and (d) 20 vol% after 7 days of culturing.

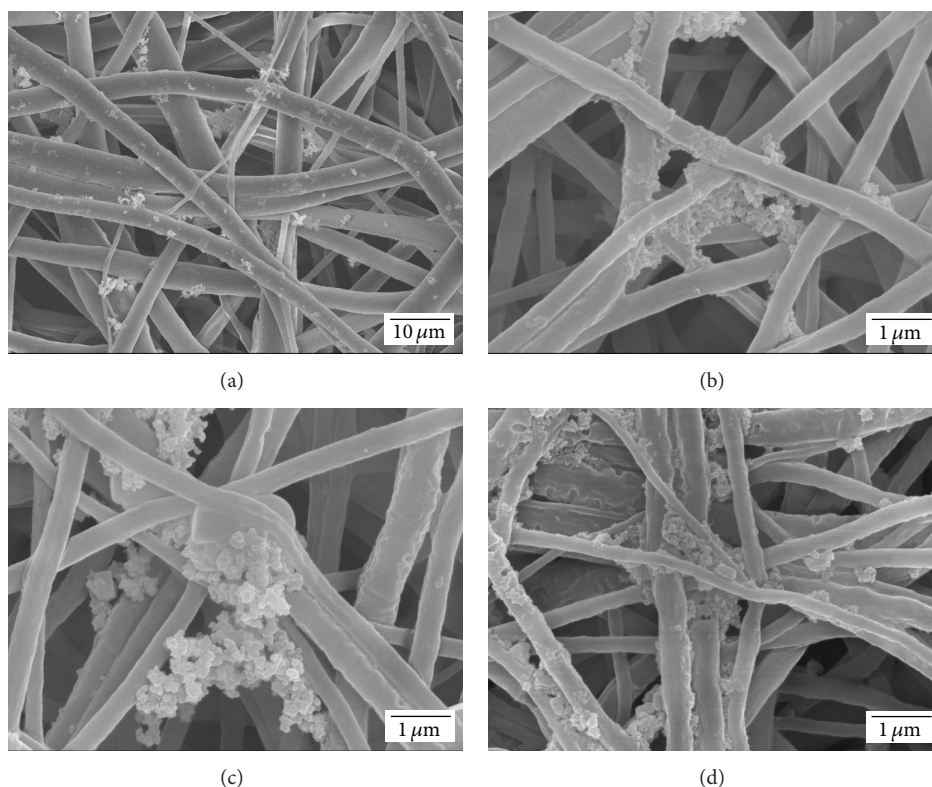


FIGURE 14: FE-SEM images of the TCH-loaded PCL/silica hybrid nanofibrous scaffolds with various silica sol contents of (a) 0 vol%, (b) 10 vol%, (c) 15 vol%, and (d) 20 vol% after immersion in the SBF for 7 days.

by hybridizing the PCL polymer with the sol-gel-derived silica phase [39].

3.7. Drug Release Behavior. The drug release behavior of the TCH-loaded PCL/silica hybrid nanofibrous scaffolds was evaluated in PBS buffer solution over a period of 50 h. Figures 10(A)–10(D) show the cumulative drug-release profiles of the hybrid nanofibrous scaffolds with various silica sol contents (0 vol%, 10 vol%, 15 vol%, and 20 vol%). The PCL/silica hybrid nanofibrous scaffolds showed much higher release rate of the TCH than the PCL nanofibrous scaffold. This was presumably attributed to both an increase in hydrophilicity of the PCL/silica hybrid nanofibers and faster degradation behavior of the silica phase. In addition, it should be noted that the hybrid nanofibrous scaffolds would have much higher release rate than relatively dense hybrids owing to their high surface-to-volume ratio. The cumulative maximum amounts of the TCH released from the PCL/silica hybrid nanofibrous scaffolds with initial silica sol contents of 0 vol%, 10 vol%, 15 vol%, and 20 vol% were $35 \pm 5\%$, $64 \pm 3\%$, $82 \pm 3\%$, and $80 \pm 4\%$, respectively. As mentioned earlier, the TCH drug tended to be segregated from the PCL solution during electrospinning process, resulting in a lower loading efficiency of the TCH into the PCL nanofibers. However, the loading efficiency is considerably enhanced by hybridizing the PCL polymer with the silica phase.

3.8. In Vitro Biocompatibility. The *in vitro* biocompatibility of the TCH-loaded PCL/silica hybrid nanofibrous scaffolds was assessed by *in vitro* cell tests using MC3T3-E1 cells. Figures 11(a)–11(d) show typical CLSM images of the cells attached to the hybrid nanofibrous scaffolds with various silica sol contents (0 vol%, 10 vol%, 15 vol%, and 20 vol%) after 6 h of culturing. The red and blue colors represent the actin and nucleus, respectively. Basically, all hybrid nanofibrous scaffolds showed that the cells are actively attached and spread on the surface, suggesting good biocompatibility.

The absorbance values, which represent the degree of cell proliferation, on the TCH-loaded PCL/silica hybrid nanofibrous scaffolds with various silica sol contents (0 vol%, 10 vol%, 15 vol%, and 20 vol%) were examined after 1 and 2 days of culturing using an MTS assay, as shown in Figures 12(a) and 12(b). The hybrid nanofibrous scaffolds with silica contents of 0 vol%, 10 vol%, and 15 vol% showed similar absorbance values after 1 day of culturing, while the scaffold with a highest silica content of 20 vol% showed a higher absorbance value (Figure 12(a)). In addition, the absorbance values increased remarkably after 2 days of culturing for all produced hybrid nanofibrous scaffolds (Figure 12(b)). This finding suggests that the loading of the TCH drug into PCL/silica hybrid nanofibrous scaffolds has no negative effects on the growth of osteoblasts, allowing for good biocompatibility [40].

The continued cell proliferation on the TCH-loaded PCL/silica hybrid nanofibrous scaffolds was evaluated after 7 days of culturing, as shown in Figures 13(a)–13(d). The hybrid nanofibrous scaffolds with higher silica contents (15 vol% and 20 vol%) showed more active extensions and bridging of extracellular matrix (ECM) (Figures 13(c) and 13(d)), representing the early stage of mineralization of MC3T3-E1 cells [41]. It should be noted that TCH-loaded PCL/silica hybrid nanofibrous scaffolds would show excellent bone regeneration *in vivo*, as is often the case with nanoporous PCL/silica xerogel membranes [39].

3.9. In Vitro Apatite-Forming Ability. The *in vitro* mineralization behavior of the TCH-loaded PCL/silica hybrid nanofibrous scaffolds, one of the most important key markers for representing the ability to induce new bone tissue formation *in vivo*, was more closely evaluated using SBF solution. Figures 14(a)–14(b) show typical SEM images of the hybrid nanofibrous scaffolds with various silica contents (0 vol%, 10 vol%, 15 vol%, and 20 vol%) after immersion in the SBF solution for 7 days. Compared to the PCL scaffold, the hybrid scaffolds showed more vigorous precipitation of apatite crystals, suggesting significantly enhanced mineralization ability owing to the excellent apatite-forming ability of the silica phase.

4. Conclusions

TCH-loaded PCL/silica hybrid nanofibrous scaffolds with various silica sol contents (10 vol%, 15 vol%, and 20 vol%) were successfully produced using ES. The silica phase was homogeneously hybridized with the PCL polymer, while their intrinsic characteristics were preserved. This significantly improved the hydrophilic nature and mechanical properties of the hybrid nanofibrous scaffolds. The hybrid nanofibrous scaffold with an initial silica sol content of 15 vol% had reasonably high ultimate tensile strength of 5.5 ± 0.3 MPa and elastic modulus of 19.8 ± 2.9 MPa as well as a low contact angle of $64 \pm 3^\circ$. In addition, the hybrid nanofibrous scaffolds showed much higher release rate and maximum amounts of the TCH than the PCL nanofibrous scaffold. Regardless of the silica content, all produced hybrid nanofibrous scaffolds showed biocompatibility assessed in terms of the proliferation of pre-osteoblast cells. These findings suggest that TCH-loaded PCL/silica hybrid nanofibrous scaffolds have great potential as a membrane for guided bone regeneration (GBR).

Conflict of Interests

The authors declare that there are no conflicts of interest.

Acknowledgment

This research was supported by Korea Healthcare technology R&D Project, Ministry of Health and Welfare, Republic of Korea (Contract Grant no. H11C0388).

References

- [1] M. M. Stevens and J. H. George, "Exploring and engineering the cell surface interface," *Science*, vol. 310, no. 5751, pp. 1135–1138, 2005.
- [2] S. Gronthos, P. J. Simmons, S. E. Graves, and P. G. Robey, "Integrin-mediated interactions between human bone marrow stromal precursor cells and the extracellular matrix," *Bone*, vol. 28, no. 2, pp. 174–181, 2001.
- [3] M. P. Lutolf and J. A. Hubbell, "Synthetic biomaterials as instructive extracellular microenvironments for morphogenesis in tissue engineering," *Nature Biotechnology*, vol. 23, no. 1, pp. 47–55, 2005.
- [4] M. Schindler, I. Ahmed, J. Kamal et al., "A synthetic nanofibrillar matrix promotes *in vivo*-like organization and morphogenesis for cells in culture," *Biomaterials*, vol. 26, no. 28, pp. 5624–5631, 2005.
- [5] D. Ishii, T. H. Ying, A. Mahara et al., "*In vivo* tissue response and degradation behavior of PLLA and stereocomplexed PLA nanofibers," *Biomacromolecules*, vol. 10, no. 2, pp. 237–242, 2009.
- [6] W. Teo, W. He, and S. Ramakrishna, "Electrospun scaffold tailored for tissue-specific extracellular matrix," *Biotechnology Journal*, vol. 1, no. 9, pp. 918–929, 2006.
- [7] S. Agarwal, J. H. Wendorff, and A. Greiner, "Progress in the field of electrospinning for tissue engineering applications," *Advanced Materials*, vol. 21, no. 32–33, pp. 3343–3351, 2009.
- [8] J. H. Jang, O. Castano, and H. W. Kim, "Electrospun materials as potential platforms for bone tissue engineering," *Advanced Drug Delivery Reviews*, vol. 61, no. 12, pp. 1065–1083, 2009.
- [9] E. R. Kenawy, G. L. Bowlin, K. Mansfield et al., "Release of tetracycline hydrochloride from electrospun poly(ethylene-co-vinylacetate), poly(lactic acid), and a blend," *Journal of Controlled Release*, vol. 81, no. 1–2, pp. 57–64, 2002.
- [10] P. Taepaiboon, U. Rungsardthong, and P. Supaphol, "Drug-loaded electrospun mats of poly(vinyl alcohol) fibres and their release characteristics of four model drugs," *Nanotechnology*, vol. 17, no. 9, pp. 2317–2329, 2006.
- [11] K. Kanawung, K. Panitchanapan, S. Puangmalee et al., "Preparation and characterization of polycaprolactone/ diclofenac sodium and poly(vinyl alcohol)/tetracycline hydrochloride fiber mats and their release of the model drugs," *Polymer Journal*, vol. 39, no. 4, pp. 369–378, 2007.
- [12] Z. X. Meng, W. Zheng, L. Li, and Y. F. Zheng, "Fabrication, characterization and *in vitro* drug release behavior of electrospun PLGA/chitosan nanofibrous scaffold," *Materials Chemistry and Physics*, vol. 125, no. 3, pp. 606–611, 2011.
- [13] P. Zahedi, Z. Karami, I. Rezaeian et al., "Preparation and performance evaluation of tetracycline hydrochloride loaded wound dressing mats based on electrospun nanofibrous poly(lactic acid)/poly(ϵ -caprolactone) blends," *Journal of Applied Polymer Science*, vol. 124, no. 5, pp. 4174–4183, 2012.
- [14] L. A. Mary, T. Senthilram, S. Suganya et al., "Centrifugal spun ultrafine fibrous web as a potential drug delivery vehicle," *Express Polymer Letters*, vol. 7, pp. 238–248, 2013.
- [15] A. M. Le Ray, S. Chiffolleau, P. Iooss et al., "Vancomycin encapsulation in biodegradable poly(ϵ -caprolactone) microparticles for bone implantation. Influence of the formulation process on size, drug loading, *in vitro* release and cytocompatibility," *Biomaterials*, vol. 24, no. 3, pp. 443–449, 2003.
- [16] L. Meseguer-Olmo, M. J. Ros-Nicolás, M. Clavel-Sainz et al., "Biocompatibility and *in vivo* gentamicin release from bioactive

- sol-gel glass implants,” *Journal of Biomedical Materials Research*, vol. 61, no. 3, pp. 458–465, 2002.
- [17] W. J. Li, K. G. Danielson, P. G. Alexander, and R. S. Tuan, “Biological response of chondrocytes cultured in three-dimensional nanofibrous poly(ϵ -caprolactone) scaffolds,” *Journal of Biomedical Materials Research A*, vol. 67, no. 4, pp. 1105–1114, 2003.
- [18] H. Yoshimoto, Y. M. Shin, H. Terai, and J. P. Vacanti, “A biodegradable nanofiber scaffold by electrospinning and its potential for bone tissue engineering,” *Biomaterials*, vol. 24, no. 12, pp. 2077–2082, 2003.
- [19] M. Shin, H. Yoshimoto, and J. P. Vacanti, “*In vivo* bone tissue engineering using mesenchymal stem cells on a novel electrospun nanofibrous scaffold,” *Tissue Engineering*, vol. 10, no. 1–2, pp. 33–41, 2004.
- [20] M. S. Khil, S. R. Bhattarai, H. Y. Kim, S. Kim, and K. Lee, “Novel fabricated matrix via electrospinning for tissue engineering,” *Journal of Biomedical Materials Research B*, vol. 72, no. 1, pp. 117–124, 2005.
- [21] K. Fujihara, M. Kotaki, and S. Ramakrishna, “Guided bone regeneration membrane made of polycaprolactone/calcium carbonate composite nano-fibers,” *Biomaterials*, vol. 26, no. 19, pp. 4139–4147, 2005.
- [22] P. Wutticharoenmongkol, N. Sanchavanakit, P. Pavasant, and P. Supaphol, “Novel bone scaffolds of electrospun polycaprolactone fibers filled with nanoparticles,” *Journal of Nanoscience and Nanotechnology*, vol. 6, no. 2, pp. 514–522, 2006.
- [23] C. Erisken, D. M. Kalyon, and H. Wang, “Functionally graded electrospun polycaprolactone and β -tricalcium phosphate nanocomposites for tissue engineering applications,” *Biomaterials*, vol. 29, no. 30, pp. 4065–4073, 2008.
- [24] E. M. Valliant and J. R. Jones, “Softening bioactive glass for bone regeneration: sol-gel hybrid materials,” *Soft Matter*, vol. 7, no. 11, pp. 5083–5095, 2011.
- [25] E. J. Lee, S. H. Teng, T. S. Jang et al., “Nanostructured poly(ϵ -caprolactone)-silica xerogel fibrous membrane for guided bone regeneration,” *Acta Biomaterialia*, vol. 6, no. 9, pp. 3557–3565, 2010.
- [26] T. S. Jang, E. J. Lee, J. H. Jo et al., “Fibrous membrane of nano-hybrid poly-L-lactic acid/silica xerogel for guided bone regeneration,” *Journal of Biomedical Materials Research B*, vol. 100, no. 2, pp. 321–330, 2012.
- [27] B. Lei, K. H. Shin, D. Y. Noh et al., “Nanofibrous gelatin-silica hybrid scaffolds mimicking the native extracellular matrix (ECM) using thermally induced phase separation,” *Journal of Materials Chemistry*, vol. 22, pp. 14133–14140, 2012.
- [28] Y. Wu, C. Wu, Y. Li, T. Xu, and Y. Fu, “PVA-silica anion-exchange hybrid membranes prepared through a copolymer crosslinking agent,” *Journal of Membrane Science*, vol. 350, no. 1–2, pp. 322–332, 2010.
- [29] S. Cheng, D. Shen, X. Zhu, X. Tian, D. Zhou, and L. Fan, “Preparation of nonwoven polyimide/silica hybrid nanofibrous fabrics by combining electrospinning and controlled in situ sol-gel techniques,” *European Polymer Journal*, vol. 45, no. 10, pp. 2767–2778, 2009.
- [30] D. Cao, Y. P. Wu, Z. F. Fu et al., “Cell adhesive and growth behavior on electrospun nanofibrous scaffolds by designed multifunctional composites,” *Colloids and Surfaces B*, vol. 84, no. 1, pp. 26–34, 2011.
- [31] R. R. Duling, R. B. Dupaux, N. Katsube, and J. Lannutti, “Mechanical characterization of electrospun polycaprolactone (PCL): a potential scaffold for tissue engineering,” *Journal of Biomechanical Engineering*, vol. 130, no. 1, Article ID 011006, 2008.
- [32] V. Pillay, C. Dott, Y. E. Choonara et al., “A review of the effect of processing variables on the fabrication of electrospun nanofibers for drug delivery applications,” *Journal of Nanomaterials*, vol. 2013, Article ID 789289, 22 pages, 2013.
- [33] A. Mohamed, V. L. Finkenstadt, S. H. Gordon, G. Biresaw, E. Palmquist Debra, and P. Rayas-Duarte, “Thermal properties of PCL/gluten bioblends characterized by TGA, DSC, SEM, and infrared-PAS,” *Journal of Applied Polymer Science*, vol. 110, no. 5, pp. 3256–3266, 2008.
- [34] S. Sayyar, E. Murray, B. C. Thompson, S. Gambhir, D. L. Officer, and G. G. Wallace, “Covalently linked biocompatible graphene/polycaprolactone composites for tissue engineering,” *Carbon*, vol. 52, pp. 296–304, 2013.
- [35] J. L. E. Ivirico, M. S. Sánchez, R. Sabater i Serra, J. M. M. Dueñas, J. L. G. Ribelles, and M. M. Pradas, “Structure and properties of poly(ϵ -caprolactone) networks with modulated water uptake,” *Macromolecular Chemistry and Physics*, vol. 207, no. 23, pp. 2195–2205, 2006.
- [36] D. Verma, K. Katti, and D. Katti, “Bioactivity in in situ hydroxyapatite-polycaprolactone composites,” *Journal of Biomedical Materials Research A*, vol. 78, no. 4, pp. 772–780, 2006.
- [37] S. H. Jun, E. J. Lee, S. W. Yook, H. E. Kim, H. W. Kim, and Y. H. Koh, “A bioactive coating of a silica xerogel/chitosan hybrid on titanium by a room temperature sol-gel process,” *Acta Biomaterialia*, vol. 6, no. 1, pp. 302–307, 2010.
- [38] A. Fidalgo and L. M. Ilharco, “The influence of the wet gels processing on the structure and properties of silica xerogels,” *Microporous and Mesoporous Materials*, vol. 84, no. 1–3, pp. 229–235, 2005.
- [39] E. J. Lee, S. H. Teng, T. S. Jang et al., “Nanostructured poly(ϵ -caprolactone)-silica xerogel fibrous membrane for guided bone regeneration,” *Acta Biomaterialia*, vol. 6, no. 9, pp. 3557–3565, 2010.
- [40] L. F. Zhang, R. Sun, L. Xu et al., “Hydrophilic poly (ethylene glycol) coating on PDLLA/BCP bone scaffold for drug delivery and cell culture,” *Materials Science and Engineering C*, vol. 28, no. 1, pp. 141–149, 2008.
- [41] J. P. St-Pierre, M. Gauthier, L. P. Lefebvre, and M. Tabrizian, “Three-dimensional growth of differentiating MC3T3-E1 pre-osteoblasts on porous titanium scaffolds,” *Biomaterials*, vol. 26, no. 35, pp. 7319–7328, 2005.

Research Article

A Mucoadhesive Electrospun Nanofibrous Matrix for Rapid Oramucosal Drug Delivery

Clare Dott, Charu Tyagi, Lomas K. Tomar, Yahya E. Choonara, Pradeep Kumar, Lisa C. du Toit, and Viness Pillay

Department of Pharmacy and Pharmacology, Faculty of Health Sciences, University of the Witwatersrand, 7 York Road, Parktown, Johannesburg 2193, South Africa

Correspondence should be addressed to Viness Pillay; viness.pillay@wits.ac.za

Received 15 July 2013; Accepted 29 August 2013

Academic Editor: Tong Lin

Copyright © 2013 Clare Dott et al. This is an open access article distributed under the Creative Commons Attribution License, which permits unrestricted use, distribution, and reproduction in any medium, provided the original work is properly cited.

A nanofibrous matrix system (NFMS), consisting of a drug-loaded nanofiber layer, was electrospun directly onto a polymeric backing film, the latter of which was formulated and optimized according to a 3-level, 3-factor Box-Behnken experimental design. The dependent variables, fill volume, hydroxypropylmethylcellulose (HPMC) concentration, and glycerol concentration, were assessed for their effects on measured responses, disintegration time, work of adhesion, force of adhesion, dissolution area under curve (AUC) at 1 minute, and permeation AUC at 3 minutes. Physicochemical and physicochemical properties of the developed system were studied by rheology, FTIR, toughness determination, mucoadhesion, and nanotensile testing. Data obtained from the physicochemical characterization confirmed the suitability of NFMS for application in oramucosal drug delivery. The optimized NFMS showed the drug entrapment of 2.3 mg/1.5 cm² with disintegration time of 12.8 seconds. Electrospinning of drug-loaded polyvinylalcohol (PVA) fibers resulted in a matrix with an exceedingly high surface-area-to-volume ratio, which enhanced the rate of dissolution for rapid oramucosal drug delivery. To corroborate with the experimental studies, the incorporation of glycerol with HPMC and PVA blend was mechanistically elucidated using computer-assisted modeling of the 3D polymeric architecture of the respective molecular complexes to envisage the likely alignment of the polymer morphologies affecting the performance of the nanofibrous device.

1. Introduction

Electrospinning has gleaned considerable interest in the field of drug delivery due to its proficiency in producing fibers with eminently small diameters. The process of electrospinning involves applying an electrical potential to a polymer solution in order to produce very fine fibers in the nano- and micrometer size range. When a drop of polymer solution at the end of a capillary tube is subjected to an electrical potential, the drop elongates, becoming conical in shape, and once the electrical field exceeds surface tension, a fiber jet is ejected from the tip of the cone [1–3]. As the fiber jet travels through the atmosphere, the solvent evaporates, and solid polymer fibers are deposited on a grounded collector, closing the gap between the capillary and collector, and hence completing the circuit [3, 4]. If the polymer concentration, and hence viscosity and chain entanglements, is too low, the jet will break up into droplets before reaching the collector [5, 6].

However, as the concentration is increased, the viscosity will increase, and chain entanglements will become sufficient for fiber formation, resulting in a whipping motion of the jet and stretching and thinning of the fiber on application of a potential. Electrospun fibers display a small diameter and extremely high surface area to mass ratio [7, 8]. This is advantageous in drug delivery as it results in an increase in the total drug release from drug-loaded fibers when compared to cast films of the same composition, which have a considerably smaller surface area [9, 10]. Furthermore, a large exposed surface area can greatly improve the dissolution rate, and hence bioavailability, of a drug [11–14]. For adequate drug absorption to occur via the buccal mucosa, it is necessary for the drug concentration within the oral cavity to be high. Accelerated disintegration of an orally dissolving drug delivery system results in a high concentration of drug at the surface of absorption and therefore rapid and extensive absorption [15, 16]. Furthermore, rapid absorption leads to

expeditious blood levels and hence a prompt onset of action [17–20]. It has been demonstrated that the *in vivo* availability of a drug administered via the oramucosal route is greatly dependent on the disintegration rate of the drug delivery system [15].

During electrospinning, the polymer chain orientation that occurs during fiber formation has a significant effect on the physicochemical properties of the nanofibrous matrix that is formed [21]. The fiber diameter has been found to affect the mechanical properties of electrospun materials [22], where fibers with smaller diameters displayed a greater strength but were less pliable than larger fibers [23]. The physicochemical properties of a material have a significant effect on drug release [24], patient acceptability [25], and residence time at the site of absorption [26, 27]. Due to the relatively short residence time of an oramucosally administered drug delivery system at the site of absorption, mucoadhesion is often required [15]. Mucoadhesive drug delivery systems are advantageous in that the entire system is rendered immobile, an intimate contact between the system and buccal mucosa is created, and a high drug concentration at the absorption surface is achieved [15, 27]. This results in a reduction in the required drug concentration as well as an improved bioavailability [27]. Thin, mucoadhesive films are favorable for oramucosal drug delivery due to the flexible nature and high contact surface area of such films [15, 28].

Statistical optimization, by experimental design, employs mathematical equations and graphic analysis in order to characterize and assess the effects of independent variables on measured responses [29] and was applied to this investigation. In contrast to traditional approaches to formulation optimization, where one variable is assessed at a time, statistical optimization utilizes fewer experimental runs, which is less time consuming and provides a true optimized formulation by a systematic approach [29].

In the work outlined in this study, drug-loaded fibers were electrospun directly onto a statistically optimized polymeric backing film in order to form a porous, rapidly disintegrating nanofibrous matrix system (NFMS) for oramucosal drug delivery. The polymeric backing film was produced according to a Box-Behnken experimental design. The polyvinylalcohol (PVA) electrospun fibers were loaded with model drug, diphenhydramine, in order to assess drug entrapment, release, and permeation characteristics. Drug-loaded films, serving as a comparison, were also prepared according to the same formula as the backing film and using the same constituents as the electrospinning solution. The effects of varying polymeric constituents on drug release, drug permeation, mucoadhesion, and disintegration were also investigated in order to produce an optimized oramucosal drug delivery system

2. Materials and Methods

2.1. Materials. Polyvinylalcohol (PVA) (87–89% hydrolyzed, Mw 13,000–23,000 g/mol) and diphenhydramine (DPH) were purchased from Sigma-Aldrich (St. Louis, MO, USA). Propan-2-ol, glycerol, and citric acid were purchased from

TABLE 1: Polymer concentrations and volumes used in film preparation according to a Box-Behnken design.

Formulation number	Fill volume (mL)	HPMC (%w/v)	Glycerol (%w/w of PVA + HPMC)
D1	40	0.50	12.5
D2	100	0.25	15.0
D3	40	0.25	15.0
D4	70	0.25	12.5
D5	70	0.50	10.0
D6	100	0.50	12.5
D7	40	0.25	10.0
D8	70	0.25	12.5
D9	70	0.00	10.0
D10	100	0.00	12.5
D11	70	0.00	15.0
D12	70	0.25	12.5
D13	70	0.50	15.0
D14	40	0.00	12.5
D15	100	0.25	10.0

Rochelle Chemicals (Johannesburg, South Africa). Hydroxypropylmethylcellulose (HPMC) was purchased from Colorcon Limited (London, England).

2.2. Preparation of Polymeric Backing Films by Film Casting. Films intended as backing and mucoadhesive layers for electrospun fibers were prepared according to a Box-Behnken experimental design. Polymer solutions were prepared by dissolving glycerol, PVA, and HPMC in a 4:1 mixture of deionized water and propan-2-ol. The concentrations and volumes used were as outlined in Table 1. For all the formulations the PVA concentration was used at 1% w/v. Solutions were syringed into rectangular flat-bottomed moulds and left under an extractor at 21°C for 48 hours in order that complete solvent evaporation and film formation could occur. For comparative purposes, a DPH-loaded film (FD) containing the same polymeric and plasticizer constituents was prepared.

2.2.1. Experimental Design. A 3-factor Box-Behnken experimental design was generated by Minitab, V15 (Minitab Inc., PA, USA), in order to statistically optimize the polymeric film layer and analyze the effect of formulation variables on system disintegration and drug release. The independent variables X_1 , X_2 , and X_3 are outlined in Table 2. Y_1 through to Y_5 , the dependent variables, were disintegration time, work of adhesion (WA), maximum detachment force (MDF), dissolution area under the curve (AUC) at 1 minute (AUC_D), and permeation AUC at 3 minutes (AUC_P), respectively [30–32].

2.3. Preparation of Nanofibers by Electrospinning. A drug-loaded solution for electrospinning was produced by dissolving PVA, citric acid, DPH, and glycerol in a 2:1 mixture of water and propan-2-ol at concentrations of 25% w/v,

TABLE 2: Test parameters employed in biaxial extensibility testing.

Parameter	Setting
Test mode	Compression
Pretest speed	1 mm/s
Test speed	1 mm/s
Posttest speed	1 mm/s
Target mode	Distance
Distance	10 mm
Trigger force	0.5 N

2% w/v, 10% w/v, and 0.5% v/v, respectively. These quantities were based on optimal fiber production, reproducibility, and drug-loading proficiencies as will be explained later in the paper. The solution was placed in a 5 mL pipette, which was fitted into the adjustable supporting bracket of an electrospinning device. Electrospinning of the solution was performed at 20 kV with a tip-to-collector distance of 11 cm, using a custom-built electrospinning device (RGC Engineering Sales Division, Johannesburg, South Africa) equipped with a voltmeter and MJ Series High Voltage Power Supply (Glassman High Voltage Inc., NJ, USA). Fibers were collected on the polymeric backing film secured on aluminum foil-lined board which formed the complete NFMS. Samples were cut into sections. For comparative purposes, a film (FE) was prepared with the same drug/polymer ratio as the electrospinning solution.

2.4. Characterization

2.4.1. Scanning Electron Microscopy of the Drug-Loaded Fiber Layer. The surface structure of the electrospun fibers was analyzed by images produced by scanning electron microscopy (SEM), using a Phenom Microscope (FEI Company, Hillsboro, OR, USA). Samples were mounted on stubs and sputter-coated with gold prior to examination.

2.4.2. FTIR Spectroscopy. FTIR spectroscopy was performed in order to assess structural changes that may have occurred in the polymeric backbone due to interactions of excipients, drugs, or polymers during film or fiber formation. A Spectrum 100 FT-IR Spectrometer (PerkinElmer Inc., Waltham, MA, USA) was used to assess vibration characteristics of chemical functional groups of samples in response to reactions with infrared light.

2.4.3. Rheological Studies of the Components of the NFMS. The rheological properties of polymer solutions and hydrated NFMS, FD, and FE samples were determined with the use of a Haake Modular Advanced Rheometer System (ThermoFisher Scientific, Karlsruhe, Germany). The stress-strain rheological parameters of the polymer solution have an influence on drug release, electrospinning, palatability, and effect on saliva, and they are important factors when considering the desired characteristics of the system. Samples were analyzed by placing the polymer solution or NFMS/film sample, hydrated in 1 mL simulated saliva (pH 6.75), on the sample stage and immersing the spindle in the fluid. The shear rate was

ramped from 0 to 500/s, and the shear forces and viscosities of the samples were measured at 37°C for the NFMS and film samples and at 25°C for the electrospinning solution. The thixotropy of the 25% w/v PVA electrospinning solution was determined by ramping the shear rate from 0 to 50/s over 60 seconds, holding for 60 seconds and then decreasing back to 0/s over 60 seconds. Oscillation studies were carried out by subjecting samples to oscillating stresses or strains. Oscillation measurements were used to determine the storage modulus, G' , and the loss modulus, G'' , as a function of angular frequency, ω . Oscillation tests provide information on sample elasticity and viscosity related to the applied frequency.

2.4.4. Microenvironmental Surface pH Variation Studies of the NFMS. Extreme changes in pH on the surface of the matrix can cause irritation to mucous membranes within the oral cavity [33]. Measurement of the surface pH is therefore essential. Matrices were allowed to swell in contact with 1 mL of simulated saliva (pH 6.75). The surface pH was measured by glass microelectrode (Mettler Instruments, Giessen, Germany). Measurements were taken after the matrices had been hydrated for 20 seconds and at 1, 3, 5, 10, and 15 minutes thereafter.

2.4.5. Toughness and Biaxial Extensibility Studies of the NFMS. Biaxial extensibility was determined from force-distance profiles generated using a TA.XTplus Texture Analyser (Stable Micro Systems, London, England) fitted with a 2 mm flat cylindrical probe and a 5 kg load cell. The method of testing the extensibility was based on work by Sibeko and coworkers (2009) [34]. The sample was secured onto a ring assembly with a central hole (5 mm diameter), which was attached to a supportive, hollow, raised platform. The setup was placed such that the cylindrical probe of the textural analyzer was centralized over the hole. The probe was lowered and embedded onto the sample according to the test parameters outlined in Table 2.

2.4.6. Mucoadhesion of the Optimized NFMS and Drug-Loaded Films. Mucoadhesion testing was performed on NFMS sections using a TA.XTplus Texture Analyser (Stable Micro Systems, London, England) fitted with a cylindrical probe. Porcine buccal mucosal tissue was attached to the probe, using rubber bands, and exposed to simulated saliva (pH 6.75). The NFMS samples were attached to the stage directly below the probe. Mucoadhesion was tested by measuring the maximum detachment force (MDF) and the work of adhesion (WA) (AUC_{FD}) between the buccal mucosa and the samples. The pretest, test, and posttest speeds were 2, 2, and 10 mm/s, respectively. An applied force of 50 g, a trigger force of 5 g, and contact time of 5 seconds were used for the test.

2.4.7. Tensile Studies of the Optimized NFMS and Drug-Loaded Films. The tensile properties of samples were measured using a nanoTensile 5000 (Hysitron Incorporated, Minneapolis, MN, USA). Samples were cut into thin strips and mounted, with cyanoacrylate-based adhesive, onto specially designed mounting brackets held together with rigid strips of cardboard. Once the sample had cured completely, the width,

length, and thickness were measured with digital calipers. The sample and sample bracket were secured in the upper sample gripper on the nanoTensile (NT) head, and the mass was measured. The NT head was lowered, and the axes were aligned in order to secure the bottom of the sample bracket in the lower sample gripper. The rigid cardboard supports were each cut on the marks in order to prevent the supports from interfering with sample testing. The mounting brackets were moved apart at a constant rate of displacement, and the tensile properties of the sample were measured and recorded.

2.5. Disintegration Time of the Optimized NFMS and Drug-Loaded Films. The *in vitro* disintegration time of NFMS samples and drug-loaded films (FD and FE) was determined according to a modified method based on the United States Pharmacopoeia (USP) method for tablet disintegration testing using a Type PTZ 1 basket-rack assembly disintegration apparatus (Pharma Test, Hainburg, Germany). According to the USP, disintegration is considered to have occurred when there is no longer any solid residue left on the mesh of the basket-rack assembly apparatus (USP 28, 2005). The disintegration medium comprised 150 mL simulated saliva (pH 6.75) placed in a glass jar submerged in a water bath maintained at 37°C. Samples were cut into sections and placed on the mesh of the basket rack assembly, with a mesh disc placed on top. The basket rack assembly was raised and lowered through a distance of 55 mm at a frequency of 25 cycles per minute, and the time taken for sample disintegration to occur was determined by observation and recorded.

2.6. Drug Entrapment of Optimized NFMS and Drug-Loaded Films. Samples of the NFMS and the two drug-loaded films (FD and FE) were cut into 1.5 cm² sections, dissolved in simulated saliva (pH 6.75), and the drug content of each section was analyzed by UV spectrophotometer (NanoPhotometer, Implen GmbH, Munchen, Germany) at ambient temperature (25°C) at lambda max of 260 nm.

2.7. In Vitro Drug Release. Standard USP tests and apparatuses for *in vitro* dissolution and drug release testing require large volumes of fluid, which do not accurately reflect the *in vivo* conditions in the oral cavity, where there is only a small volume of fluid available for the dissolution of a drug delivery system [35]. A modified drug release testing method was therefore developed for the purposes of this study. *In vitro* drug release was tested using a 10 mm long magnet in a 35 mm diameter petri-dish, placed on a temperature-controlled magnetic stirrer. 2 mL of simulated saliva (pH 6.75) was placed in the petri-dish, maintained at 37°C, and stirred at a constant rate to ensure circulation of buffer. NFMS, FD, and FE samples were cut into sections of same dimensions and placed in the buffer. Samples were drawn at 0.083, 0.25, 0.5, 1, 3, 5, 10, and 15 minutes, analyzed by UV spectrophotometer, and replaced by fresh buffer. As a branded product comparison, the *in vitro* dissolution testing of Sleepzeze-PM tablets was performed using a rotating paddle apparatus (Model 7ST, Caleva, Frankfurt, Germany) and employing 900 mL phosphate buffered saline (PBS) (pH 6.8,

37°C). Samples were drawn at 1, 3, 5, 10, 15, 30, 60, and 90 minutes, replaced with fresh buffer, and analyzed by UV spectrophotometer (NanoPhotometer, Implen GmbH, Munchen, Germany).

2.8. Ex Vivo Drug Permeation Studies. *Ex vivo* drug permeation testing was performed using porcine buccal tissue, which is considered to have a closer resemblance to human buccal mucosa than other animal tissues [36]. Porcine buccal mucosal tissue was obtained from a certified local abattoir and transported, on ice, to the laboratory within 1 hour. Excess tissue was removed; specimens were flash-frozen at -40°C with liquid nitrogen and stored at -60°C until required for use. Frozen specimens were equilibrated in phosphate buffered saline (PBS) (pH 7.4) at room temperature to thaw. Sections of mucosa were mounted in Franz Type Diffusion Cells (Perme Gear, Inc., Hellertown, PA, USA) and equilibrated for 0.5 hours at 37°C by adding PBS (pH 7.4) to both the acceptor and donor compartments. After equilibration, the PBS in the donor compartment was removed and was replaced with an NFMS, FD, or FE sample in simulated saliva (pH 6.75). A 2 mg/mL DPH in simulated saliva solution was also tested for comparative purposes. Samples were drawn from the acceptor compartment at 0.33, 1, 2, 3, 5, 10, 15, and 30 minutes and analyzed by UV spectrophotometry, and the removed volume was replaced with fresh PBS. The apparent permeability coefficient (P_{app}) and steady state flux (J_{ss}) values were calculated using (1) and (2), respectively, as follows:

$$P_{app} = \frac{Q}{A \times c \times t}, \quad (1)$$

$$J_{ss} = \frac{\Delta M}{A \times \Delta t}, \quad (2)$$

where Q is the total amount of drug permeated during the testing time (μg), A is the diffusional area (cm^2), c is the initial drug concentration in the donor compartment ($\mu\text{g}/\text{mL}$), t is the total time that the experiment was run for (seconds), and ΔM is the amount of drug that had permeated through the mucosal tissue during time Δt .

2.9. Atomistic Molecular Structural Mechanics Simulations. Molecular mechanics computations in vacuum, which included the model building of the energy-minimized structures of multipolymer complexes, were performed using the HyperChem 8.0.8 Molecular Modeling System (Hypercube Inc., Gainesville, FL, USA) and ChemBio3D Ultra 11.0 (CambridgeSoft Corporation, Cambridge, UK) [37]. The PVA decamer was drawn using ChemBio3D Ultra in its syndiotactic stereochemistry as a 3D model, whereas the structure of HPMC (4 saccharide units) was built from standard bond lengths and angles using sugar builder module on HyperChem 8.0.8. The oligosaccharide length for the polysaccharide chain was determined on the basis of equivalent grid surface area covered by the polysaccharide so that the inherent stereoelectronic factors at the interaction site can be perfectly optimized. The set of low-energy conformers that were in equilibrium with each other was identified and

portrayed as the lowest energy conformational model. The structure of glycosylated mucopeptide analogue (MUC) was generated using sequence editor module on HyperChem 8.0.8. The glycosylation was carried out at the threonine and serine amino acid residues. The structure of glycerol (GLY) was built up with natural bond angles as defined in the Hyperchem software. The models, initially minimized using the MM+ Force Field, were energetically optimized using the AMBER 3 (Assisted Model Building and Energy Refinements) Force Field. The conformer having the lowest energy was used to create the polymer-polymer complexes. A complex of one molecule with another was assembled by disposing them in a parallel way, and the same procedure of energy-minimization was repeated to generate the final models. Full geometry optimizations were carried out in vacuum employing the Polak-Ribiere conjugate gradient method until an RMS gradient of 0.001 kcal/mol was reached. Force field options in the AMBER (with all hydrogen atoms explicitly included) and MM+ (extended to incorporate nonbonded cut-offs and restraints) methods were the HyperChem 8.0.8 defaults. For calculations of energy attributes, the force fields were utilized with a distance-dependent dielectric constant scaled by a factor of 1. The 1–4 scale factors are the following: electrostatic 0.5 and van der Waals 0.5. Invariant factors common to mathematical description of binding energy and substituent characteristics have been ignored [37].

3. Results and Discussion

3.1. Response Optimization. All the NFMS prepared through inclusion of 15 different formulations of polymer backing film were analyzed in terms of disintegration time, work of adhesion (WA), maximum detachment force (MDF), area under the curve (AUC_D) at 1 minute, and area under the curve (AUC_p) at 3 minutes which are graphically represented in Figure 1.

Response optimization was performed using Minitab, V15 (Minitab Inc., PA, USA). The film formulation was optimized according to the measured responses. Maximizing and minimizing responses, where appropriate, resulted in a low desirability for the optimized formulation, and the values were therefore targeted within the limits of acceptability. The final optimization plot revealed a composite desirability of 95.23%. Tables 3 and 4 display the fitted values acquired from formulation optimization with the observed experimental values for the various responses.

For optimized film preparation, polymer solutions were prepared by dissolving 136.5 mg of glycerol, 794 mg of polyvinylalcohol (PVA), and 116 mg of hydroxypropyl-methylcellulose (HPMC) in 79.39 mL of a 4:1 mixture of deionized water and propan-2-ol.

3.2. Physical Dimensions of the Films and Fiber Layer. The films produced were even, thin, transparent, and pliable. The fibers formed a white layer on the films. The NFMS backing layer film was 80 μm thick, while the complete NFMS was 460 μm thick, and hence the fiber layer was 380 μm thick. The

TABLE 3: Targeted responses for constrained optimization of the film formulation.

Response	Lower	Target	Upper
Disintegration time (seconds)	12	13	20
Work of Adhesion (mJ)	0.3	0.4	0.7
Maximum detachment force (N)	0.2	0.3	0.45
AUC_D at 1 minute	0.3	0.35	0.45
AUC_p at 3 minutes	1.6	1.9	2

TABLE 4: Fitted and experimental values for the optimization responses.

Response	Fitted value	Experimental value	Desirability
Disintegration time (seconds)	13.2457	12.8	96.6%
Work of adhesion (mJ)	0.3885	0.335	86.2%
Maximum Detachment force (N)	0.3043	0.2705	88.9%
AUC_D at 1 minute	0.3491	0.4179	83.5%
AUC_p at 3 minutes	1.8885	2.0860	90.5%

FE film was 110 μm thick, and the FD film was approximately 90 μm thick but was somewhat uneven in places.

3.3. Scanning Electron Microscopy. SEM analysis revealed that the fibers produced were randomly arranged having uniform diameters on average. The fiber diameter was approximately 0.36 μm , and the average visible pore size ranged between approximately 0.69 and 1.91 μm , as depicted in Figure 2.

3.4. FTIR Spectroscopy. FTIR analysis was performed in order to determine whether any chemical changes occurred to the drug and/or polymer during the process of electrospinning. The FTIR spectra for the DPH-loaded fiber layer (DF), DPH, and non-drug-loaded PVA placebo fibers (PF) are depicted in Figure 3. The broad O–H stretching vibration of PVA can clearly be seen for both DF and PF at 3295 cm^{-1} . DPH and DF both show a small peak at 3033 cm^{-1} , characteristic of the phenyl groups present in the DPH molecule (Figure 3). The phenyl groups are also identified by the presence of large peaks at 755 cm^{-1} and 702 cm^{-1} in both profiles where DPH was present. The peak associated with the stretching vibration of the alkoxy substituent in the DPH molecule at 2955 cm^{-1} is obscured by the slightly broader band of the alkyl group of the PVA molecule at 2913 cm^{-1} in the DF spectrum, which can also be seen in the PF spectrum. The broad peaks at 2594 cm^{-1} , 2524 cm^{-1} , and 2487 cm^{-1} in the DPH spectrum, representative of the tertiary amine group, are also visible in the DF spectrum, but not in the PF spectrum. The peak at 1598 cm^{-1} , indicating the absorption from the phenyl groups, is visible in both the DPH and DF spectra. From the FTIR data, it can therefore be deduced that no significant chemical changes occurred to the drug during solution preparation and electrospinning.

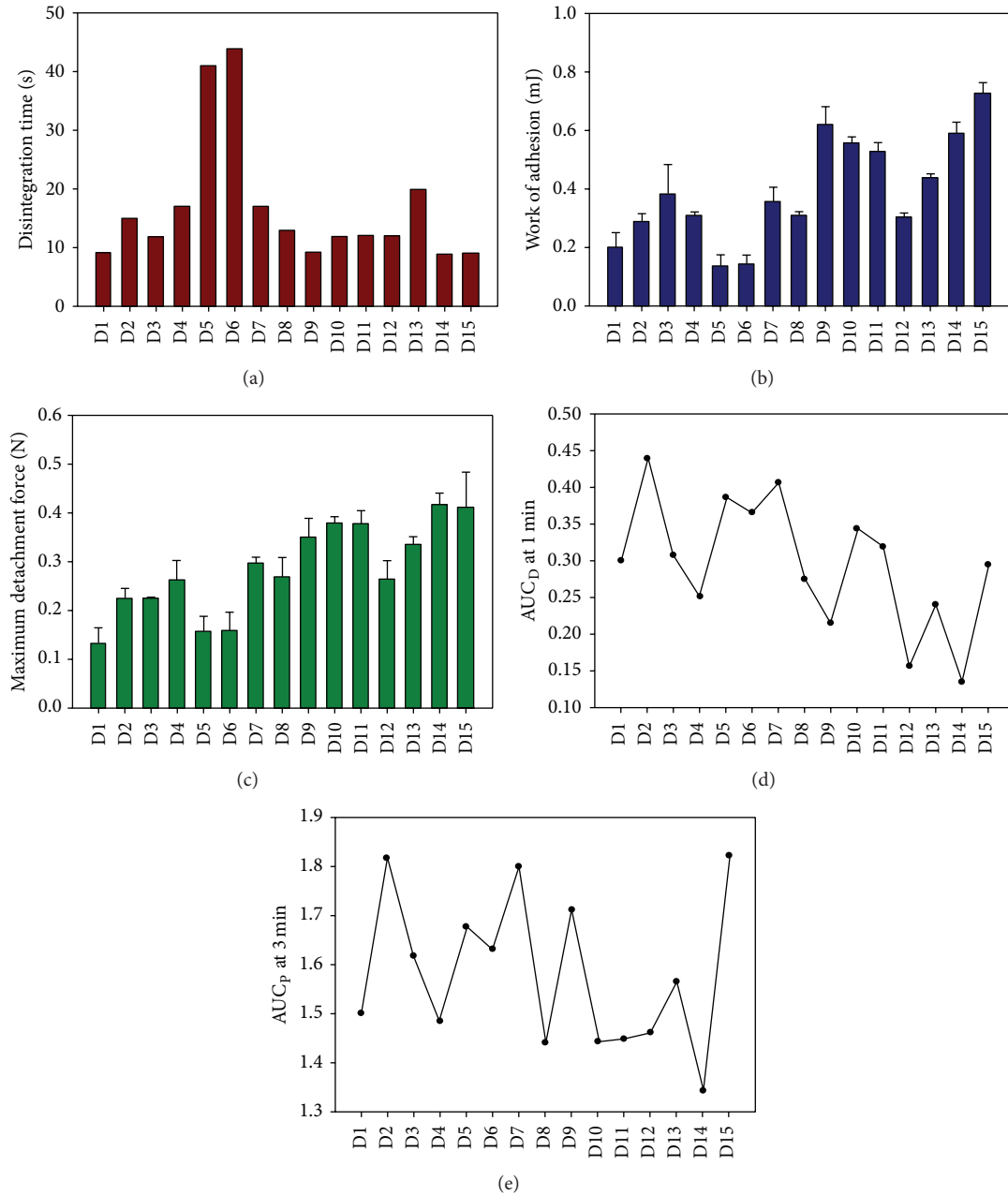


FIGURE 1: The 15 experimental design formulations depicting (a) average disintegration times, (b) average work of adhesion (WA), (c) average maximum detachment force (MDF), (d) AUC_D at 1 minute, and (e) AUC_p at 3 minutes.

3.5. Rheological Studies of the Components of the NFMS

3.5.1. Formulations. The rheological properties of a hydrated sample play an important role in the retention of that sample within the buccal cavity. The hydrated film and NFMS samples were investigated for the effect of an increasing shear rate ($\dot{\gamma}$) on shear force (τ) and viscosity (η). The average values over the shear rate range for these parameters are outlined in Table 5. Linear rheological profiles are depicted in Figure 4. The FE film (Figure 4(c)) exhibited an exceedingly larger average viscosity and shear force than the NFMS (Figure 4(a)) and FD film (Figure 4(b)), which correlates with the greater mucoadhesive properties and slower disintegration rate

evinced by this film. However, such a high viscosity may result in an unpleasant mouthfeel *in vivo* [38]. The large disparity between the parameters of the NFMS and FE film may be due to the more rapid disintegration rate of the former. Nevertheless, the rheological properties of the NFMS suggest that it would have an adequate retention time, which is in agreement with the mucoadhesion data reported in a later section.

3.5.2. Electrospinning Solution. The rheological properties of a solution employed for electrospinning can have a substantial effect on the process of electrospinning as well as the

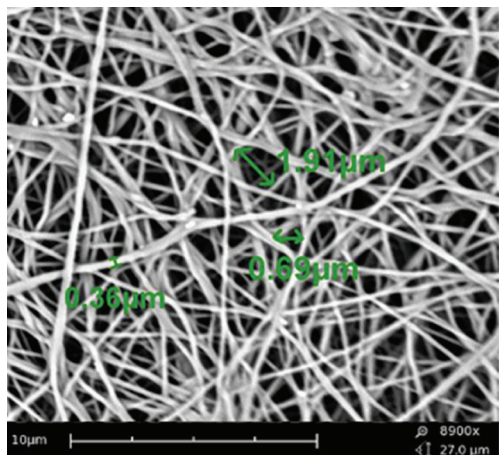


FIGURE 2: SEM image of the electrospun fiber layer, showing average fiber diameter of $0.36 \mu\text{m}$ and visible pore size of between 0.69 and $1.91 \mu\text{m}$.

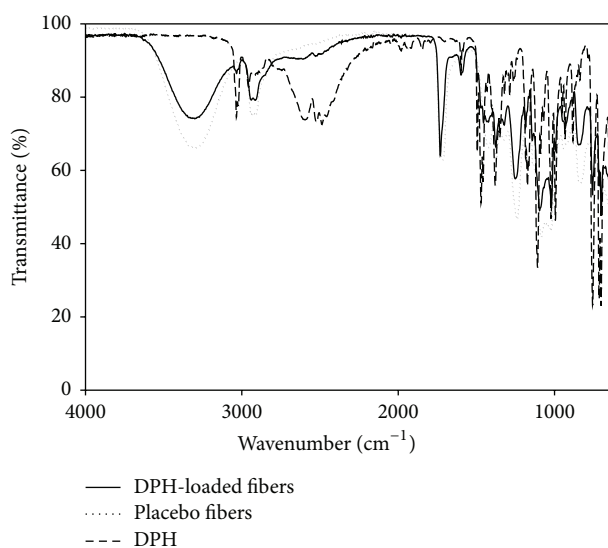


FIGURE 3: FTIR profiles of the drug-loaded fibers (DF), placebo fibers (PF), and DPH.

TABLE 5: Average rheological parameters of the NFMS, FD film, and FE film in 1 mL simulated saliva (pH 6.75).

Sample	Shear rate (1/s)	Shear force (Pa)	Viscosity (mPa·s)
NFMS	254.3	7.44	32.29
FD	252.3	7.39	30.49
FE	253.2	82.71	1616.67

quality and morphology of fibers that are formed. The degree of polymer chain entanglements, and hence the polymer concentration, has a considerable influence over the viscosity of a solution. The actual conformation of individual polymer chains also has a significant influence on solution viscosity, considering that solutions containing coiled chains have a lower viscosity than those with extended chains [39]. It is therefore important to investigate the rheological properties

of polymeric solutions employed in electrospinning. The 25% w/v PVA solution that was electrospun to form the fiber layer of the NFMS was analyzed for responses to rheological stresses, both linear and oscillating. The average shear force (τ) and viscosity (η) were 186.40 Pa and 737.5 mPa·s, respectively, for an average shear rate ($\dot{\gamma}$) of 252.3/s. Figure 5 displays the rheological profile. The linear rheological properties of the 25% w/v solution were deemed acceptable for electrospinning because adequate fiber formation occurred at that polymer concentration.

Thixotropy is observed when the viscosity of a material, that was at rest, decreases on exposure to a mechanical stress and consequently increases again upon removal of the stress. The thixotropy of the 25% w/v PVA electrospinning solution was determined by calculating the difference between the AUC values of the increasing shear and decreasing shear rate curves and was determined to be $-1.229 \text{ Pa}\cdot\text{s}^{-1}$. This difference is relatively small when compared to the average AUC, which was $757.4 \text{ Pa}\cdot\text{s}^{-1}$, and it was deduced that the electrospinning solution underwent adequate thixotropic recovery. Figure 5(b) displays the thixotropy curve for the 25% PVA solution. The curves of shear stress as a function of shear rate (blue line) for both increasing and decreasing rates follow an almost identical path and appear as one thick line, suggesting a favorable recovery of the sample.

Viscoelasticity is an important factor to be considered for the electrospinning of a polymer solution as the polymer is required to be stretched in order to produce fibers. It is necessary for the elastic properties of a solution to be great enough so that the fiber jet will not break up before reaching the collector surface. Oscillation rheology testing is a useful tool for assessing the viscoelastic behavior of materials intended for electrospinning. The yield stress (τ_0) was determined for the 25% w/v PVA electrospinning solution at 25°C by measuring the deformation (γ) over a range of controlled stress (τ). The average yield stress was 0.3782 Pa and the rheological plot is depicted in Figure 5(c). In order to determine the viscoelastic region of the 25% w/v PVA electrospinning solution, a stress sweep was performed at various frequencies to ascertain the yield point. The yield point was found to be 6.36 Pa at a frequency of 0.1 Hz. A frequency sweep was performed in order to determine the stability of the 25% w/v PVA solution. The frequency of oscillations ranged from 8 to 0.008 Hz at a constant stress. The resulting plot is presented in Figure 5(d).

3.6. Microenvironmental Surface pH Variation of the NFMS. It has been observed that extreme changes in surface pH may cause damage to mucosal surfaces [40]. The evaluation of surface pH variation is therefore an important factor to consider for oramucosal drug delivery system. The surface pH values of NFMS ranged between 6.63 and 6.75 over the 15 minutes in which measurements were taken (Figure 6). There was an initial drop in pH to 6.63 at the 20 second time point, possibly due to dissolution and subsequent solubilization of citric acid, which was employed in the formulation as a taste-masking component. At the 3 minute time point, the pH had

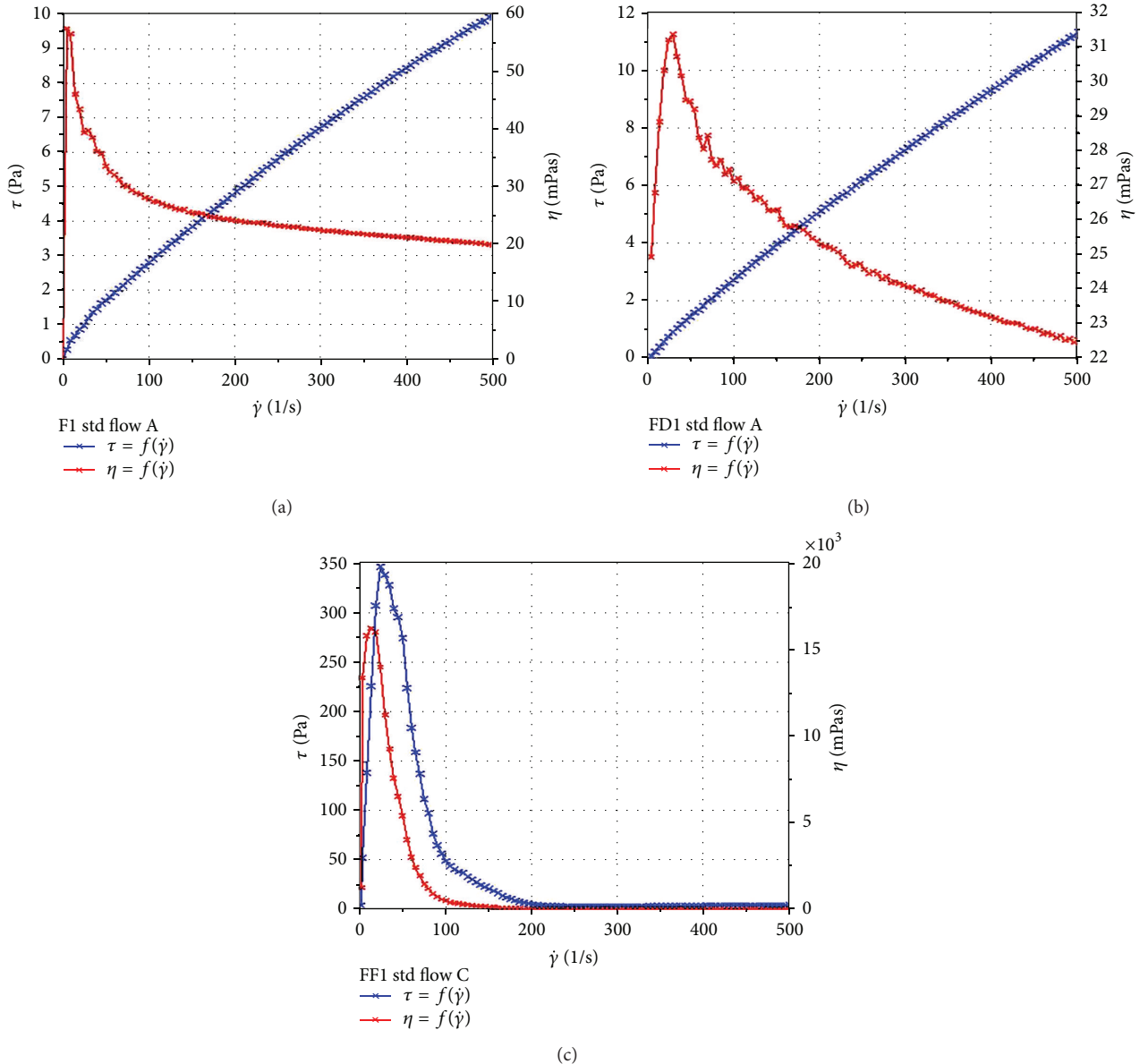


FIGURE 4: Linear rheological profiles of the (a) NFMS, (b) FD film, and (c) FE film.

increased to 6.73, which may be due to the buffering effect of the simulated saliva or the dissolving of the polymeric components of the formulation. The variation of pH was less than 0.5 units and was considered acceptable for an oramucosally administered drug delivery system as it can be deduced that minimal irritation to the buccal mucosa would occur.

3.7. Toughness and Biaxial Extensibility Studies of the NFMS. Extensibility is the degree of extension or stretching that a material can withstand before fracture occurs; polymer linkages have a substantial effect on the physico-mechanical strength of materials. The maximum force (F_{\max}) and distance (D_{\max}) values for the NFMS, optimized polymer backing film of the NFMS (NFMS film), FD film, and FE film were plotted and are presented in Figure 7. The complete

NFMS was found to be slightly stronger than the NFMS film ($F_{\max} = 5.29$ N and 5.17 N, resp.), but also less extensible ($D_{\max} = 4.435$ and 4.957 mm, resp.). It can therefore be deduced that the presence of electrospun fibers resulted in a slight increase in film strength and a decrease in extensibility. When electrospun fibers are produced, there is a thinning and extending process that takes place, and this may result in the fibers being less extensible than the film. The presence of drug in the polymer backing film (FD) brought about a decrease in both F_{\max} and D_{\max} . This may also partially explain the reduction in extensibility with the presence of a drug-loaded fiber layer. The FE film had a significantly larger F_{\max} and D_{\max} than the NFMS, which may be due to the absence of the more rigid polymer, HPMC, and formation by film casting, which does not result in thinning, of the former.

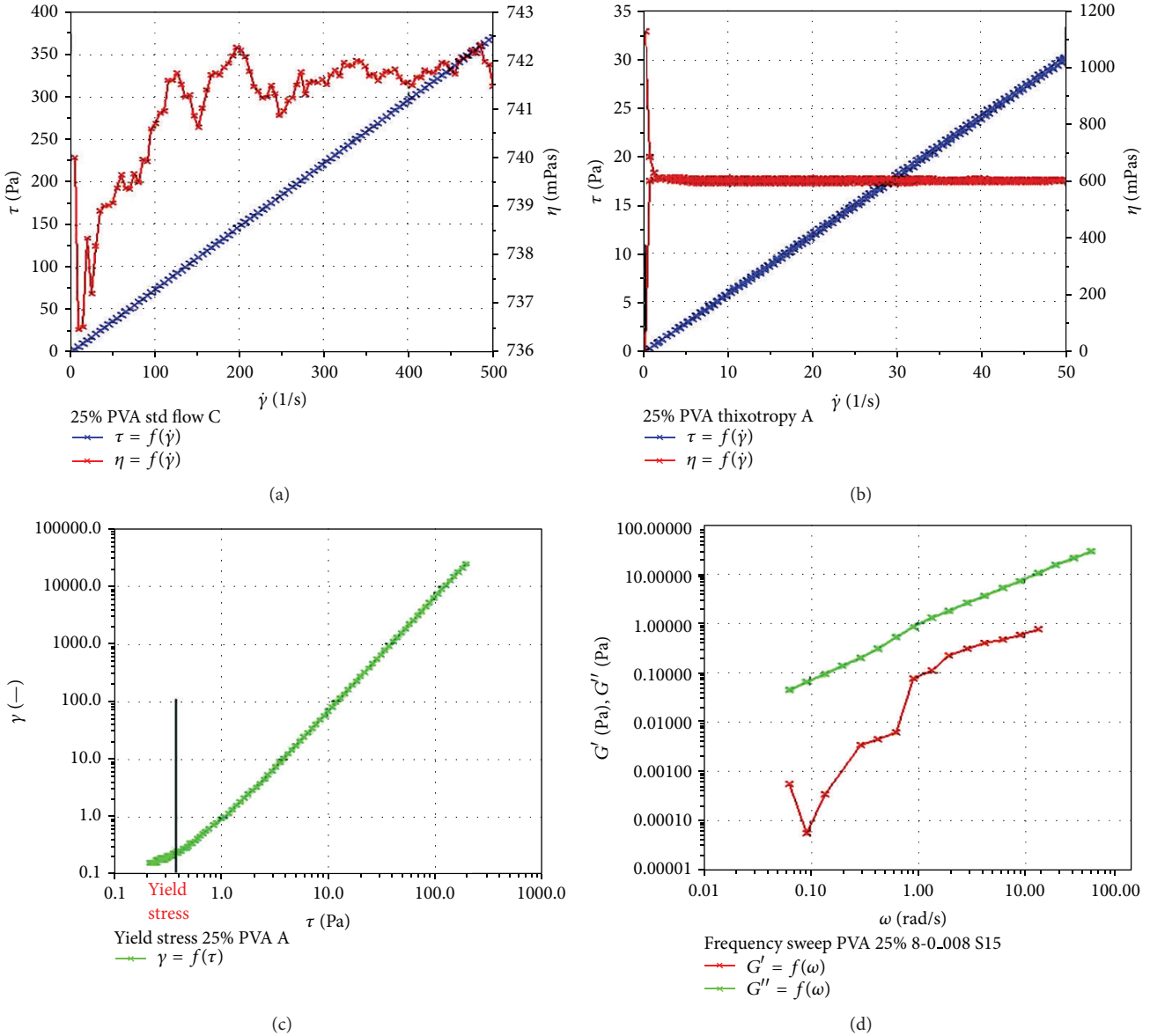


FIGURE 5: (a) Linear rheological profile of 25% w/v PVA electrospinning solution, (b) thixotropy curve for the 25% w/v PVA solution used for electrospinning, (c) rheology plot depicting the yield stress (at 0.3782 Pa) of a 25% w/v PVA solution intended for electrospinning, and (d) stress sweep of 25% w/v PVA solution intended for electrospinning.

TABLE 6: Experimental values obtained from nanotensile analysis.

Sample	Young's modulus (MPa)	Yield stress (MPa)	Ultimate strength (MPa)	Ultimate strain	Toughness (J/cm ³)
Fiber layer	26.09	0.49	2.98	0.227	0.38
NFMS film	36.01	1.675	3.33	0.242	0.62
NFMS	30.31	1.18	2.79	0.238	0.48
FD	56.35	1.13	2.73	0.314	0.71
FE	20.34	1.10	3.52	0.731	2.10

3.8. *Tensile Properties by Nanotensile Testing.* The stress-strain relationship of a material is highly dependent on the flexibility of the polymer chains and the strength of the material. When only a small amount of stress is required to produce a large amount of strain, the material is considered to be flexible, and Young's modulus, which is the slope of the linear portion of the stress-strain curve, will be relatively small. The average experimental values for Young's modulus (E), yield stress (σ_y), ultimate strength (σ_u), ultimate strain (ϵ_u), and toughness (u_f) are outlined in Table 6. The samples tested were the fiber layer of the NFMS (Figure 8(a)), the NFMS film (Figure 8(b)), the complete NFMS (Figure 8(c)), the FD film (Figure 8(d)), and the FE film (Figure 8(e)). The drug-loaded fiber layer exhibited the smallest yield stress, ultimate strain,

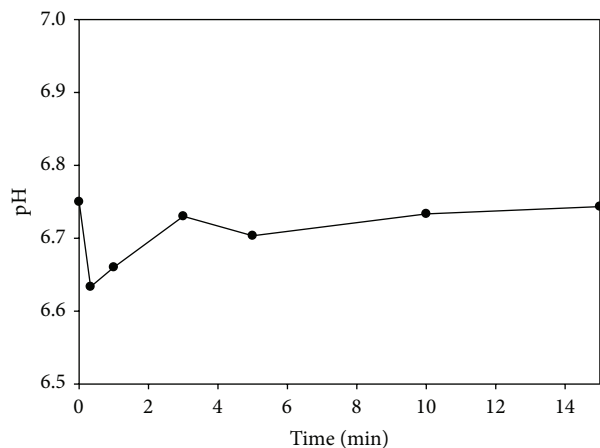


FIGURE 6: Average pH variation over time for the NFMS hydrated in simulated saliva (pH 6.75) ($n = 3$, $SD < 0.01$).

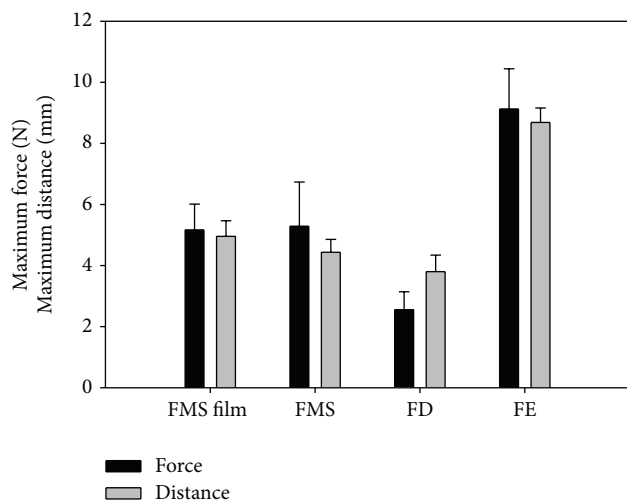


FIGURE 7: Vertical bar chart outlining average maximum force and distance values for the film of the nanofibrous matrix system (NFMS), the complete NFMS, drug-loaded NFMS film (FD) and comparator film containing the same components as the electrospinning solution (FE).

and toughness (Figure 8(a)). Young's modulus of the fiber layer was greater than that of the FE film (Figure 8(e)) but smaller than the other tested samples, suggesting that it was more flexible than the film onto which it was incorporated but less flexible than the FE film. When compared to the FE film, which was prepared using the same components at the same ratios, the fiber layer was found to have a larger Young's modulus and a considerably smaller yield stress, ultimate strength, ultimate strain, and toughness, as well as a smaller elastic region (green portion of nanotensile profile), which may be attributed to the elongating forces experienced by polymer chains during electrospinning [21, 41]. When a polymer is exposed to greater elongating forces, the fibers that are formed will have smaller diameters, which have also been associated with a larger Young's modulus and hence a greater stiffness. It can therefore be deduced that the differences between the tensile properties of the fiber layer and the

FE film are due to polymer chain stretching during fiber formation. The NFMS film revealed slightly larger values than the fiber layer for the various responses determined during nanotensile testing (Figure 8(b)). This may be due to the presence of the more rigid polymer, HPMC, in the film. The profile for the NFMS revealed two distinct points of fracture—the first one being the point at which the fiber layer fractured and the second where the film layer fractured (Figure 8(c)). The FD film (Figure 8(d)), which is the DPH-loaded NFMS film, featured a substantially larger Young's modulus than the NFMS film, suggesting that the presence of DPH in the formulation enhanced the rigidity of the film.

The results of nanotensile testing were in agreement with the extensibility results in the previous section. However, the two tests were performed disparately and with varying sensitivity. The extensibility test utilized a large sample area, imbedded a probe into the sample until fracture, and measured the force-distance relationship, whereas the nanotensile test employed only a small sample area, pulled the sample apart until fracture, and measured the stress-strain relationship, from which various parameters, such as Young's modulus, yield stress, and toughness, could be calculated. While both tests are useful, the nanotensile test was more applicable for this particular formulation due to the method of testing, type of results produced, and the augmented sensitivity of the test.

3.9. Mucoadhesive Properties. The average maximum detachment force (MDF) and work of adhesion (WA) were determined from the peak and AUC, respectively, of the force-distance profiles generated by mucoadhesive testing. Table 7 outlines the values of MDF and WA for the NFMS film, nanofibrous layer, and the drug-loaded films (FD and FE). The backing film of the NFMS exhibited an adequate MDF and WA. The nanofibrous layer was observed to be somewhat more mucoadhesive than the film; however, due to the rapid disintegration rate of the fibers, the backing film is required to hold the system in place and ensure that the released drug is detained at the buccal mucosa until absorption occurs. The FE film was found to have a considerably larger MDF than the nanofibrous layer of the NFMS. This may be attributed to the rapid disintegration rate of the fibers, resulting in less of the formulation being available in its original form at the point in time when mucoadhesion was measured, as opposed to the slower disintegration rate of the FE film. In comparison to the NFMS film layer, the FD film displayed an exceedingly smaller MDF and WA. From this, it can be deduced that the addition of drug to the film formulation resulted in a reduction in mucoadhesiveness. The disparity between the MDF and WA values of the NFMS backing film and the FE film may be due to the presence of HPMC in the NFMS film formulation. HPMC has poorly flexible chains due to a high glass transition temperature and is therefore poorly mucoadhesive [42], and hence the addition of HPMC to the film formulation will decrease the mucoadhesive strength of the resulting film.

3.10. Disintegration Time of the Optimized NFMS and Drug-Loaded Films. The time taken for the NFMS and the FD and FE films to disintegrate was 12.8 seconds, 15.8 seconds,

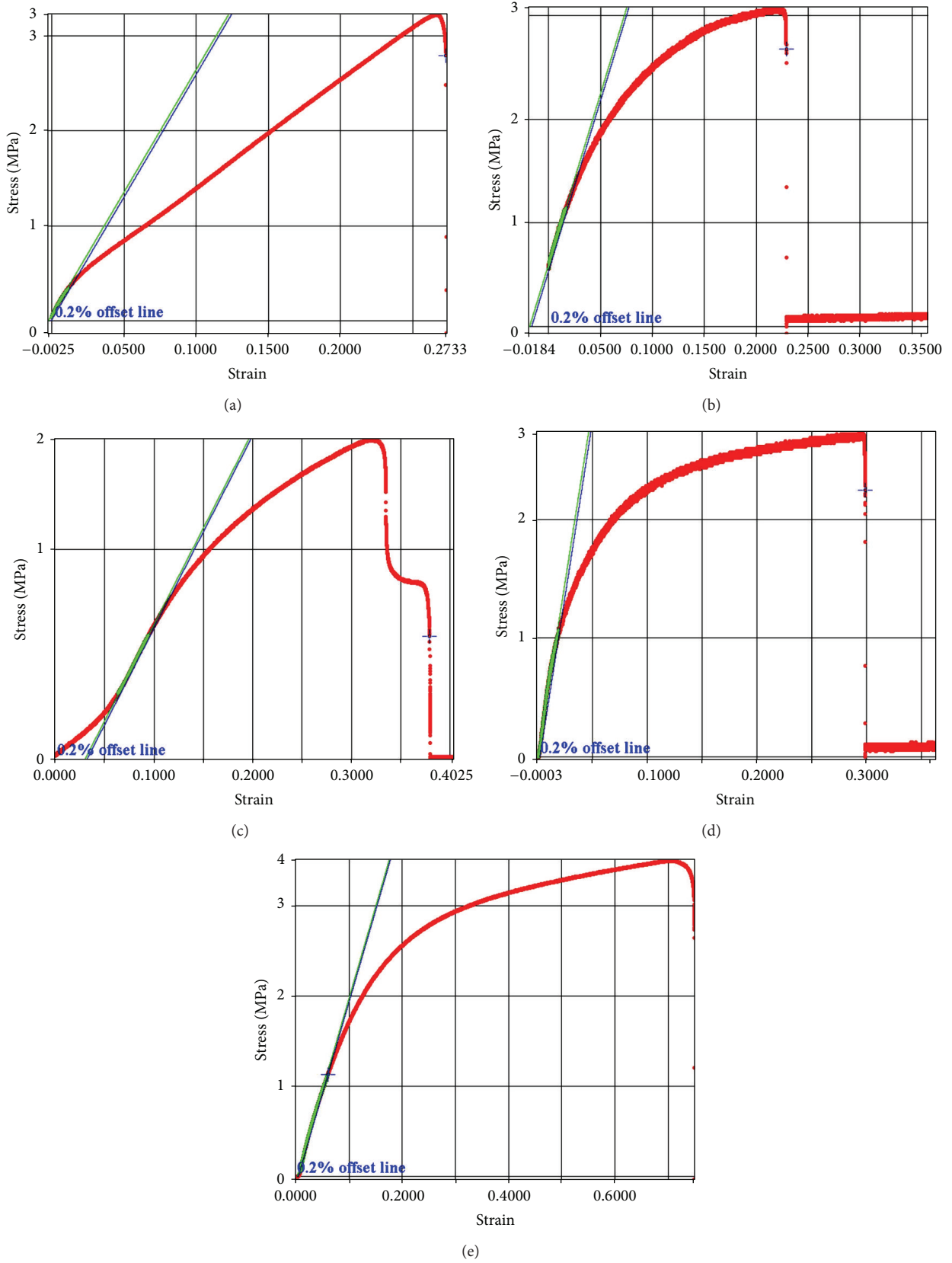


FIGURE 8: Stress-strain nanotensile profiles of the (a) drug-loaded fiber layer of NFMS, (b) film of NFMS, (c) complete NFMS, (d) FD film (drug-loaded), and (e) FE film (drug-loaded).

TABLE 7: MDF and WA for the matrix and different films under study.

Formulation	MDF	WA
NFMS film	0.2705	0.335
NFMS nanofibrous layer	0.2982	0.601
FD	0.0468	0.041
FE	0.3867	0.599

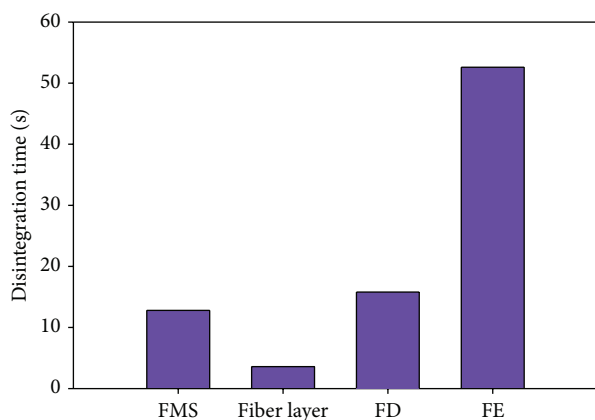


FIGURE 9: Disintegration times of the nanofibrous matrix system (NFMS), fiber layer of the NFMS, drug-loaded optimized film (FD), and film formed from the same components as the electrospinning solution (FE) ($n = 3$, $SD < 1$).

and 52.6 seconds, respectively, and is depicted graphically in Figure 9. The DPH-loaded fiber layer of the NFMS took an average of 3.6 seconds to disintegrate, which is considerably shorter than the time taken for the drug-loaded films or the NFMS to disintegrate. This very short time period of disintegration may not suffice or correlate with the optimum time required for the absorption of the released drug through oramucosa and may result in poor bioavailability of the drug due to swallowing of major drug content. In order to keep the drug at the surface of absorption and prevent swallowing, the backing film layer in NFMS should remain intact for a longer period of time than the fiber layer. However, if the film remains intact for too long, it may result in poor mouthfeel and affect patient acceptability. The polymer backing film supports the fiber layer and retains it for an optimum extended period of time, as seen in Figure 9, ensuring maximum drug absorption without compromising the patient compliance.

3.11. Drug Entrapment and In Vitro Drug Release. The average drug entrapment of the NFMS, FD, and FE films was determined as $2.3 \text{ mg} \pm 0.44 \text{ mg}$, $8.8 \text{ mg} \pm 0.11 \text{ mg}$, and $5.5 \text{ mg} \pm 0.48 \text{ mg}$, respectively. The optimized NFMS exhibited a rapid dissolution rate, with an average of 63% of the loaded dose releasing in 1 minute and 86% in 3 minutes. In comparison, the FD and FE films released 27% and 17% of the loaded dose in 1 minute and 48% and 46% at 3 minutes, respectively. The drug release profiles are depicted in Figure 10(a). It is apparent that the dissolution rate of the NFMS is

significantly more rapid than that of either of the drug-loaded films, owing to the extremely high surface area of the nanofibrous layer in comparison with films [8, 10], which enhances the rate of disintegration and dissolution [14]. Figure 10(b) compares the drug release profiles of the NFMS and the branded comparator product, Sleepeze-PM, the later displaying a relatively rapid drug release, with 31% and 55% of the loaded dose releasing after 1 and 3 minutes, respectively. However, the optimized NFMS exhibited a superior drug release profile in a considerably smaller volume of buffer, which makes it preferable to the conventional system on the market in terms of its rapid action.

The area under the curve (AUC_D) at 1 minute was calculated for the NFMS, FD, and FE films and Sleepeze-PM tablets, and it is illustrated in Figure 10(c). The AUC_D of the NFMS is nearly 3 times greater than that of the FD film and Sleepeze-PM tablets and approximately 5 times greater than the AUC_D of the FE film. Hence it can be deduced that drug release from the NFMS occurs more rapidly than from any of the tested comparison formulations.

3.12. Ex Vivo Drug Permeation Studies. *Ex vivo* drug permeation, where conditions are as similar as possible to *in vivo* circumstances, is a valuable study to conduct in order to determine the expediency of employing a particular drug or drug delivery system for buccal administration [43]. Figure 11(a) depicts the flux profiles of the NFMS, a 2 mg/mL DPH solution, and the drug-loaded films, FD and FE. The DPH solution exhibited a slightly greater flux than the NFMS, with 79% and 78% of the loaded dose permeated at 3 minutes, respectively. The FD and FE films displayed a lower flux than the NFMS, where 74% and 55% of the loaded dose had permeated after 3 minutes, respectively. This is in agreement with the *in vitro* dissolution data. Permeation AUC (AUC_P) at 3 minutes was calculated for the tested formulations and plotted as in Figure 11(b). AUC_P of the 2 mg/mL DPH solution was slightly greater than that for the NFMS, suggesting that the rate of permeation of drug from solution was only marginally faster than that from the NFMS. The FE film exhibited the smallest AUC_P value, and the value for the FD film was between that of the NFMS and FE film. The rate of drug permeation from the DPH-loaded films was somewhat slower than that from the NFMS or the drug solution.

The apparent permeability coefficient (P_{app}) and steady state flux (J_{ss}) values were calculated for the tested formulations and are outlined in Table 8. These values were in accordance with those for AUC_P of the various formulations, with the FE film exhibiting the smallest P_{app} and J_{ss} values and the DPH solution having the largest P_{app} and J_{ss} values.

3.13. Molecular Mechanics Assisted Model Building and Energy Refinements. Molecular mechanics energy relationship (MMER), a method for analytico-mathematical representation of potential energy surfaces, was used to provide information about the contributions of valence terms, non-covalent Coulombic terms, and noncovalent van der Waals

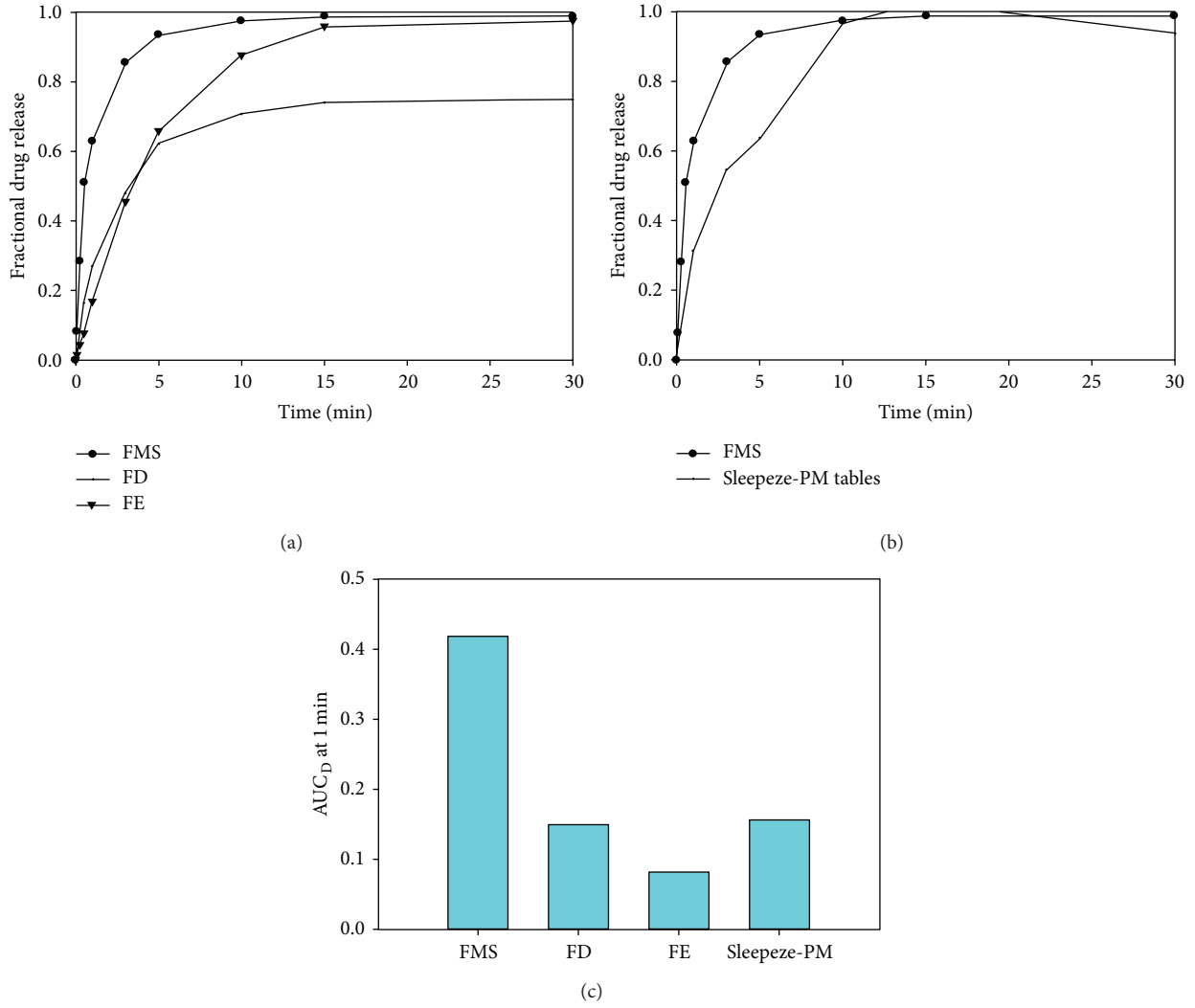


FIGURE 10: (a) Drug release profiles of the nanofibrous matrix system (NFMS) and the drug-loaded films FD and FE ($n = 3$, $SD < 0.04$). (b) Comparative drug release profiles of the nanofibrous matrix system (NFMS) and Sleepeze-PM tablets ($n = 3$, $SD < 0.04$) and (c) AUC_D comparison between the NFMS, comparator DPH-loaded film formulations (FD and FE), and Sleepeze-PM tablets ($n = 3$, $SD < 0.02$).

interactions for the plasticizer/polysaccharide/protein morphologies and interactions. The MMER model for the potential/steric energy factors in various molecular complexes can be written as

$$E_{\text{molecule/complex}} = V_{\Sigma} = V_b + V_{\theta} + V_{\varphi} + V_{ij} + V_{hb} + V_{el}, \quad (3)$$

$$E_{\text{HPMC}} = 49.713V_{\Sigma} = 2.089V_b + 18.821 + 22.360V_{\varphi} + 6.776V_{ij} - 0.335V_{hb}, \quad (4)$$

$$E_{\text{PVA}} = 5.173V_{\Sigma} = 0.615V_b + 1.652V_{\theta} + 0.881V_{\varphi} + 4.895V_{ij} - 2.871V_{hb}, \quad (5)$$

$$E_{\text{HPMC/PVA}} = 44.321V_{\Sigma} = 2.582V_b + 19.911V_{\theta} + 27.276V_{\varphi} - 2.740V_{ij} - 2.709V_{hb}, \quad (6)$$

$[\Delta E = -10.565 \text{ kcal/mol}],$

$$E_{\text{GLY}} = 2.624V_{\Sigma} = 0.096V_b + 1.121V_{\theta} + 0.375V_{\varphi} + 1.031V_{ij}, \quad (7)$$

$$E_{\text{HPMC/GLY}} = 31.891V_{\Sigma} = 2.261V_b + 21.937V_{\theta} + 27.007V_{\varphi} - 19.097V_{ij} - 0.217V_{hb}, \quad (8)$$

$[\Delta E = -28.318 \text{ kcal/mol}],$

$$E_{\text{HPMC/PVA/GLY}} = 22.867V_{\Sigma} = 2.689V_b + 21.701V_{\theta} + 30.849V_{\varphi} - 30.181V_{ij} - 2.192V_{hb}, \quad (9)$$

$[\Delta E = -42.515 \text{ kcal/mol}],$

$$E_{\text{MUC}} = -166.812V_{\Sigma} = 5.474V_b + 70.351V_{\theta} + 55.173V_{\varphi} - 29.066V_{ij} - 7.096V_{hb} - 261.649V_{el}, \quad (10)$$

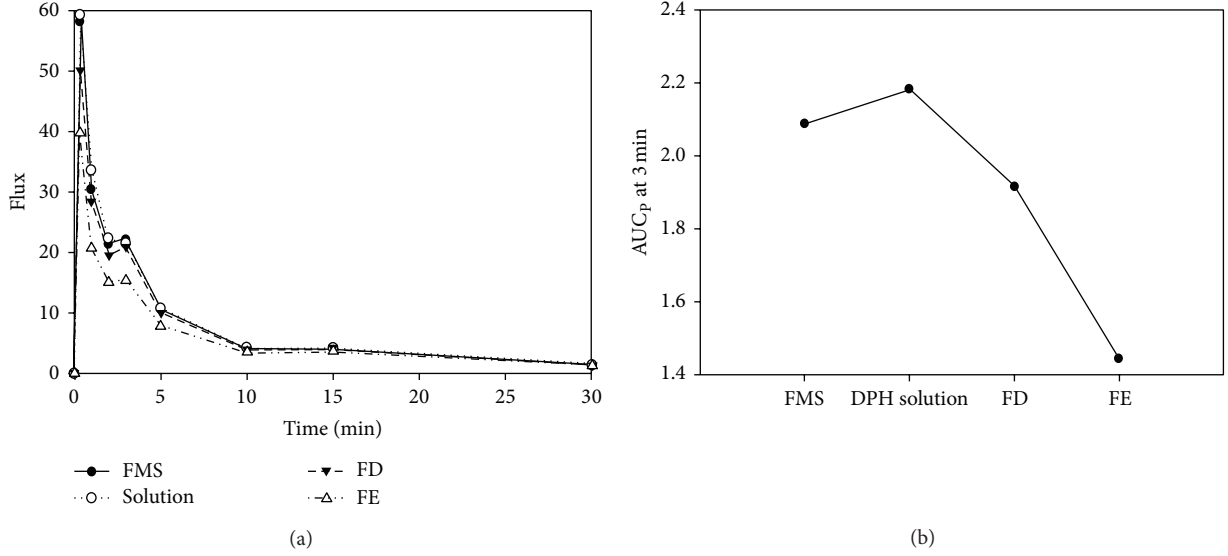


FIGURE 11: (a) Drug permeation profiles of the matrix system (NFMS), the drug solution, and the drug-loaded film formulation (FD and FE) ($n = 3$, $SD < 0.1$ in all cases) and (b) plot depicting AUC_p at 3 minutes for the nanofibrous matrix system (NFMS), DPH solution, and DPH-loaded film formulation (FD and FE) ($n = 3$, $SD < 0.02$ in all cases).

$$\begin{aligned}
 E_{\text{HPMC/MUC}} = & -156.127V_{\Sigma} = 6.888V_b + 88.277V_{\theta} \\
 & + 84.268V_{\varphi} - 51.281V_{ij} - 7.555V_{hb} \\
 & - 276.724V_{el}, \quad [\Delta E = -39.028 \text{ kcal/mol}], \quad (11)
 \end{aligned}$$

$$\begin{aligned}
 E_{\text{PVA/MUC}} = & -175.667V_{\Sigma} = 6.486V_b + 72.435V_{\theta} + 66.468V_{\varphi} \\
 & - 48.050V_{ij} - 9.266V_{hb} - 263.742V_{el}, \\
 & [\Delta E = -14.028 \text{ kcal/mol}], \quad (12)
 \end{aligned}$$

$$\begin{aligned}
 E_{\text{HPMC/PVA/MUC}} = & -170.567V_{\Sigma} = 8.098V_b + 91.792V_{\theta} \\
 & + 78.881V_{\varphi} - 63.968V_{ij} \\
 & - 9.755V_{hb} - 275.615V_{el}, \\
 & [\Delta E = -58.641 \text{ kcal/mol}], \quad (13)
 \end{aligned}$$

where V_{Σ} is related to total steric energy for an optimized structure, V_b corresponds to bond stretching contributions (reference values were assigned to all of structure's bond lengths), V_{θ} denotes bond angle contributions (reference values were assigned to all of structure's bond angles), V_{φ} represents torsional contribution arising from deviations from optimum dihedral angles, V_{ij} incorporates van der Waals interactions due to nonbonded interatomic distances, V_{hb} symbolizes hydrogen-bond energy function and V_{el} stands for electrostatic energy. In addition, the total potential energy deviation, ΔE_{total} , was calculated as the difference between the total potential energy of the complex system and the sum of the potential energies of isolated individual molecules as follows:

$$\Delta E_{\text{Total (A/B)}} = E_{\text{Total (A/B)}} - (E_{\text{Total (A)}} + E_{\text{Total (B)}}). \quad (14)$$

TABLE 8: Calculated apparent permeability coefficient (P_{app}) and steady state flux (J_{ss}) values for the formulations under study.

Formulation	P_{app}	J_{ss}
NFMS	4.9×10^{-4}	5.88
DPH solution	5.0×10^{-4}	5.95
FD	4.7×10^{-4}	5.60
FE	3.4×10^{-4}	4.11

The molecular stability can then be estimated by comparing the total potential energies of the isolated and complexed systems. If the total potential energy of complex is smaller than the sum of the potential energies of isolated individual molecules in the same conformation, the complexed form is more stable and its formation is favoured [44].

3.13.1. Energy Computations for Polymer/Plasticizer Complexes Using Atomistic Simulations. The molecular conformations obtained from the simulation of HPMC, PVA, and glycerol (GLY) are represented by Figure 12, Table 9, and (4)–(9). The effects of blending PVA with HPMC (HPMC/PVA) and glycerol with HPMC (HPMC/GLY) and blending all three altogether are elucidated herein. It is evident from the energy computations that all the three complexes are well stabilized due to $-ve \Delta E$ ((4)–(9)). HPMC contains interactive oxygen containing groups in the form of $-C-O-C-$ (both in the ring and the methyl side chain) and hydroxyl group for possible association with glycerine molecules. Specifically, the oxofunctionalities of HPMC and the hydroxyl functionality of glycerine may interact with directional orientation acting at adequately short distances (Figure 12(a)), H-bonding, and van der Waals attractive interactions resulting in energy minimization of 28.318 kcal/mol. Similarly, in case of HPMC/PVA, the hydroxyl group of PVA interacted with $-C-O-C-$ moiety

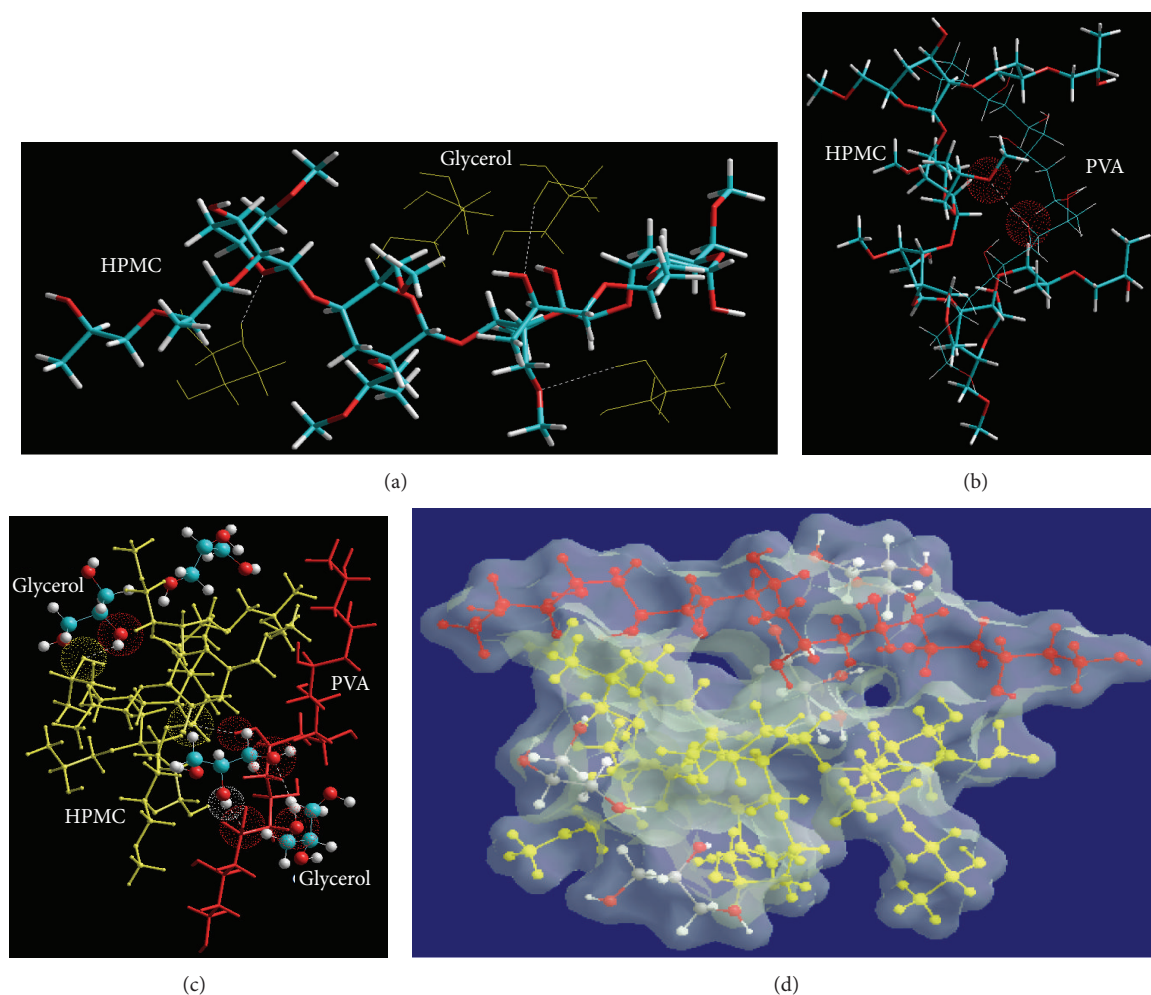


FIGURE 12: Visualization of geometrical preferences of (a) HPMC/glycerol complex, (b) HPMC/PVA complex, and (c) HPMC/PVA/Glycerol complex and (d) connolly molecular electrostatic potential surfaces in translucent display mode showcasing the trimolecular complex after molecular simulation. The atoms involved in H-bonding are emphasized by space filling model (dots). Color codes for elements are C (cyan), O (red), and H (white).

TABLE 9: Molecular mechanics evaluation of the surface-to-volume ratio and density of pure polymers and blends.

Molecular complex	Surface area (\AA^2)	Volume (\AA^3)	SVR [#]	Mass (amu)	Density ($\text{amu}/\text{\AA}^3$)
HPMC	1374.70	2655.35	0.5177	993.15	0.3740
PVA	785.80	1327.24	0.5920	442.55	0.3334
Glycerol	982.04	1333.36	0.7365	368.36	0.2762
HPMC/PVA	1548.78	3476.73	0.4454	1435.69	0.4129
HPMC/GLY	1436.69	3247.83	0.4423	1361.53	0.4192
HPMC/PVA/GLY	1624.86	4052.57	0.4009	1804.07	0.4452

[#]SVR: surface-to-volume ratio.

of HPMC with an energy minimization of 10.565 kcal/mol (Figure 12(b)). Furthermore, we carried out the full simulation of HPMC/PVA/GLY to see whether the individual blend interactions still persist or not. It is evident from Figure 12 that apart from all the previous H-bonding interactions, PVA also interacted with GLY forming a GLY-HPMC-GLY-PVA-GLY complex (Figure 12(c)) resulting in an even higher stabilization of potential energy ($\Delta E = -42.515$ kcal/mol). In all three blend simulations, the nonbonding London dispersion

hydrophobic forces dominated the overall contribution from all the energy terms, further explaining the vigorous geometrical conformational requirements desirable for the networks between these polymer/plasticizer fragments (Figure 12(d)).

In addition, the molecular attributes in terms of surface-to-volume ratio (SVR) and final density corroborated with the above findings with HPMC/PVA/GLY having lowest SVR followed by HPMC/GLY, and HPMC/PVA (Table 9). The lower the surface-to-volume ratio, the more stable

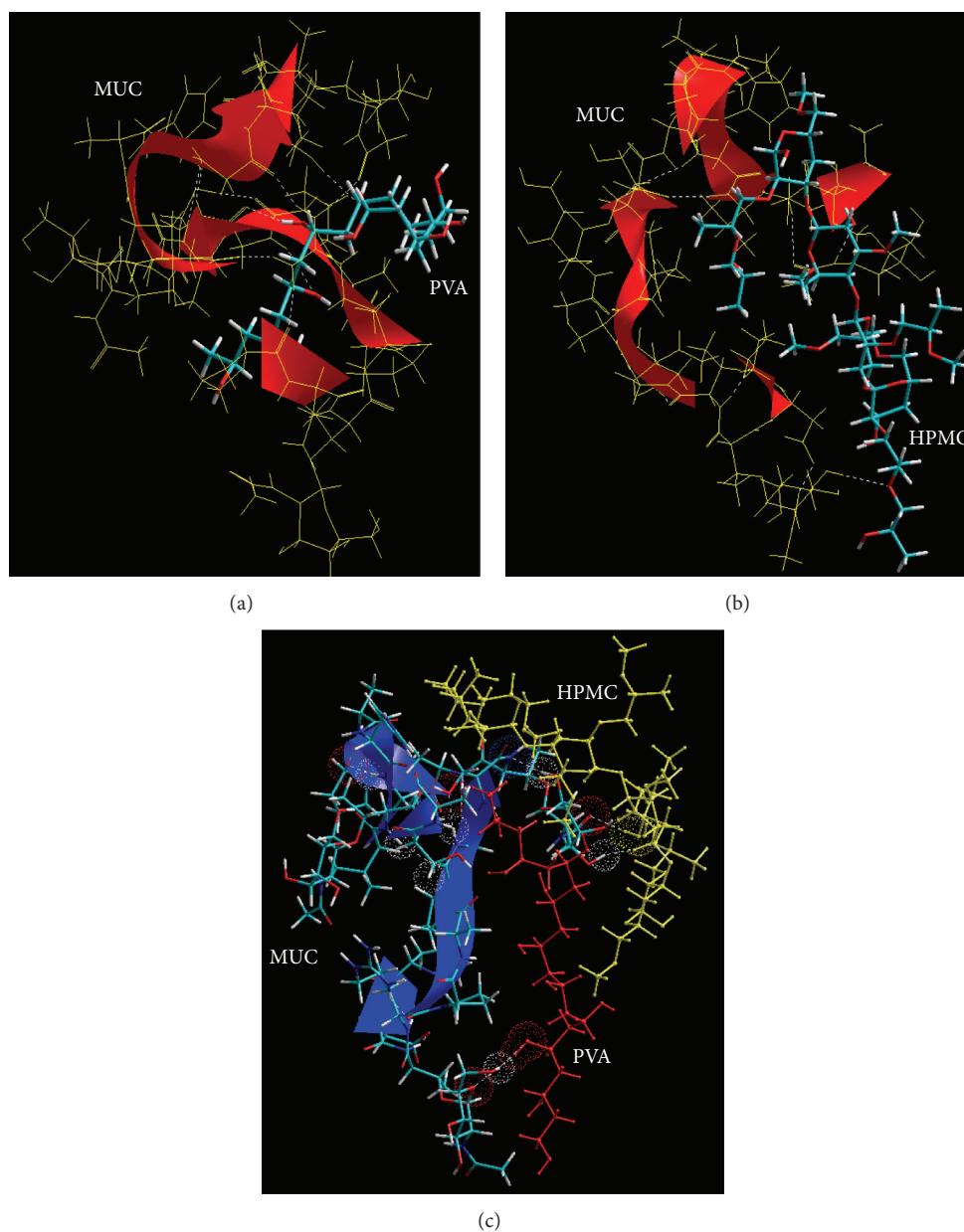


FIGURE 13: Visualization of geometrical preferences of (a) PVA/MUC complex, (b) HPMC/MUC complex, and (c) HPMC/PVA/MUCI complex after molecular simulation. The atoms involved in H-bonding are emphasized by space filling model (dots). Color codes for elements: C (cyan), O (red), N (blue) and H (white).

the structure. In this study, initial models were developed employing a derivative approach based on average-density function of the pure systems. Considering the polymer-polymer/polymer-plasticizer system, a substantial increase in the network density was detected as compared to the average of the component individual molecules, with density values ranging from 0.4129 through 0.4192 to 0.4452 amu/Å³ for HPMC/PVA, HPMC/GLY and HPMC/PVA/GLY, respectively. Interestingly, these density increments are in corroboration with the appearance of specific interchain networking forming a miscible interphase in between the three molecules [45]. Thus we conclude that the energy

stabilization, low SVR, and high density lead to highly efficient plasticization of the HPMC/PVA backing film by glycerol. The observations so obtained were in accordance with previously reported results by Sakellariou et al., 1993 where the plasticizer's efficiency was defined in relation to the tendency of the polymer-plasticizer set to form polar as well as hydrogen-bonding interactions [46].

3.13.2. Prediction of Mucoadhesive Potential of the Backing Layer. The bioadhesive or mucoadhesive potential of the NFMS was determined by measuring the detailed chemical interfaces between the individual polymers (HPMC and

PVA) or polymeric matrix (HPMC/PVA) and the glycosylated oromucopeptide analogue after geometrical optimization using energy minimizations. HPMC and PVA are known to be mucoadhesive polymers and may impart bioadhesion to the drug delivery system [47].

As per the energy consideration, a collective phenomenon comprising van der Waals forces, electrostatic interactions, and H-bonding in the form of nonbonding interactions was reported ((4), (5), and (10)–(13)). This contributed to a stress transduction necessitating the establishment of connectivity between chemically conformed regions via interactive surface generation. Interestingly, the inherent binding energies of the polymer matrices with MUC were quite high ranging from -14.028 through -39.028 to -58.641 kcal/mol in case of PVA/MUC, HMPC/MUC, and HPMC/PVA/MUC confirming the significant interactions among the polymer entities and the oromucopeptide (Figure 13 and Table 9). The minimized energy increased significantly after introducing both the polymers together in the MUC-polymer system leading to a comparatively stabilized conformation. Additionally, the H-bonds formed between the polymer matrix and the MUC were increased in case of trimolecular system (Figure 13). A deeper inspection revealed the existence of hydrophobic interactions in the form of methyl groups (from mucopeptide residues) networking with oxofunctionalities of the constituent polymers (Figure 13).

The experimental mucoadhesion studies can be correlated to these *in silico* findings. As explained earlier in the paper, the mucoadhesion due to hydrophilic polymers is usually accompanied by a “region of maximum” where it is dependent on the concentration of the polymer, such as HPMC in the present case. The contour plot depicted an initial increase in mucoadhesion with increase in the amount of polymers up to the intermediate levels and decreases thereafter. The possible explanation to this is that the HPMC/PVA backing film may readily absorb water while in contact with hydrated mucous membrane leading to swelling of the polymer matrix and may progressively become rubbery because of extensive uncoiling of polymeric chains. Furthermore, this may result in an increase in the mobility of the polymer fragments producing a wide-spread adhesive surface which may thus present with maximum contact area for mucosa to interact and may additionally provide flexibility to the polymer chains for mucosal interpenetration [48]. On contrary, a further increase in the amount of these hydrophilic polymers may render the network structure too dense and less flexible (due to high glass transition temperature as described in mucoadhesion section) to hold the tethered mucous chains thereby decreasing the mucoadhesion [48]. Glycerol may further enhance the mucoadhesion by providing a stabilized and flexible system as postulated in the polymer/plasticizer complexes and also by providing additional hydroxyl bonds to form H-bonds with the mucopeptide.

4. Conclusions

Mucoadhesive, drug-loaded electrospun fibers were incorporated directly onto polymeric backing films of PVA and HPMC which were successfully prepared and optimized

according to a 3-level 3-factor Box-Behnken experimental design. The effects of the independent variables on the dependent response variables were analyzed, and an optimized formulation was mathematically produced. The physicochemical and physicomachanical characteristics of the optimized NFMS were assessed. The FTIR analysis elucidated no significant chemical interactions occurring between drug, polymer, and excipients during the process of formulation preparation. The complete NFMS exhibited rapid and optimum disintegration time. Although the disintegration and drug release of the fiber matrix alone was high enough, the backing film holds the system in place for an optimum time length ensuring the retention of released drug at buccal mucosa until the absorption occurs. The optimized NFMS thus displayed rapid disintegration and drug release with good mucoadhesion, oramucosal retention, flexibility and minimal mucosal irritation due to pH variation. The NFMS may therefore be deemed suitable for rapid oramucosal drug delivery. Furthermore, molecular mechanics technique afforded unique understanding on the miscibility profiling and mucoadhesive properties of specific polymer/plasticizer and polymer/mucopeptide complexes, respectively.

Conflict of Interests

The authors declare that they have no conflict of interests.

Acknowledgments

This research was funded by the National Research Foundation (NRF) and Technology Innovation Agency (TIA) of South Africa.

References

- [1] J. Doshi and D. H. Reneker, “Electrospinning process and applications of electrospun fibers,” *Journal of Electrostatics*, vol. 35, no. 2-3, pp. 151–160, 1995.
- [2] D. Liang, B. S. Hsiao, and B. Chu, “Functional electrospun nanofibrous scaffolds for biomedical applications,” *Advanced Drug Delivery Reviews*, vol. 59, no. 14, pp. 1392–1412, 2007.
- [3] T. J. Sill and H. A. von Recum, “Electrospinning: applications in drug delivery and tissue engineering,” *Biomaterials*, vol. 29, no. 13, pp. 1989–2006, 2008.
- [4] J. M. Deitzel, J. Kleinmeyer, D. Harris, and N. C. B. Tan, “The effect of processing variables on the morphology of electrospun nanofibers and textiles,” *Polymer*, vol. 42, no. 1, pp. 261–272, 2001.
- [5] M. G. McKee, G. L. Wilkes, R. H. Colby, and T. E. Long, “Correlations of solution rheology with electrospun fiber formation of linear and branched polyesters,” *Macromolecules*, vol. 37, no. 5, pp. 1760–1767, 2004.
- [6] S. L. Shenoy, W. D. Bates, H. L. Frisch, and G. E. Wnek, “Role of chain entanglements on fiber formation during electrospinning of polymer solutions: good solvent, non-specific polymer-polymer interaction limit,” *Polymer*, vol. 46, no. 10, pp. 3372–3384, 2005.
- [7] A. Frenot and I. S. Chronakis, “Polymer nanofibers assembled by electrospinning,” *Current Opinion in Colloid and Interface Science*, vol. 8, no. 1-2, pp. 64–75, 2003.

- [8] D. H. Reneker and A. L. Yarin, "Electrospinning jets and polymer nanofibers," *Polymer*, vol. 49, no. 10, pp. 2387–2425, 2008.
- [9] X. Zong, K. Kim, D. Fang, S. Ran, B. S. Hsiao, and B. Chu, "Structure and process relationship of electrospun bioabsorbable nanofiber membranes," *Polymer*, vol. 43, no. 16, pp. 4403–4412, 2002.
- [10] S. Agarwal, J. H. Wendorff, and A. Greiner, "Use of electrospinning technique for biomedical applications," *Polymer*, vol. 49, no. 26, pp. 5603–5621, 2008.
- [11] L. Bruner and St. Tolloczko, "Über die Auflösungs geschwindigkeit fester Körper," *Zeitschrift für Anorganische Chemie*, vol. 28, no. 1, pp. 314–330, 1901.
- [12] E. Sjökvist and C. Nyström, "Physicochemical aspects of drug release. XI. Tableting properties of solid dispersions, using xylitol as carrier material," *International Journal of Pharmaceutics*, vol. 67, no. 2, pp. 139–153, 1991.
- [13] G. Verreck, I. Chun, J. Peeters, J. Rosenblatt, and M. E. Brewster, "Preparation and characterization of nanofibers containing amorphous drug dispersions generated by electrostatic spinning," *Pharmaceutical Research*, vol. 20, no. 5, pp. 810–817, 2003.
- [14] A. Dokoumetzidis and P. Macheras, "A century of dissolution research: from Noyes and Whitney to the biopharmaceutics classification system," *International Journal of Pharmaceutics*, vol. 321, no. 1–2, pp. 1–11, 2006.
- [15] G. Ponchel, "Formulation of oral mucosal drug delivery systems for the systemic delivery of bioactive materials," *Advanced Drug Delivery Reviews*, vol. 13, no. 1–2, pp. 75–87, 1994.
- [16] S. Rossi, G. Sandri, and C. M. Caramella, "Buccal drug delivery: a challenge already won?" *Drug Discovery Today: Technologies*, vol. 2, no. 1, pp. 59–65, 2005.
- [17] M. J. Rathbone, B. K. Drummond, and I. G. Tucker, "The oral cavity as a site for systemic drug delivery," *Advanced Drug Delivery Reviews*, vol. 13, no. 1–2, pp. 1–22, 1994.
- [18] J. Abrams, "New nitrate delivery systems: buccal nitroglycerin," *The American Heart Journal*, vol. 105, no. 5, pp. 848–854, 1983.
- [19] O. A. Scholz, A. Wolff, A. Schumacher et al., "Drug delivery from the oral cavity: focus on a novel mechatronic delivery device," *Drug Discovery Today*, vol. 13, no. 5–6, pp. 247–253, 2008.
- [20] D. M. Simpson, J. Messina, F. Xie, and M. Hale, "Fentanyl buccal tablet for the relief of breakthrough pain in opioid-tolerant adult patients with chronic neuropathic pain: a multicenter, randomized, double-blind, placebo-controlled study," *Clinical Therapeutics*, vol. 29, no. 4, pp. 588–601, 2007.
- [21] A. Baji, Y. W. Mai, S. C. Wong, M. Abtahi, and P. Chen, "Electrospinning of polymer nanofibers: effects on oriented morphology, structures and tensile properties," *Composites Science and Technology*, vol. 70, no. 5, pp. 703–718, 2010.
- [22] E. P. S. Tan and C. T. Lim, "Mechanical characterization of nanofibers—a review," *Composites Science and Technology*, vol. 66, no. 9, pp. 1102–1111, 2006.
- [23] E. P. S. Tan, S. Y. Ng, and C. T. Lim, "Tensile testing of a single ultrafine polymeric fiber," *Biomaterials*, vol. 26, no. 13, pp. 1453–1456, 2005.
- [24] T. Coviello, F. Alhaique, C. Parisi, P. Matricardi, G. Bocchinfuso, and M. Grassi, "A new polysaccharidic gel matrix for drug delivery: preparation and mechanical properties," *Journal of Controlled Release*, vol. 102, no. 3, pp. 643–656, 2005.
- [25] S. N. R. Adhikari, B. S. Nayak, A. K. Nayak, and B. Mohanty, "Formulation and evaluation of buccal patches for delivery of atenolol," *AAPS PharmSciTech*, vol. 11, no. 3, pp. 1038–1044, 2010.
- [26] M. A. Zaman, G. P. Martin, and G. D. Rees, "Mucoadhesion, hydration and rheological properties of non-aqueous delivery systems (NADS) for the oral cavity," *Journal of Dentistry*, vol. 36, no. 5, pp. 351–359, 2008.
- [27] G. P. Andrews, T. P. Lavery, and D. S. Jones, "Mucoadhesive polymeric platforms for controlled drug delivery," *European Journal of Pharmaceutics and Biopharmaceutics*, vol. 71, no. 3, pp. 505–518, 2009.
- [28] L. Perioli, V. Ambrogi, F. Angelici et al., "Development of mucoadhesive patches for buccal administration of ibuprofen," *Journal of Controlled Release*, vol. 99, no. 1, pp. 73–82, 2004.
- [29] B. Singh, R. Kumar, and N. Ahuja, "Optimizing drug delivery systems using systematic "design of experiments"—part I: fundamental aspects," *Critical Reviews in Therapeutic Drug Carrier Systems*, vol. 22, no. 1, pp. 27–105, 2005.
- [30] S. L. C. Ferreira, R. E. Bruns, H. S. Ferreira et al., "Box-Behnken design: an alternative for the optimization of analytical methods," *Analytica Chimica Acta*, vol. 597, no. 2, pp. 179–186, 2007.
- [31] G. E. P. Box and D. W. Behnken, "Some new three level designs for the study of quantitative variables," *Technometrics*, vol. 2, no. 4, pp. 455–475, 1960.
- [32] S. Chopra, S. K. Motwani, Z. Iqbal, S. Talegaonkar, F. J. Ahmad, and R. K. Khar, "Optimisation of polyherbal gels for vaginal drug delivery by Box-Behnken statistical design," *European Journal of Pharmaceutics and Biopharmaceutics*, vol. 67, no. 1, pp. 120–131, 2007.
- [33] V. M. Patel, B. G. Prajapati, and M. M. Patel, "Formulation, evaluation, and comparison of bilayered and multilayered mucoadhesive buccal devices of propranolol hydrochloride," *AAPS PharmSciTech*, vol. 8, no. 1, pp. E147–E154, 2007.
- [34] B. Sibeko, V. Pillay, Y. E. Choonara et al., "Computational molecular modeling and structural rationalization for the design of a drug-loaded PLLA/PVA biopolymeric membrane," *Biomedical Materials*, vol. 4, no. 1, Article ID 015014, 2009.
- [35] S. Azarmi, W. Roa, and R. Löbenberg, "Current perspectives in dissolution testing of conventional and novel dosage forms," *International Journal of Pharmaceutics*, vol. 328, no. 1, pp. 12–21, 2007.
- [36] A. Figueiras, J. Hombach, F. Veiga, and A. Bernkop-Schnürch, "In vitro evaluation of natural and methylated cyclodextrins as buccal permeation enhancing system for omeprazole delivery," *European Journal of Pharmaceutics and Biopharmaceutics*, vol. 71, no. 2, pp. 339–345, 2009.
- [37] P. Kumar, V. Pillay, Y. E. Choonara, G. Modi, D. Naidoo, and L. C. du Toit, "In silico theoretical molecular modeling for Alzheimer's disease: the nicotine-curcumin paradigm in neuroprotection and neurotherapy," *International Journal of Molecular Sciences*, vol. 12, no. 1, pp. 694–724, 2011.
- [38] M. E. Malone, I. A. M. Appelqvist, and I. T. Norton, "Oral behaviour of food hydrocolloids and emulsions—part 1: lubrication and deposition considerations," *Food Hydrocolloids*, vol. 17, no. 6, pp. 763–773, 2003.
- [39] S. Ramakrishna, K. Fujihara, W. E. Teo, T. C. Lim, and Z. Ma, *An Introduction to Electrospinning and Nanofibers*, World Scientific, London, UK, 2005.
- [40] P. Bottenberg, R. Cleymaet, C. de Muynck et al., "Development and testing of bioadhesive, fluoride-containing slow-release tablets for oral use," *Journal of Pharmacy and Pharmacology*, vol. 43, no. 7, pp. 457–464, 1991.
- [41] J. W. Lu, Z. P. Zhang, X. Z. Ren, Y. Z. Chen, J. Yu, and Z. X. Guo, "High-elongation fiber mats by electrospinning of polyoxymethylene," *Macromolecules*, vol. 41, no. 11, pp. 3762–3764, 2008.

- [42] E. Karavas, E. Georgarakis, and D. Bikiaris, "Application of PVP/HPMC miscible blends with enhanced mucoadhesive properties for adjusting drug release in predictable pulsatile chronotherapeutics," *European Journal of Pharmaceutics and Biopharmaceutics*, vol. 64, no. 1, pp. 115–126, 2006.
- [43] Y. Sudhakar, K. Kuotsu, and A. K. Bandyopadhyay, "Buccal bioadhesive drug delivery—a promising option for orally less efficient drugs," *Journal of Controlled Release*, vol. 114, no. 1, pp. 15–40, 2006.
- [44] B. Y. Yu, J. W. Chung, and S. Y. Kwak, "Reduced migration from flexible poly(vinyl chloride) of a plasticizer containing β -cyclodextrin derivative," *Environmental Science and Technology*, vol. 42, no. 19, pp. 7522–7527, 2008.
- [45] H. Abou-Rachid, L. Lussier, S. Ringuette, X. Lafleur-Lambert, M. Jaidann, and J. Brisson, "On the correlation between miscibility and solubility properties of energetic plasticizers/polymer blends: modeling and simulation studies," *Propellants, Explosives, Pyrotechnics*, vol. 33, no. 4, pp. 301–310, 2008.
- [46] P. Sakellariou, A. Hassan, and R. C. Rowe, "Plasticization of aqueous poly(vinyl alcohol) and hydroxypropyl methylcellulose with polyethylene glycols and glycerol," *European Polymer Journal*, vol. 29, no. 7, pp. 937–943, 1993.
- [47] N. K. Mongia, K. S. Anseth, and N. A. Peppas, "Mucoadhesive poly(vinyl alcohol) hydrogels produced by freezing/thawing processes: applications in the development of wound healing systems," *Journal of Biomaterials Science, Polymer Edition*, vol. 7, no. 12, pp. 1055–1064, 1996.
- [48] P. Kumar and M. Bhatia, "Functionalization of chitosan/methylcellulose interpenetrating polymer network microspheres for gastroretentive application using central composite design," *PDA Journal of Pharmaceutical Science and Technology*, vol. 64, no. 6, pp. 497–506, 2010.

Research Article

A Study of Surface Modifications of Carbon Nanotubes on the Properties of Polyamide 66/Multiwalled Carbon Nanotube Composites

Li Qiu,^{1,2} Yongkang Chen,^{1,3} Yongzhen Yang,^{1,4} Lihua Xu,^{1,2} and Xuguang Liu^{1,2}

¹ Key Laboratory of Interface Science and Engineering in Advanced Materials, Taiyuan University of Technology, Ministry of Education, Taiyuan 030024, China

² College of Chemistry and Chemical Engineering, Taiyuan University of Technology, Taiyuan 030024, China

³ University of Hertfordshire, School of Engineering and Technology, Hatfield, Hertfordshire AL10 9AB, UK

⁴ Research Center on Advanced Material Science and Technology, Taiyuan University of Technology, Taiyuan 030024, China

Correspondence should be addressed to Xuguang Liu; liuxuguang@tyut.edu.cn

Received 15 July 2013; Accepted 9 September 2013

Academic Editor: Raghavendra Hegde

Copyright © 2013 Li Qiu et al. This is an open access article distributed under the Creative Commons Attribution License, which permits unrestricted use, distribution, and reproduction in any medium, provided the original work is properly cited.

The effects of surface modification of carbon nanotube on the properties of polyamide 66/multiwalled carbon nanotube composites have been investigated. Polyamide 66 (PA66) and multiwalled carbon nanotube (MWCNT) composites were prepared by melt mixing. The surfaces of MWCNTs were modified with acid- and amine-groups. Field emission scanning electron microscopy analyses revealed that amine-MWCNTs (D-MWCNTs) dispersed better in the PA66 matrix than pristine- and acid-MWCNTs. However, an introduction of D-MWCNTs into PA66 matrix induced heterogeneous nucleation and affected the crystal growth process during the crystallization of PA66/MWCNT composites. Both nanoindentation and friction analyses were carried out in a study of the effect of the introduction of modified MWCNTs on both mechanical and friction properties of the composites. With the introduction of D-MWCNTs, both nanohardness and elastic modulus of the composites were significantly improved, but it was observed that the maximum depth, nanohardness, and elastic modulus of the composites showed no distinct change before and after a friction test. It is evident that PA66/D-MWCNT composites have the least friction coefficient of the PA66/MWCNT composites of all the approaches of carbon nanotube surface modification.

1. Introduction

For the past two decades, carbon nanotubes (CNTs) have attracted a great deal of attention in both academic and industrial aspects because of their remarkable self-lubricating, mechanical, electrical, and thermal properties, which allow them to be applied as high performance structure materials for aerospace and many other industrial fields [1–6]. Thus, CNTs are taken as good candidates for reinforcing a variety of polymers, ceramics, and metals. Among these promising materials, polymer/CNTs composites have been considered as one of the most attractive applications of CNTs with excellent performance and multifunction [7–11]. Moreover, the addition of CNTs can improve the mechanical and friction behavior of the polymer matrix. Recent investigations on

the mechanics and tribology of CNTs filled polymer by Chiu and Kao [9] and Meng et al. [11] show a high hardness and elastic modulus and low friction. However, the challenges for improving performance of polymer/CNTs composites include improving dispersity of CNTs in polymer matrix and enhancing the interfacial interactions between polymeric matrix and CNTs to promote the load transfer from polymer matrix to CNTs. As a result of the small diameter and the chemically smooth surface of CNTs, they usually exhibit a highly aggregated state in common solvents and polymer matrix. Also, CNTs usually form stabilized bundles because of the van der Waals and electrostatic interactions between CNTs and matrix. Therefore, a homogeneous dispersion of CNTs in polymeric matrix is the key to obtain excellent performance of polymer/CNT composites. It is necessary to

modify surface inertness of CNTs by functional groups or polymers that are either identical or structurally similar to matrix materials.

PA66 is a typical semicrystalline polymer and has been widely used in various engineering fields. PA66 is also the most important commercialized engineering plastic and possesses excellent chemical and abrasion resistance, plus low coefficient of friction, dimensional stability, toughness, and high hardness and strength. However, its lack of high temperature aging resistance and absorption of moisture in air lead to the inferior dimensional stability, which limits the applications of PA66. Both physical and mechanical properties of crystalline polymers are greatly dependent on the morphology, crystalline structure, and degree of crystallinity. Therefore modification and reinforcement of PA66 have drawn much attention to improve its physical properties and to introduce new properties. For example, Rodriguez-Pastor et al. [12] reported the preparation of helical-ribbon carbon nanofiber-based nylon-6,6 composites by three processing methods and the effect of CNTs modification methods on the properties of composites. Krause et al. [13] investigated the influence of CNTs production method and aspect ratio on percolation threshold of melt-mixed PA66.

This paper presents the new study outcomes in preparation of PA66/multiwalled carbon nanotube (MWCNT) composites by melt compounding using the twin-screw extruder; in microstructure characterization of different surface-modified MWCNTs within the polymer matrix by field emission scanning electron microscopy (FESEM) and Fourier transform infrared spectrometry (FTIR); and in a systematic investigation of the effects of surface modification of carbon nanotube on both mechanical and friction properties of the obtained composites using different experimental tools.

2. Experimental

2.1. Preparation of PA66/MWCNT Composite. Pristine MWCNTs (out diameter: 30–50 nm; length: 10–20 μm ; purity > 95%, P-MWCNTs) were treated with a mixture of $\text{H}_2\text{SO}_4/\text{HNO}_3$ (3:1, v/v) in an ultrasonic bath for 2 hours at 50°C. MWCNTs were filtered and washed with deionized water until pH became 7 and dried in vacuum to give acid-treated MWCNTs (A-MWCNTs). A-MWCNTs were reacted with excessive SOCl_2 under stirring at 70°C for 24 hours. The residual SOCl_2 was then removed by filtration and washed with tetrahydrofuran. Subsequently, the solid product was dried under vacuum at 80°C for 12 hours to give acylchloride-MWCNTs (MWCNTs-COCl). Ethylenediamine (360 mL) was added to a three-neck flask that contained MWCNTs-COCl (1.5 g), and the mixture was stirred at 120°C for 48 hours. After the reaction, the product was vacuum-filtered and washed for several times with anhydrous ethanol and dichloromethane; thus the amine-modified MWCNTs (D-MWCNTs) were obtained.

PA66/MWCNT composites were prepared by melt-blending PA66 (101L) with MWCNTs. The melt compounding was performed in a melt-blending process using a SHJ-36 twin-screw extruder. The temperature of the extruder was

maintained at 250, 260, 260, and 255°C from hopper to die, respectively. The rotation speed of the twin screw was 45 rpm. The composite containing 1.0 wt% MWCNTs was employed in this study. The pure PA66 was also extruded under the same conditions.

2.2. Surface Characterization and Property Tests. Fourier transformation infrared (FTIR) spectrometric measurements were performed by an FTIR spectrometer (SENSOR 27). The surface morphology of the cryofractured PA66/MWCNT composites was characterized by field emission scanning electron microscopy (FESEM).

The crystallization behaviors of the composites were carried out using a Q-100 (TA Instruments) differential scanning calorimeter (DSC) under nitrogen atmosphere to avoid any oxidation. The sample was heated from 40°C to 300°C at 10°C/min, held there for 5 min to erase any previous heating history, and then cooled from 300°C to room temperature (RT) at a cooling rate of 10°C/min.

The dry rolling-sliding friction tests were conducted using a twin disc wear testing machine. Full details of wear testing are similar to the previous work [14–16]. All discs were tested at the rotational speed of 1000 rpm, the applied load of 200 N, and the slip ratio of 14.29% in a rolling-sliding contact.

Mechanical properties of the worn surfaces were determined using a nano-indentation/scratching tester (Micro Material Ltd). A Berkovich indenter with a tip diameter of 50 nm was employed throughout the experiment. For all indentation tests, the initial load was set to be 0.05 mN and a constant maximum indentation load of 10 mN was applied with the loading/unloading duration of 15 seconds. Distance between each indent was not less than 15 μm in order to avoid any possible interference between neighboring indents. A test for each material was repeated for five times. Nano-hardness, reduced modulus, and elastic modulus were the average values of the results, and the presented loading-unloading curves were corresponding to the measured reduced modulus which was nearest to average value. The maximum relative standard deviation of the values for PA66, P-MWCNTs, A-MWCNTs, and D-MWCNTs were 9.887%, 2.145%, 1.901%, and 1.849%, respectively.

3. Results and Discussion

3.1. Dispersibility of MWCNTs in PA66 Matrix. FESEM observation was used to qualitatively and directly visualize the state of dispersion of MWCNTs in the PA66 matrix. The representative FESEM images of the cross-sectional cryofractured surface of the PA66/MWCNT composites with 1.0 wt% differently modified MWCNTs are shown in Figure 1. The bright spots and lines in the FESEM images were attributed to MWCNTs as a result of their high electrical conductivity. The dispersion of P-MWCNTs was found to be poor in the PA66 matrix, as shown in Figure 1(a); furthermore, the exposed P-MWCNTs were observed in the PA66 matrix. Therefore, it can be suggested that P-MWCNTs were mechanically mixed in the PA66 matrix so that the reinforcement effects of the MWCNTs have been weakened. It is unambiguous in

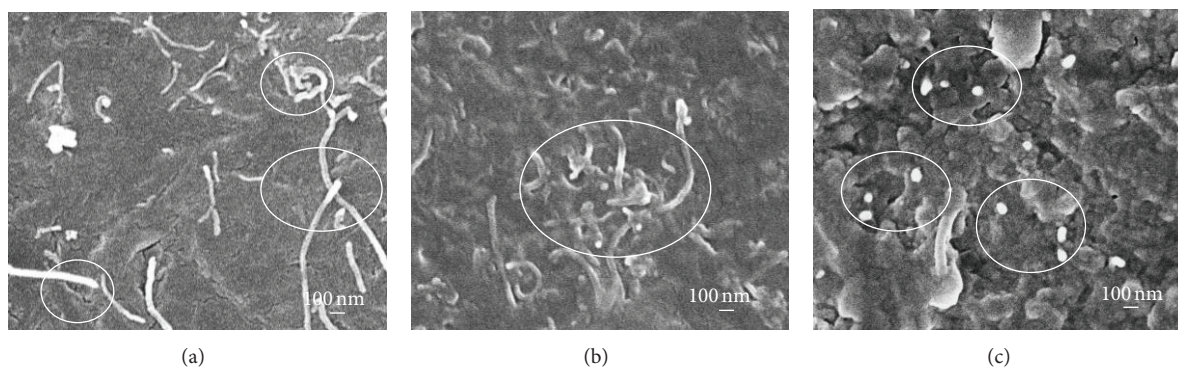


FIGURE 1: Fractured surfaces of PA66/MWCNT composites with 1.0 wt% MWCNTs: (a) PA66/P-MWCNTs, (b) PA66/A-MWCNTs, and (c) PA66/D-MWCNTs.

Figure 1(b) that the A-MWCNTs were dispersed in the PA66 matrix without any exposed MWCNTs while some agglomerations of MWCNTs were observed in the PA66 matrix. The good dispersion could be attributed to the increased polarity of the A-MWCNTs by the carboxylic groups, resulting in the increased compatibility between MWCNTs and PA66 matrix. As shown in Figure 1(c), amine-modified MWCNTs were uniformly dispersed in PA66 matrix, and when cryofractured, some nanotubes were pulled out from PA66 matrix. The good interfacial compatibility should be attributed to the formation of the -NHCO- groups on the surface of MWCNTs which served as a link to improve the interface bonds between D-MWCNTs and PA66 matrix. With homogeneous dispersion of D-MWCNTs it is suggested that they were embedded, debundled, and distributed throughout the matrix as a result of effective functionalization. The dispersion state of MWCNTs in the PA66 matrix was the key parameter for drastic improvements of the crystal and mechanical properties.

To confirm the reaction between PA66 and D-MWCNTs during melt mixing, FTIR spectra of PA66, D-MWCNTs, and PA66/D-MWCNT composites were measured and are shown in Figure 2. The strong band of pure PA66 at 3296 cm^{-1} was attributed to hydrogen bonded N-H stretching vibration. The absorption bands at 2933 , 2855 cm^{-1} , and 1195 cm^{-1} resulted from the symmetric and asymmetric C-H stretch vibrations and C-H twisting. The amide I band at 1629 cm^{-1} was mainly associated with the C=O stretching vibration. Amide II at 1533 cm^{-1} resulted from the N-H bending and C-N stretching vibration. The absorption band at 1273 cm^{-1} was due to C-N-H coupling vibration of the amide III band. In PA66/D-MWCNT composite, the band at 3440 cm^{-1} (O-H stretching vibration of alcoholic) and 1736 cm^{-1} (C=O symmetric stretching of carboxyl) in D-MWCNTs disappeared. It is suggested that D-MWCNTs were probably grafted on PA66 matrix by a condensation reaction during a melt-compounding process because this kind of reaction occurs easily between amine groups of D-MWCNTs' surface and carboxyl group of PA66. The same conclusion was also reached by other researchers [17, 18]. Also, because of the similarity of the surface functional groups of D-MWCNTs and PA66 chains, good compatibility can be expected even though

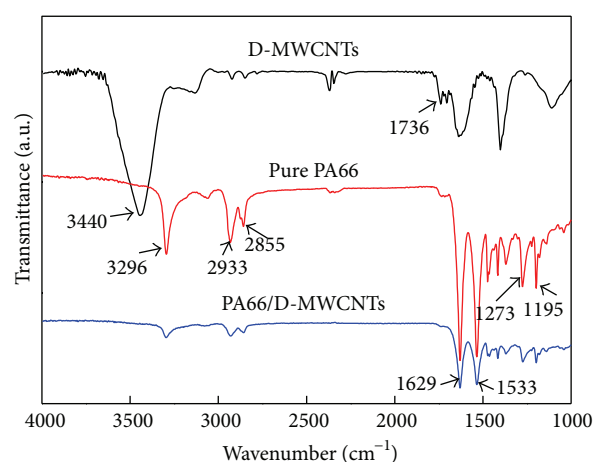


FIGURE 2: FTIR spectra of D-MWCNTs, pure PA66, and PA66/D-MWCNT composites.

no condensation reaction occurs between D-MWCNTs and PA66. Therefore, we think the disappeared peaks are an indication of, at least in part, the condensation reaction.

From FESEM and FTIR results, it can be seen that D-MWCNTs were uniformly dispersed in PA66 matrix and that molecular chain structure of PA66 showed no distinct difference owing to the chemical bonds between PA66 and D-MWCNTs.

3.2. Effects on PA66 Crystallinity. Usually, the crystallinity of polymer matrix significantly affects the friction property of the composites. Therefore, their crystallization behavior of PA66 matrix was investigated by DSC. Figure 3 shows the cooling thermograms of PA66 and PA66/MWCNT composites with 1.0 wt% MWCNTs obtained at a $10^\circ\text{C}/\text{min}$ rate. It can be seen that the pure PA66 had only a crystallization peak temperature at 232°C . The crystallization temperature shifted to a higher temperature, and the crystallization temperature range became broader with an introduction of MWCNTs, as had been reported in various polymer/CNTs composites [19, 20]. In general, inorganic fillers have two inconsistent influences on the crystallization of the semi-crystalline polymers.

TABLE 1: Melting and crystallisation parameters of PA66 and PA66/MWCNT composites with 1.0 wt% differently modified MWCNTs.

	T_m (°C)	ΔH_m (J/g)	X_t (%)	T_c (°C)	ΔH_c (J/g)
Pure PA66	266.89	55.01	28.35	232.11	49.70
PA66/P-MWCNTs	263.48	64.64	33.31	244.11	45.04
PA66/A-MWCNTs	262.04	63.71	32.83	243.37	46.42
PA66/D-MWCNTs	266.07	66.91	34.48	240.76	34.19

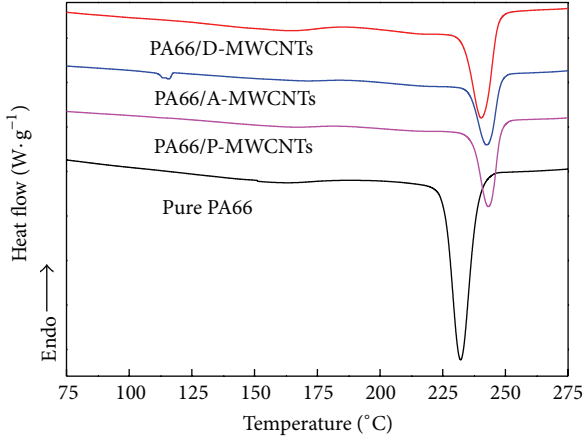


FIGURE 3: DSC thermograms on cooling of pure PA66 and PA66/MWCNT composites with 1.0 wt% MWCNTs.

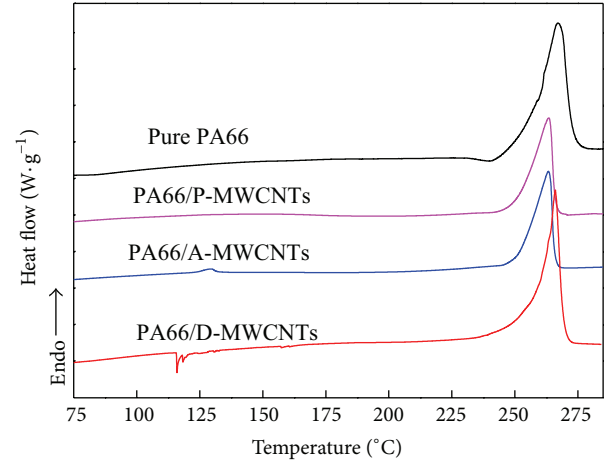


FIGURE 4: DSC thermograms on heating of pure PA66 and PA66/MWCNT composites with 1.0 wt% MWCNTs.

On one hand, they act as heterogeneous nucleating sites to facilitate the crystallization of polymers. On the other hand, they hinder the motion of polymer chain segments to retard the crystallization of polymers [18]. In the present work, the MWCNTs mainly acted as heterogeneous nucleating sites between the PA66 and MWCNTs and thus resulted in a higher crystallinity of the PA66 composites. However, the crystallization peak temperature of PA66/D-MWCNT composites was lower than that of the other composites. The low crystallization temperature of PA66/D-MWCNT composites could arise from polarity attraction or chemical interaction between amino end groups of D-MWCNTs and carboxylic groups of PA66.

Figure 4 shows the heating thermograms of PA66 and PA66/MWCNT composites with 1.0 wt% MWCNTs obtained at a 10°C/min rate. With heating pure PA66, only one endothermic peak, which was associated with the lamellar thickness of PA66 [21], was observed at 266.7°C. The introduction of MWCNTs into the PA66 matrix provided a large amount of nucleation sites for PA66 chains to restrained recrystallization or reorganization during the heating process in DSC testing [22], which resulted in only one melting peak of PA66. The changes in the characteristic parameters of the crystallization process are given in Table 1. The crystallinity degree of pure PA66 was 28.35%, while with 1.0 wt% D-MWCNTs incorporated in, the crystallinity degree increased to 34.48%. As the crystallinity degree of the sample materials increased and their ductility reduced, these resulted in lowering the ability of the surface to accommodate the impacts and high strain rates in the dry sliding friction test. This is

similar to that an increase in crystallinity reduced the wear rate of the polymer-matrix composite [23]. However, it was also reported that a decrease of crystallinity reduced the wear rate of the composite [24, 25]. This implies that the influence of the crystallization behavior, caused by an addition of the MWCNTs, is not the dominant factor for the enhancement of wear resistance.

3.3. Effects on Mechanical Properties. The mechanical properties of the composites, such as hardness, modulus, or the product of these factors, usually have significant influences on the wear behavior of the composites. According to previous research [26], materials with high hardness and high modulus would achieve lower friction coefficient. Thus, it is necessary to discuss the relationship between the mechanical properties and the tribo performance of polymer matrix composite.

A typical loading-unloading curve and the parameters used in an analysis of the nanoindentation test are shown in Figure 5. Among the mechanical properties which can be determined by a nanoindentation test, the elastic modulus (E) and the nano-hardness (H) are very common. They can be measured by analyzing the unloading part of the load-displacement curve. The nano-hardness (H) can be computed as

$$H = \frac{P_{\max}}{A}, \quad (1)$$

where P_{\max} is the maximum normal load and A is the contact area at the maximum load.

TABLE 2: Mechanical properties deduced from the nanoindentation test.

Specimen	Reduced modulus (GPa)		Elastic modulus (GPa)		Hardness (GPa)	
	Before test	After test	Before test	After test	Before test	After test
PA66	2.9927	3.8911	1.7699	2.3029	0.2191	0.2779
PA66/P-MWCNTs	3.0865	3.1707	1.8255	1.8755	0.2215	0.2335
PA66/A-MWCNTs	3.2916	3.1028	1.9472	1.8352	0.2218	0.2293
PA66/D-MWCNTs	3.0887	3.0938	1.8268	1.8299	0.2317	0.2271

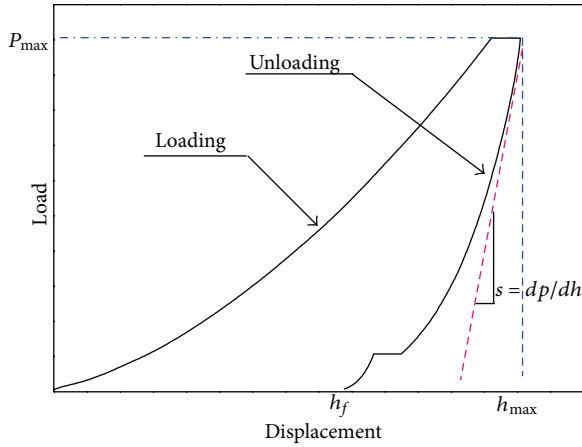


FIGURE 5: The loading and unloading curves in a nanoindentation test.

By considering the nonrigid indenters response, the elastic modulus (E) can be directly calculated through the following equation:

$$\frac{1}{E_r} = \frac{1 - \nu^2}{E} + \frac{1 - \nu_i^2}{E_i}, \quad (2)$$

where E_r is the reduced modulus of indentation contact; Poisson's ratio (ν) of PA66 is 0.41 [27]. For the diamond indenter, the elastic modulus (E_i) is 1140 GPa, and Poisson's ratio (ν_i) is 0.07.

The reduced modulus of elasticity (E_r) can be calculated from the unloading curve with Oliver-Pharr method [28] using the following equation:

$$E_r = \frac{\sqrt{\pi}}{2} \frac{dp}{dh} \frac{1}{\sqrt{A}}, \quad (3)$$

where dp/dh is the slope of the unloading curves.

Figure 6 gives loading-unloading curves, before and after a friction test, of pure PA66 and PA66/MWCNT composites with 1.0 wt% differently modified MWCNTs. These curves were obtained from the nanoindentation tests with a normal force of 10 mN. In Figure 6(a), before the friction test, the loading-unloading curves of specimens were shifted to the left, and maximum depth reduced with the addition of the modified MWCNTs, indicating that the composite's resistance to indentation gradually was increased with the addition of different modified MWCNTs. The indentation depths represent the contributions from the elasticity. This fact can

be deduced from the unloading curves. With the introduction of differently modified MWCNTs the slope of unloading curve was increased. According to (3), there is a linear relationship between modulus and the slope of unloading (i.e., stiffness), and a growth in stiffness will result in a higher modulus.

As shown in Figure 7(a) pure PA66 was increased drastically after a frictional test. It is suggested that because of the low weathering property, PA66 became aging after the friction test, which led to the enhancement of the hardness and modulus. Figure 7(a) also shows a clear increasing trend of elastic modulus as the introduction of differently modified MWCNTs. Moreover, the hardness was also increased by adding modified MWCNTs into the polymer matrix, as illustrated in Figure 7(b). The effect of differently modified MWCNTs on the hardness and elastic modulus of composites from the nanoindentation tests is summarized in Table 2. The results of H and E in Table 2 are the averaged values in the depth. After friction testing, loading-unloading curves of specimen were shifted to the right, and maximum depth was increased with the addition of the modified MWCNTs, as shown in Figure 6(b). Figure 7 also shows that the composites with 1.0 wt% D-MWCNTs are not affected in the maximum depth, nano-hardness, and elastic modulus before and after the friction test. By contrast, the nano-hardness and elastic modulus of the pure PA66 are increased when D-MWCNTs have been added into polymer matrix because of the intrinsic high strength and low friction coefficient of D-MWCNTs and the strong interfacial adhesive force between D-MWCNTs and PA66 matrix. It is suggested that the addition of D-MWCNTs had a significant effect on enhancement of mechanical properties and is also expected to affect the tribological behavior of the composites.

3.4. Effect on Frictional Properties. In a similar manner, the tribological behavior of material has a close relation with its crystallization and mechanical properties. Figure 8 presents the friction coefficient of the PA66 and PA66 composites with differently modified MWCNTs during the tests at a speed of 1000 rpm, load of 200 N, and slip ratio of 14.29%. Figure 8 shows that the friction coefficient of PA66 was low at the early stage of the tribological test. This is because, at the initial stage, the contact surfaces between two discs were dominated by a bedding-in process where the contact between two surfaces occurred mainly in the microasperity level. Such a contact resulted in a lower friction force. When such micropeaks were worn out, friction coefficient increased gradually. As shown in Figure 8, the friction coefficient of the composites was the lowest when D-MWCNTs were added

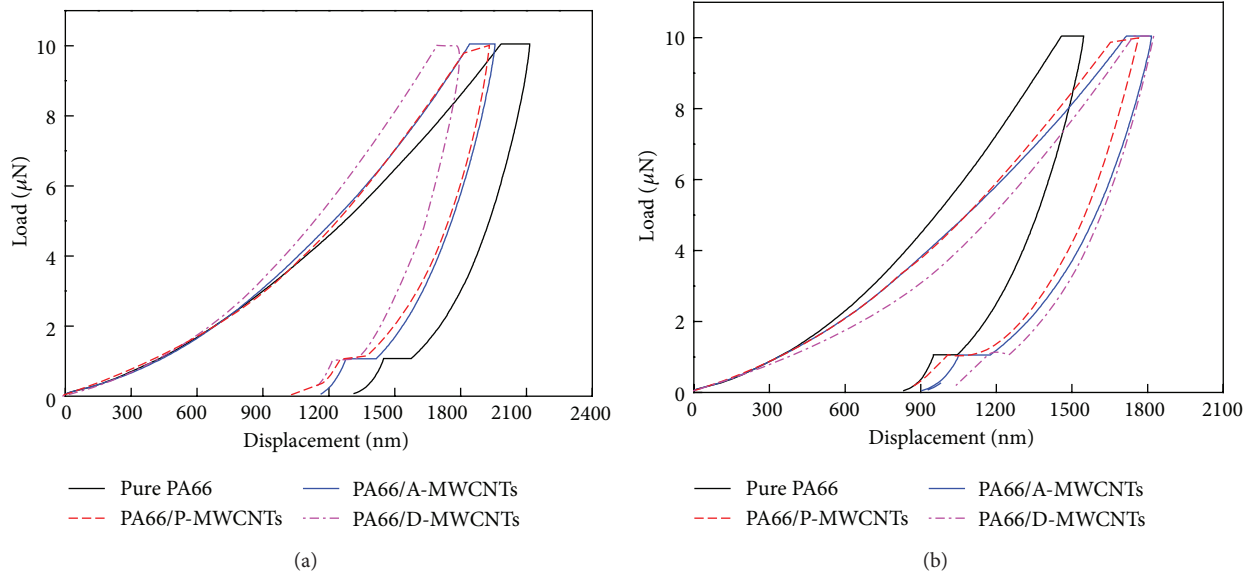


FIGURE 6: Loading-unloading curves of pure PA66 and PA66/MWCNT composites with 1.0 wt% MWCNTs: (a) before friction test and (b) after friction test.

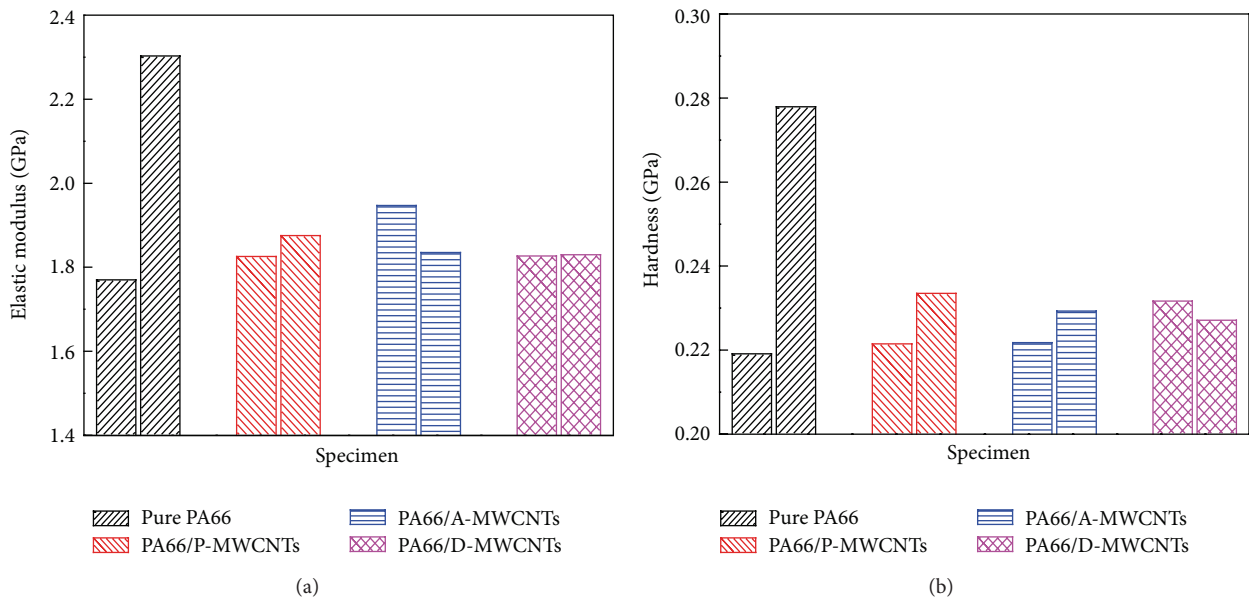


FIGURE 7: Elastic modulus (a) and nano-hardness (b) of PA66 and PA66/MWCNT composites with 1.0 wt% MWCNTs (left: before friction test and right: after friction test).

to PA66 matrix. There is a significant reduction of 17% in frictional coefficient between pure PA66 and D-MWCNTs composites. This observation is very similar to that of Yoo and Norman [23]. High crystallinity matrices produced a transfer film on interfacial layer with low friction coefficients. During a sliding friction test in dry condition, the formation of the transfer film was always thought to be an important factor to enhance the wear resistance of the polymer composite. During the friction process, this layer film was continuously replenished as the composite worn, until the surface became saturated with MWCNTs fragments.

As shown in Figures 7 and 8, it is evident that, with an addition of D-MWCNTs, the nano-hardness of composite increases, but the friction coefficient of the composite decreases. It is suggested that the introduction of MWCNTs into polymer matrix improved abrasive resistance of composites owing to their load supporting role during a friction process. The load supporting role displayed on enhancement of the mechanical properties of the polymer. The same tendency of mechanical properties and friction behavior may be both ascribed to the different morphology and polymer/MWCNTs interactions with differently modified MWCNTs.

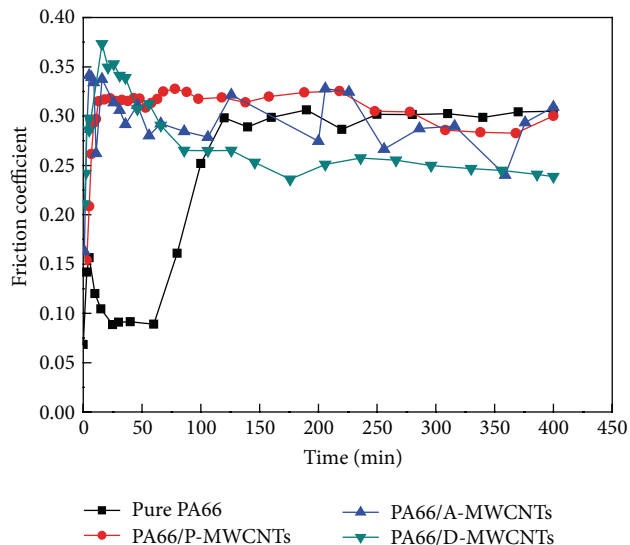


FIGURE 8: Friction coefficient curves for the pure PA66 and PA66/MWCNT composites with 1.0 wt% differently modified MWCNTs (at 200 N, 1000 rpm, and 14.29% slip ratio).

4. Conclusions

In this work, the effects of modification methods on the dispersion of MWCNTs and the resulting mechanical and friction properties of the composites have been investigated and the following conclusions can be drawn.

Amine functionalization of MWCNTs improved the dispersion of MWCNTs in PA66 matrix. Because of the chemical bonds between PA66 and D-MWCNTs, molecular chain structure of PA66 showed no distinct difference. The degree of crystallization and melting enthalpy of PA66/MWCNTs were enhanced via the introduction of D-MWCNTs.

Before a friction test, surface chemical modification of MWCNTs resulted in an obvious increase in the nano-hardness and elastic modulus of the composites. More interestingly, after the friction test, the nano-hardness and elastic modulus of the composites gradually reduced with the introduction of modified MWCNTs. The nano-hardness and elastic modulus of the PA66/D-MWCNT composites were almost unchanged, indicating the addition of D-MWCNTs effectively improved mechanical properties of the composites during the actual application process. The friction coefficient of the PA66/D-MWCNT composites was lowest of the all samples when D-MWCNTs were added to PA66 matrix.

Conflict of Interests

None of the coauthors have financial relationship with the commercial identities mentioned in this paper.

Acknowledgments

The authors acknowledge financial supports from Program for National Natural Science Foundation of China (21176169), Ph. D Programs Foundation of Ministry of Education of

China (20101402110007), and Research Project Supported by Shanxi Scholarship Council of China (2012-038).

References

- [1] S. Iijima, "Helical microtubules of graphitic carbon," *Nature*, vol. 354, no. 6348, pp. 56–58, 1991.
- [2] A. Thess, R. Lee, P. Nikolaev et al., "Crystalline ropes of metallic carbon nanotubes," *Science*, vol. 273, no. 5274, pp. 483–487, 1996.
- [3] S. J. Tans, M. H. Devoret, H. Dai et al., "Individual single-wall carbon nanotubes as quantum wires," *Nature*, vol. 386, no. 6624, pp. 474–477, 1997.
- [4] R. H. Baughman, A. A. Zakhidov, and W. A. De Heer, "Carbon nanotubes—the route toward applications," *Science*, vol. 297, no. 5582, pp. 787–792, 2002.
- [5] T. X. Liu, I. Y. Phang, L. Shen, S. Y. Chow, and W. Zhang, "Morphology and mechanical properties of multiwalled carbon nanotubes reinforced nylon-6 composites," *Macromolecules*, vol. 37, no. 19, pp. 7214–7222, 2004.
- [6] X. L. Xie, Y. W. Mai, and X. P. Zhou, "Dispersion and alignment of carbon nanotubes in polymer matrix: a review," *Materials Science and Engineering R*, vol. 49, no. 4, pp. 89–112, 2005.
- [7] J. M. Augustine, S. N. Maiti, and A. K. Gupta, "Mechanical properties and crystallization behavior of toughened polyamide-6/carbon nanotube composites," *Journal of Applied Polymer Science*, vol. 125, no. 1, pp. E478–E485, 2012.
- [8] S. H. Jin, K. H. Yoon, Y. Park, and D. S. Bang, "Properties of surface-modified multiwalled carbon nanotube filled polyethylene terephthalate composite films," *Journal of Applied Polymer Science*, vol. 107, no. 2, pp. 1163–1168, 2008.
- [9] F. C. Chiu and G. F. Kao, "Polyamide 46/multi-walled carbon nanotube nanocomposites with enhanced thermal, electrical, and mechanical properties," *Composites A*, vol. 43, no. 1, pp. 208–218, 2012.
- [10] Z. Yang, S. Huang, and T. X. Liu, "Crystallization behavior of polyamide 11/multiwalled carbon nanotube composites," *Journal of Applied Polymer Science*, vol. 122, no. 1, pp. 551–560, 2011.
- [11] H. Meng, G. X. Sui, G. Y. Xie, and R. Yang, "Friction and wear behavior of carbon nanotubes reinforced polyamide 6 composites under dry sliding and water lubricated condition," *Composites Science and Technology*, vol. 69, no. 5, pp. 606–611, 2009.
- [12] I. Rodriguez-Pastor, H. Varela-Rizo, D. R. Bortz, G. Montes de Oca, I. Guinea, and I. Martin-Gullon, "Effects of processing and functionalization methods on nylon-6,6 nanocomposites with Helical-ribbon carbon nanofibers," *Journal of Applied Polymer Science*, vol. 126, no. 4, pp. 1437–1448, 2012.
- [13] B. Krause, M. Ritschel, C. Täschner et al., "Comparison of nanotubes produced by fixed bed and aerosol-CVD methods and their electrical percolation behaviour in melt mixed polyamide 6.6 composites," *Composites Science and Technology*, vol. 70, no. 1, pp. 151–160, 2010.
- [14] Y. K. Chen, S. N. Kukureka, and C. J. Hooke, "The wear and friction of short glass-fibre-reinforced polymer composites in unlubricated rolling-sliding contact," *Journal of Materials Science*, vol. 31, no. 21, pp. 5643–5649, 1996.
- [15] S. N. Kukureka, C. J. Hooke, M. Rao, P. Liao, and Y. K. Chen, "Effect of fibre reinforcement on the friction and wear of polyamide 66 under dry rolling-sliding contact," *Tribology International*, vol. 32, no. 2, pp. 107–116, 1999.

- [16] Y. K. Chen, S. N. Kukureka, C. J. Hooke, and M. Rao, "Surface topography and wear mechanisms in polyamide 66 and its composites," *Journal of Materials Science*, vol. 35, no. 5, pp. 1269–1281, 2000.
- [17] P. C. Ma, N. A. Siddiqui, G. Marom, and J. K. Kim, "Dispersion and functionalization of carbon nanotubes for polymer-based nanocomposites: a review," *Composites A*, vol. 41, no. 10, pp. 1345–1367, 2010.
- [18] H. Meng, G. X. Sui, P. F. Fang, and R. Yang, "Effects of acid- and diamine-modified MWNTs on the mechanical properties and crystallization behavior of polyamide 6," *Polymer*, vol. 49, no. 2, pp. 610–620, 2008.
- [19] J. Li, Z. P. Fang, L. F. Tong, A. Gu, and F. Liu, "Effect of multi-walled carbon nanotubes on non-isothermal crystallization kinetics of polyamide 6," *European Polymer Journal*, vol. 42, no. 12, pp. 3230–3235, 2006.
- [20] Z. Y. Li, S. Z. Xu, W. T. Liu, S. Q. He, and C. S. Zhu, "Preparation and characterization of nylon610/functionalized multiwalled carbon nanotubes composites," *Journal of Applied Polymer Science*, vol. 113, no. 5, pp. 2805–2812, 2009.
- [21] G. F. Shan, W. Yang, X. G. Tang et al., "Multiple melting behaviour of annealed crystalline polymers," *Polymer Testing*, vol. 29, no. 2, pp. 273–280, 2010.
- [22] I. Y. Phang, J. Ma, L. Shen, T. Liu, and W. Zhang, "Crystallization and melting behavior of multi-walled carbon nanotube-reinforced nylon-6 composites," *Polymer International*, vol. 55, no. 1, pp. 71–79, 2006.
- [23] J. H. Yoo and S. E. Norman Jr., "Tribological behavior of blends of polyether ether ketone and polyether imide," *Wear*, vol. 162–164, pp. 418–425, 1993.
- [24] P. Werner, V. R. J. Altstadt, R. Jaskulka et al., "Tribological behaviour of carbon-nanofibre-reinforced poly(ether ether ketone)," *Wear*, vol. 257, no. 9–10, pp. 1006–1014, 2004.
- [25] G. Y. Xie, Y. J. Zhong, G. X. Sui, and R. Yang, "Mechanical properties and sliding wear behavior of potassium titanate whiskers-reinforced poly(ether ether ketone) composites under water-lubricated condition," *Journal of Applied Polymer Science*, vol. 117, no. 1, pp. 186–193, 2010.
- [26] A. Molazemhosseini, H. Tourani, and M. R. Naimi-Jamal, "Nanoindentation and nanoscratching responses of PEEK based hybrid composites reinforced with short carbon fibers and nano-silica," *Polymer Testing*, vol. 32, no. 3, pp. 525–534, 2013.
- [27] R. Jarrar, M. A. Mohsin, and Y. Haik, "Alteration of the mechanical and thermal properties of nylon 6/nylon 6,6 blends by nanoclay," *Journal of Applied Polymer Science*, vol. 124, no. 3, pp. 1880–1890, 2012.
- [28] W. C. Oliver and G. M. Pharr, "Measurement of hardness and elastic modulus by instrumented indentation: advances in understanding and refinements to methodology," *Journal of Materials Research*, vol. 19, no. 1, pp. 3–20, 2004.

Research Article

Nanofibrous *p-n* Junction and Its Rectifying Characteristics

Jian Fang, Xungai Wang, and Tong Lin

Australian Future Fibres Research and Innovation Centre, Deakin University, Geelong, VIC 3220, Australia

Correspondence should be addressed to Tong Lin; tong.lin@deakin.edu.au

Received 10 May 2013; Accepted 2 July 2013

Academic Editor: Raghavendra Hegde

Copyright © 2013 Jian Fang et al. This is an open access article distributed under the Creative Commons Attribution License, which permits unrestricted use, distribution, and reproduction in any medium, provided the original work is properly cited.

Randomly oriented tin oxide (SnO_2) nanofibers and poly(3,4-ethylenedioxythiophene)-poly(styrenesulfonate)/polyvinylpyrrolidone (PEDOT:PSS/PVP) nanofibers were prepared by a two-step electrospinning technique to form a layered fibrous mat. The current-voltage measurement revealed that the fibrous mat had an obvious diode-rectifying characteristic. The thickness of the nanofiber layers was found to have a considerable influence on the device resistance and rectifying performance. Such an interesting rectifying property was attributed to the formation of a *p-n* junction between the fibrous SnO_2 and PEDOT:PSS/PVP layers. This is the first report that a rectifying junction can be formed between two layers of electrospun nanofiber mats, and the resulting nanofibrous diode rectifier may find applications in sensors, energy harvest, and electronic textiles.

1. Introduction

Porous media have diverse applications ranging from filtration and gas/liquid adsorption to optics, electronics, sensors, and biomedicine. They can be prepared by different techniques with pores controllable on *macro*-, *meso*-, or *micro*-scales [1]. Nanofibrous materials represent a special class of porous media, made of nanofibers or nanowires, often in a form of thin fibrous structures. The large specific surface area, high porosity, and excellent pore interconnectivity have significantly enhanced their application performance. In electronic and energy areas, nanofibrous materials have been used as electrodes, separators, or active layers for development of batteries [2], solar cells [3], sensors [4], and power generators [5].

Despite the semiconducting characteristic of some nanofibers, nanofibrous materials are predominantly prepared to have homogeneous properties throughout the structure. Heterogeneous electrical property, such as diode *p-n* junction and rectifying effect, would enable a fibrous material to control the carrier transport, which creates opportunities to develop novel multifunctional nanofibrous materials and devices. Recently, a fully porous *p-n* junction prepared from porous silicon has been reported [6]. *p-n* junction carbon nanotube networks have also been prepared using a partial doping method [7]. However, *p-n* junction and rectifying

effect formed between two layers of different nanofibers have been little reported in the research literature.

In our recent study, we found that, when tin oxide (SnO_2) nanofibers and poly(3,4-ethylenedioxythiophene)-poly(styrenesulfonate)/polyvinylpyrrolidone (PEDOT:PSS/PVP) nanofibers were prepared separately by an electrostatic spinning, that is, electrospinning [8–12], technique to form a layered fibrous mat, a device made of this mat showed an interesting rectifying behavior and *p-n* junction characteristic. This fibrous device may find applications for textile electronics or rectifier for fibrous energy harvesters. In this paper, we report on the preparation of this novel nanofibrous device and its rectifying performance.

2. Experimental Details

2.1. Materials. Tin(II) chloride dehydrate ($\text{SnCl}_2 \cdot 2\text{H}_2\text{O}$), PVP, N,N-dimethylformamide (DMF), acetonitrile, and ethanol were purchased from Sigma and used as received. Tetrabutylammonium hexafluorophosphate (Bu_4NPF_6) was obtained from Fluka, and 1.3 wt% aqueous PEDOT:PSS solution (Baytron P) was kindly provided by H.C. Starck.

SnCl_2 -PVP solution was prepared by dissolving PVP ($M_w = 1,300,000$) and $\text{SnCl}_2 \cdot 2\text{H}_2\text{O}$ into a mixture of ethanol and DMF (1/2, v/v). The concentration of PVP and

SnCl_2 in the solution was 30.0 wt% and 21.0 wt%, respectively. PEDOT:PSS-PVP solution was prepared by adding 1 g PVP ($M_w = 360,000$) and 2.5 mL DMF into 4 mL Baytron P.

2.2. Electrospinning. Electrospinning was performed using a purpose made setup consisting of a high voltage power supply, a syringe pump, and a grounded collector [13]. During electrospinning, the spinning solution was loaded into a 5 mL plastic syringe with a 21-gauge metal needle. A syringe pump (KD Scientific) was used to control the flow rate, and a high voltage was applied between the needle and a grounded metal collector, using a high voltage power supply (ES3P-5W, Gamma High Voltage).

SnCl_2 /PVP nanofibers were electrospun under an applied voltage = 15 kV, spinning distance = 18 cm, flow rate = 0.6 mL/h. PEDOT:PSS/PVP nanofibers were directly electrospun (applied voltage = 18 kV, spinning distance = 15 cm, flow rate = 0.2 mL/h) from the second solution onto the surface of the SnO_2 nanofiber mat to form a second nanofibrous layer.

2.3. Device Fabrication. To prepare a rectifier device, SnCl_2 /PVP nanofibers were electrospun and deposited onto a thin aluminium plate (steps are illustrated in Figure 2(a)). SnO_2 nanofibers were then obtained by calcinating the as-electrospun nanofibers together with the aluminium substrate at 250°C for one hour and 500°C for 5 hours to remove all the organic components. Subsequently, PEDOT:PSS/PVP nanofibers were formed on the top of the SnO_2 nanofiber layer, followed by sputter-coating a layer of gold (Au) on the PEDOT:PSS/PVP nanofiber mat.

2.4. Characterizations. Morphology of the nanofibers was examined on a field emission scanning electron microscope (SEM, Supra V55). All samples were gold coated (Bal-tec SCD50 sputter coater), and the images were taken at an acceleration voltage of 5 kV. The fiber diameter was calculated using image processing software (Image Pro-Plus 4.5). X-ray diffraction (XRD) results were obtained on a diffractometer (PANalytical XRD) using Cu radiation 1.54 Å. The samples were analysed at room temperature with sampling intervals of 0.02° and a scanning rate of 0.25°/min. The average size of SnO_2 crystals was calculated according the Scherrer equation ($D = 0.9\lambda/\beta \cos \theta$), where λ is the wavelength of X-ray, θ is the diffraction angle, and β is the full width half max of the (211) diffraction peak. An electrochemical workstation (CHI760D) was used to measure the I - V characteristics and electrical impedance spectra (EIS) of the devices. The LUMO and HOMO energy levels of PEDOT:PSS/PVP nanofiber mat were also measured on CHI760D by a cyclic voltammetry (CV) method [14]. Acetonitrile was used as solvent and Bu_4NPF_6 (0.1 mol/L) as the support electrolyte. All the measurements were performed at room temperature.

3. Results and Discussion

Figure 1(a) shows the SEM image of the SnCl_2 /PVP nanofibers. The fibers had uniform morphology with an average

diameter of 674 nm. After the calcination treatment, the average diameter reduced to 368 nm (Figure 1(b)). Although the fiber surface became very rough (Inset image in Figure 1(b)) after the treatment, the fibers still retained the fibrous form without breakage.

The X-ray diffraction (XRD) patterns of the SnCl_2 /PVP and SnO_2 nanofibers are shown in Figure 1(c). The as-electrospun SnCl_2 /PVP nanofibers showed no obvious crystal peak, indicating an amorphous state. In contrast, strong diffraction peaks corresponding to SnO_2 crystal planes of (110), (101), (200), (211), (220), (002), (310), (112), (301), (202), and (321) were found in the spectrum, which matched well with the standard XRD data of SnO_2 (JCPDS-41-1445) [15]. This confirms that SnCl_2 has been converted to SnO_2 , and PVP has been removed from the fibers after the calcination treatment. Based on the (211) phase, the average SnO_2 crystal size was calculated by the Scherrer equation to be about 14 nm.

Figure 1(d) shows the SEM image of PEDOT:PSS/PVP nanofibers. The fibers looked uniform with a diameter of 103 ± 22 nm. Normally, the average diameter of electrospun nanofibers is about 200 nm. The smaller average diameter for the PEDOT:PSS/PVP nanofibers was attributed to the increased charge density and associated enhancement in fiber stretching when ionic PEDOT:PSS was present in the electrospinning solution [16].

The process for fabrication of the nanofibrous device is illustrated in Figure 2(a). After electrospinning (Figure 2(a)(I)), SnCl_2 /PVP nanofibers on an aluminum substrate were subjected to a calcination treatment to get pure SnO_2 nanofibers (Figure 2(a)(II)). Another layer of PEDOT:PSS/PVP nanofibers was then deposited directly onto the SnO_2 layer (Figure 2(a)(III)). After sputter-coating a thin layer of gold on the top surface of the PEDOT:PSS/PVP nanofiber mat (Figure 2(a)(IV)), a simple electronic device was finally formed. When the Au electrode was connected to the working electrode of the workstation, while the Al electrode was linked to the counter and the reference electrodes, and voltage was swept from -5.0 to $+5.0$ V, the device I - V curve was recorded. As shown in Figure 2(b), the I - V curves of the nanofibrous device showed a typical rectifying feature. The forward current increased with increasing the bias voltage, while the reverse current was maintained at a very low value regardless of the change of voltage. When the connection was reversed, the rectifying effect changed the polarity. These results clearly indicate that the nanofibrous device has a typical diode rectifying characteristic [17].

The thickness of nanofibers layer was found to play a key role in the rectifying behaviour. In this study, the nanofiber layer thickness was controlled through electrospinning time. For the SnO_2 nanofiber layer, short circuit occurred when the layer thickness was less than $3 \mu\text{m}$. However, the intrinsic stiffness of SnO_2 made it difficult to handle during the device fabrication, and when the SnO_2 nanofiber layer was thicker than $6 \mu\text{m}$, the SnO_2 layer was hard to connect with the electrode. Based on this, the nanofibrous devices were made by keeping the SnO_2 nanofiber layer thickness at $4 \mu\text{m}$ to achieve stable rectifying behaviour.

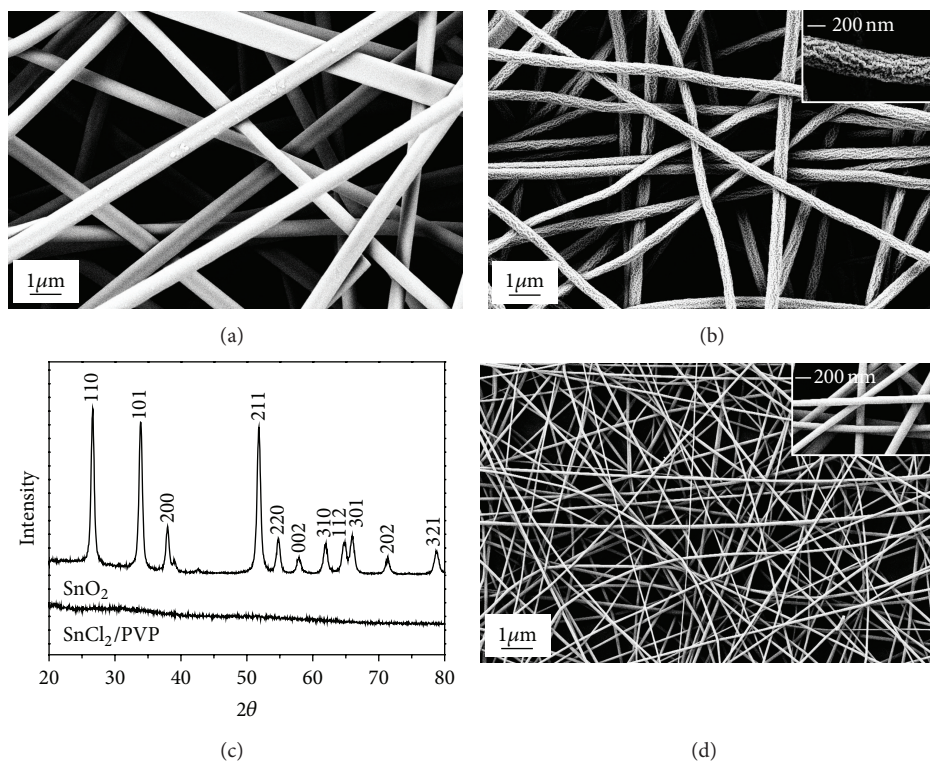


FIGURE 1: SEM images of (a) as-spun SnCl_2/PVP nanofibers and (b) SnO_2 nanofibers after calcination (the inset is a high magnification image), (c) XRD pattern of the SnCl_2/PVP and SnO_2 nanofibers, and (d) SEM image of the PEDOT:PSS/PVP nanofibers (the inset is a high magnification image).

In comparison to the SnO_2 nanofiber layer, the PEDOT:PSS/PVP layer was more flexible to adjust its thickness. Figure 2(b) also shows the effect of PEDOT:PSS/PVP fibrous layer thickness on the I - V characteristic. With increasing the thickness from $4.8 \mu\text{m}$ to $11.6 \mu\text{m}$, the forward current decreased, while the reverse current was almost unchanged.

Based on the I - V curves, the rectification ratio (R) and turn-on voltage of these devices were measured. R was calculated by $R = I^+/I^-$ (where I^+ is the forward current at forward bias of 5 V and I^- is the leaking current at reverse bias of -5 V). For the device with the PEDOT:PSS/PVP nanofiber layer thickness of 4.8 , 7.9 , and $11.6 \mu\text{m}$, the R value was 48 , 35 , and 35 , respectively, and the minimum forward voltage required to turn on the junction was 2.78 , 2.94 , and 3.07 V , respectively. Normally, the turn-on voltages for commercial silicon and germanium diodes are 0.7 and 0.3 V , respectively. The higher turn-on voltage of the nanofibrous devices was presumably due to the complex fibrous structure.

To verify the role of the nanofiber layers in the rectifying effect, the I - V characteristic of single nanofiber layer, either from SnO_2 or PEDOT:PSS/PVP, was also measured. As shown in Figure 2(c), a linear feature was obtained for the PEDOT:PSS/PVP nanofiber mat when it was sandwiched between Au electrodes, indicating the Ohmic contact between the PEDOT:PSS/PVP nanofiber mat and the gold. For SnO_2 nanofiber mat, a nonlinear I - V curve was formed when two Al electrodes were used, but without rectifying behavior. This is probably because of the weak bonding

between the SnO_2 nanofiber and the electrodes. When a thin layer of metal aluminium was inserted between the SnO_2 and PEDOT:PSS/PVP nanofiber layers, the rectifying effect disappeared also. Therefore, the SnO_2 and PEDOT:PSS/PVP nanofiber layers and their close contact are essential for the formation of the rectifying effect.

SnO_2 has been reported to have n -type semiconductor characteristic with a wide bandgap ($\sim 3.5 \text{ eV}$) [18, 19]. The conduction and valance bands of SnO_2 are -4.5 and -8.0 eV , respectively [20]. Since the size of SnO_2 nanofibers is far beyond the range showing the size effect, the effect of nanofibrous structure on the band energy level can be ignored.

It has been established that PEDOT:PSS is a p -type electroactive polymer with tuneable electrical conductivity [21]. The pure PEDOT:PSS was reported to have the lowest unoccupied molecular orbital (LUMO) and the highest occupied molecular orbital (HOMO) energy levels of -3.5 and -5.2 eV [22]. However, the presence of PVP in the PEDOT:PSS nanofibers could affect the energy levels of PEDOT:PSS/PVP nanofibers.

The LUMO and HOMO energy levels of the PEDOT:PSS/PVP nanofiber mat were measured by a CV method. During the measurement, PEDOT:PSS/PVP nanofibers on a Pt plate were used as the working electrode, a Pt plate as the counter electrode, and a Ag/AgCl (0.1 mol/L) standard electrode as the reference electrode. Figure 3(a) shows a typical CV curve of PEDOT:PSS/PVP nanofiber mat (PEDOT:PSS

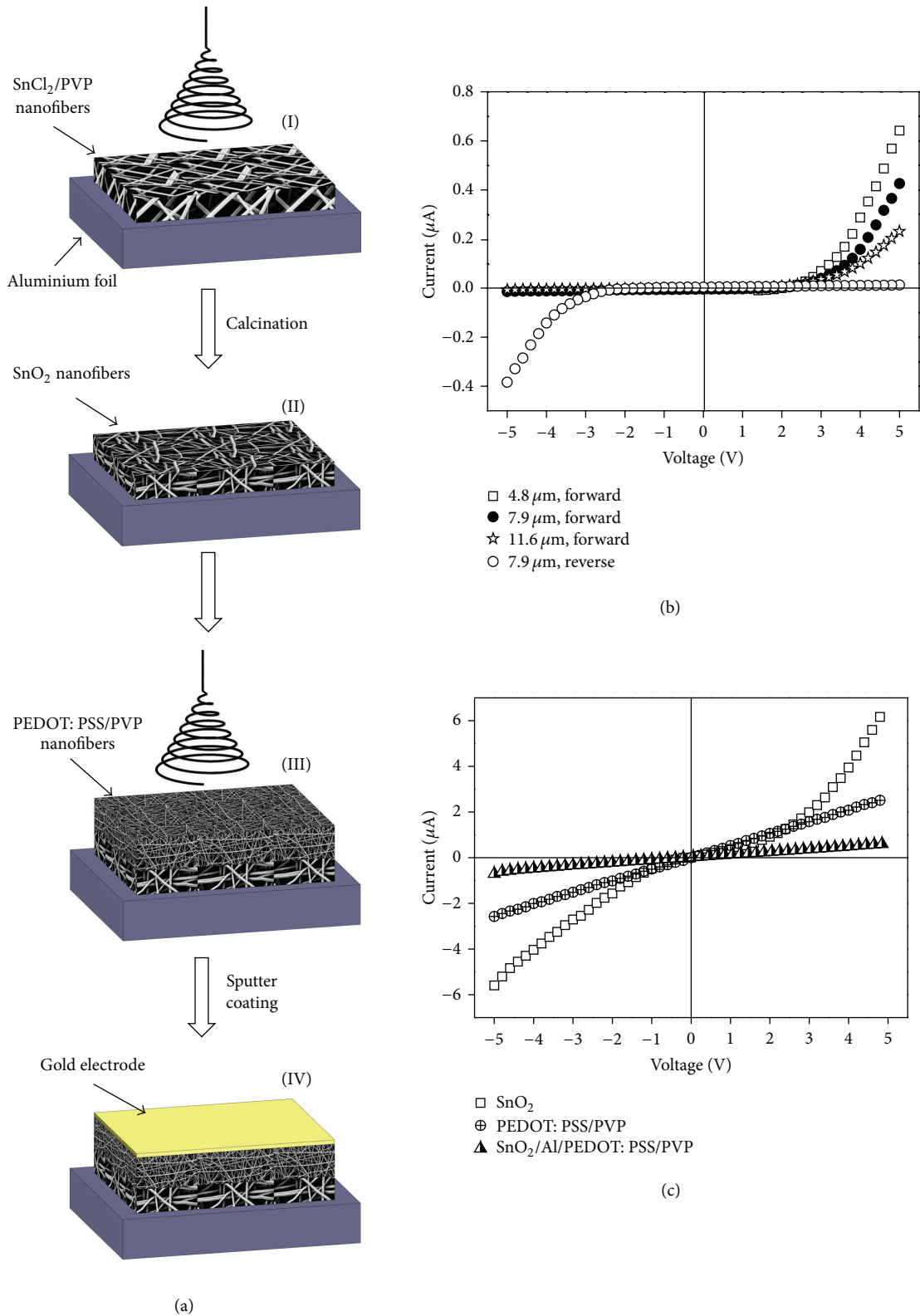


FIGURE 2: (a) Schematic illustration of device fabrication process, (b) I - V curves of the nanofibrous devices prepared with different thicknesses of the PEDOT:PSS/PVP nanofiber layer (SnO_2 nanofiber layer thickness = $4.0 \mu\text{m}$), and (c) I - V curves of nanofibers and the electrodes (SnO_2 nanofiber layer thickness = $4.0 \mu\text{m}$, PEDOT:PSS/PVP nanofiber layer thickness = $7.9 \mu\text{m}$).

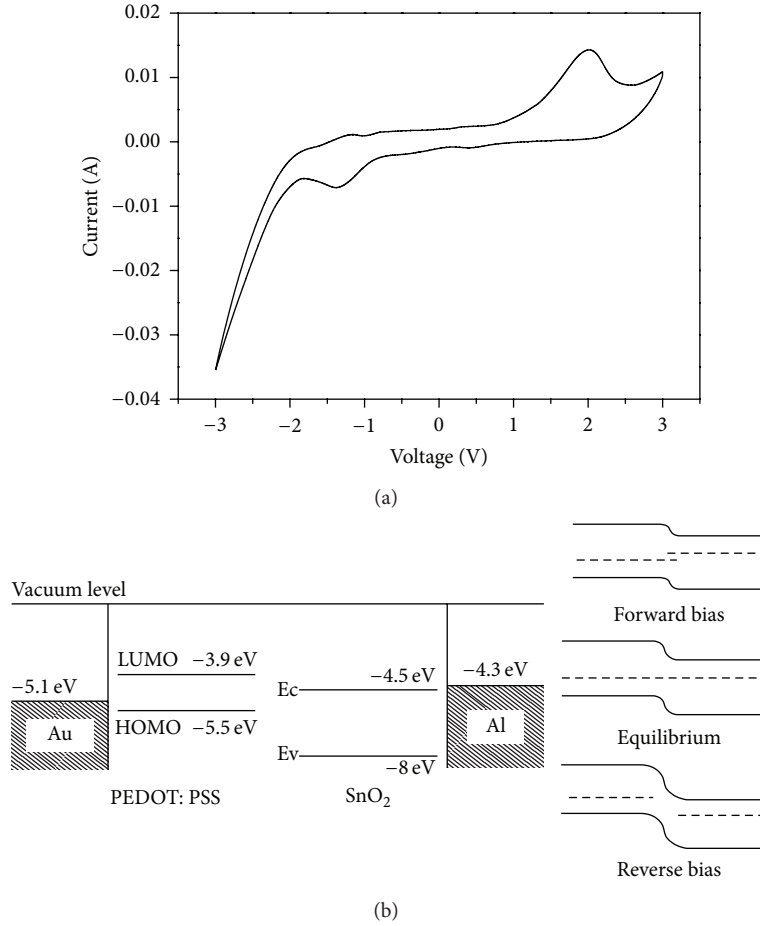


FIGURE 3: (a) Cyclic voltammogram curve of the PEDOT:PSS/PVP nanofibers, (b) energy band diagram of the junction.

thickness = 7.9 μm). The onset of the first oxidation (E'_{ox}) and reduction (E'_{red}) potential was 0.81 V and -0.75 V, respectively. The LUMO and HOMO levels calculated based on the CV curve were -3.9 eV and -5.5 eV, respectively. Therefore, the bandgap ($E_g = E'_{\text{ox}} + E'_{\text{red}}$) of the PEDOT:PSS/PVP nanofibrous mat is around 1.6 eV, which is similar to that of pure PEDOT:PSS reported [22].

Figure 3(b) shows the energy band diagram of gold, PEDOT:PSS/PVP, SnO₂, and aluminium before and after contact. The small difference between the work function of gold (-5.1 eV) and the HOMO level of PEDOT:PSS/PVP made them form an Ohmic contact. Similarly, aluminium and SnO₂ also form an Ohmic contact because of the small difference between the SnO₂ conduction band and the work function of aluminium (-4.3 eV). Upon close contact between a PEDOT:PSS/PVP and a SnO₂ nanofibrous layers, a p - n junction was formed. Electrons flow from the n -type SnO₂ nanofibers to p -type PEDOT:PSS/PVP nanofibers. Band bending resulted in a barrier. If the junction is forward connected, positive potential on the PEDOT:PSS/PVP nanofibers lowers their Fermi energy. The decreased barrier allows more charges to cross the junction. On the contrary, a reverse connection results in an increase in the barrier (Figure 3(b)).

To analyse the p - n junction, the standard thermionic emission model was employed, the I - V of which follows the relationship below [22]:

$$I = I_s \left[\exp \frac{qV}{nKT} - 1 \right], \quad (1)$$

where I_s is the saturation current, q is the elementary charge of $1.60217646 \times 10^{-19}$ coulombs, V is the applied voltage, n is the ideality factor, K is the Boltzmann constant of 8.62×10^{-5} eV K⁻¹, and T is the absolute temperature (300 K in this study). The saturation current and the ideality factor can be obtained from the semilog plot of the forward bias current (Figure 4). Reverse saturation current in p - n junction is caused by the migration of minority charge carriers and nearly independent of the reverse bias voltage. By measuring the lowest current value in the curves in Figure 4, the saturation current for the p - n junction with different PEDOT:PSS/PVP layer thicknesses was obtained, being about 7.02×10^{-5} , 5.52×10^{-5} , and 1.39×10^{-5} μA for the PEDOT:PSS/PVP thickness of 4.8, 7.9, and 11.6 μm , respectively. The ideality factor can be calculated as the slope of the broken lines in Figure 4, which are the linear fitted to the semilog plots. In this case, three tested p - n junctions had ideality factors of 2.03, 2.13, and 2.29 for the 4.8, 7.9, and

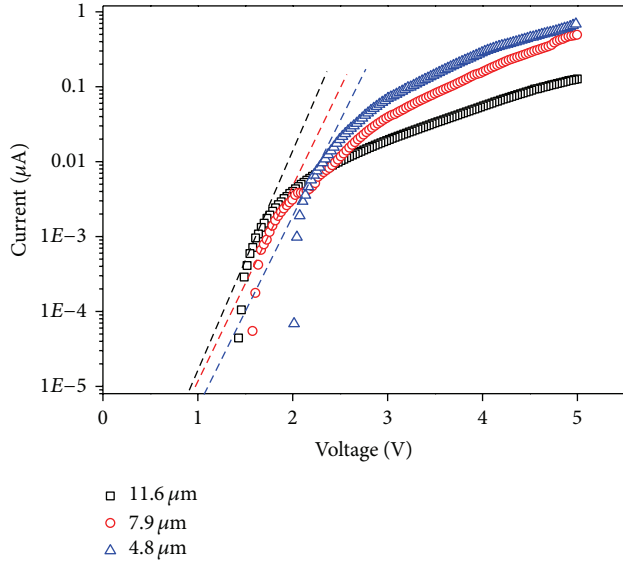


FIGURE 4: Semilogarithmic plot of the rectifying current versus applied voltage under forward bias.

11.6 μm PEDOT:PSS/PVP nanofiber layer, respectively. These ideality factors are slightly higher than the ideal value (1~2) of p - n diodes. This is presumably due to the complex electron transport within the nanofiber matrix.

Once the saturation current is known, the barrier height of the junction (ϕ_b) can be calculated by the following equation [22]:

$$\phi_b = -\frac{KT}{q} \ln\left(\frac{AA^*T^2}{I_s}\right) \quad (2)$$

Here junction area (A) was set based on the porosity of nanofiber mats and the working area of the device. For most of the electrospun nanofiber mats, the volume porosity was typically over 90% [23]. It is supposed that the chance for nanofibers to contact between two layers is determined by the areal porosity. In the case of nanofiber mat, the areal porosity is supposed to be similar to the volume porosity. The device with 1 cm^2 working area has a junction area $A = 1 \times (1 - 90\%) \times (1 - 90\%) = 0.01\text{ cm}^2$. A^* is the effective Richardson constant ($120\text{ A/K}^2\text{ cm}^2$). The barrier height of the three junctions was calculated to be 0.90, 0.91, and 0.95 eV for the PEDOT:PSS/PVP nanofiber layer thickness of 4.8, 7.9, and 11.6 μm , respectively.

To further explore the device performance, electrical impedance spectra (EIS) were tested. As shown in Figure 5, there is a complete semicircle at higher frequency range and an incomplete one at lower frequency range, which suggests that both material properties and electrode effect contribute to the device resistance. Bigger semicircle was observed on the spectra when the PEDOT:PSS/PVP layer was thicker, which represented a high electrical resistance of the rectifier. The resistance was obtained from the spectra as 1.89×10^7 , 2.88×10^7 , and $8.45 \times 10^7\ \Omega$ for the PEDOT:PSS/PVP thickness of 4.8, 7.9, and 11.6 μm , respectively. The difference

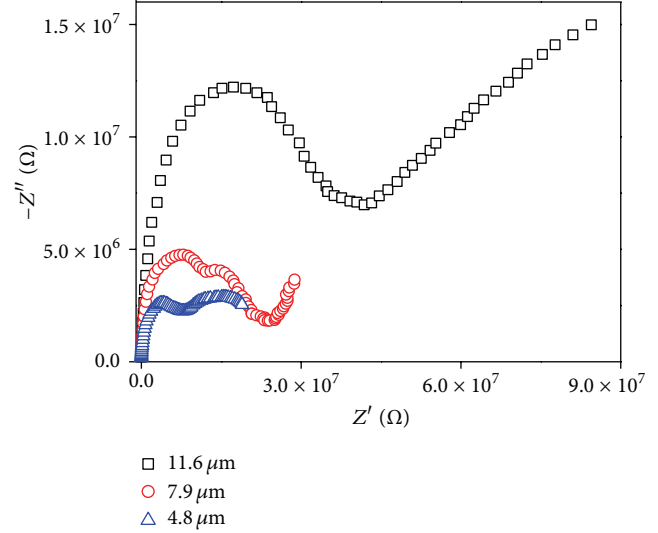


FIGURE 5: Electrical impedance spectra of the rectifier devices with different PEDOT:PSS/PVP nanofiber layer thicknesses.

in rectifying behaviour of three rectifiers should be closely related to the device resistance.

The results of this study have shown that electrospinning is a simple but effective approach to prepare fibrous electronic devices. Electrospun nanofiber webs and novel nanofibrous devices may be useful for development breathable textile electronics. Fibrous rectifiers could also be combined with fibrous power generators for energy harvesting applications. In our previous study, we have reported the mechanical-to-electrical conversion properties of electrospun polyvinylidene difluoride (PVDF) nanofiber webs [5]. The nanofibrous rectifier reported in this study could form a flexible candidate to convert AC signals that are generated by the PVDF nanofibers to DC outputs, which will be proven in our further work.

4. Conclusion

A layered fibrous p - n junction has been prepared using a two-step electrospinning technique. The device has an interesting rectifying property with a p - n junction formed between the SnO_2 and the PEDOT:PSS/PVP nanofiber layers. The thickness of the PEDOT:PSS/PVP nanofiber layers plays a significant role in determining the rectifying performance of the device. A thicker PEDOT:PSS/PVP nanofiber layer results in higher electrical resistance of the junction. This simple fibrous p - n junction rectifier may find novel applications in electronic textiles, sensors, and energy harvesting devices.

Acknowledgments

The authors would like to acknowledge the funding support from Australian Research Council (ARC) through its Future Fellowship Grant and Deakin University under the Central Research Grant scheme (CRGs).

References

- [1] E. A. Boucher, "Porous materials: structure, properties and capillary phenomena," *Journal of Materials Science*, vol. 11, no. 9, pp. 1734–1750, 1976.
- [2] L. Mai, L. Xu, C. Han et al., "Electrospun ultralong hierarchical vanadium oxide nanowires with high performance for lithium ion batteries," *Nano Letters*, vol. 10, no. 11, pp. 4750–4755, 2010.
- [3] M. Y. Song, D. K. Kim, K. J. Ihn, S. M. Jo, and D. Y. Kim, "Electrospun TiO₂ electrodes for dye-sensitized solar cells," *Nanotechnology*, vol. 15, no. 12, pp. 1861–1865, 2004.
- [4] C. Deng, P. Gong, Q. He et al., "Highly fluorescent TPA-PBPV nanofibers with amplified sensory response to TNT," *Chemical Physics Letters*, vol. 483, no. 4–6, pp. 219–223, 2009.
- [5] J. Fang, X. Wang, and T. Lin, "Electrical power generator from randomly oriented electrospun poly(vinylidene fluoride) nanofibre membranes," *Journal of Materials Chemistry*, vol. 21, no. 30, pp. 11088–11091, 2011.
- [6] W. Sun, N. P. Kherani, K. D. Hirschman, L. L. Gadeken, and P. M. Fauchet, "A three-dimensional porous silicon *p-n* diode for betavoltaics and photovoltaics," *Advanced Materials*, vol. 17, no. 10, pp. 1230–1233, 2005.
- [7] C. Biswas, S. Y. Lee, T. H. Ly, A. Ghosh, Q. N. Dang, and Y. H. Lee, "Chemically doped random network carbon nanotube *p-n* junction diode for rectifier," *ACS Nano*, vol. 5, no. 12, pp. 9817–9823, 2011.
- [8] T. Lin, J. Fang, H. Wang, T. Cheng, and X. Wang, "Using chitosan as a thickener for electrospinning dilute PVA solutions to improve fibre uniformity," *Nanotechnology*, vol. 17, no. 15, pp. 3718–3723, 2006.
- [9] J. Fang, H. Niu, T. Lin, and X. Wang, "Applications of electrospun nanofibers," *Chinese Science Bulletin*, vol. 53, no. 15, pp. 2265–2286, 2008.
- [10] T. Lin, H. Wang, and X. Wang, "Self-crimping bicomponent nanofibers electrospun from polyacrylonitrile and elastomeric polyurethane," *Advanced Materials*, vol. 17, no. 22, pp. 2699–2703, 2005.
- [11] J. Fang, H. Wang, H. Niu, T. Lin, and X. Wang, "Evolution of fiber morphology during electrospinning," *Journal of Applied Polymer Science*, vol. 118, no. 5, pp. 2553–2561, 2010.
- [12] J. Fang, H. Wang, X. Wang, and T. Lin, "Superhydrophobic nanofibre membranes: effects of particulate coating on hydrophobicity and surface properties," *Journal of the Textile Institute*, vol. 103, no. 9, p. 937, 2012.
- [13] T. Lin, H. Wang, H. Wang, and X. Wang, "The charge effect of cationic surfactants on the elimination of fibre beads in the electrospinning of polystyrene," *Nanotechnology*, vol. 15, no. 9, pp. 1375–1381, 2004.
- [14] Q. Peng, K. Park, T. Lin, M. Durstock, and L. Dai, "Donor- π -acceptor conjugated copolymers for photovoltaic applications: tuning the open-circuit voltage by adjusting the donor/acceptor ratio," *Journal of Physical Chemistry B*, vol. 112, no. 10, pp. 2801–2808, 2008.
- [15] X. Xu, J. Sun, H. Zhang et al., "Effects of Al doping on SnO₂ nanofibers in hydrogen sensor," *Sensors and Actuators B*, vol. 160, no. 1, pp. 858–863, 2011.
- [16] O. Martínez, A. G. Bravos, and N. J. Pinto, "Fabrication of poly(vinylidene fluoride-trifluoroethylene)/ poly(3,4-ethylenedioxythiophene)-polystyrene sulfonate composite nanofibers via electro spinning," *Macromolecules*, vol. 42, no. 20, pp. 7924–7929, 2009.
- [17] S. M. Sze and K. K. Ng, *Physics of Semiconductor Devices*, Wiley-Interscience, New York, NY, USA, 3rd edition, 2007.
- [18] Z. L. Wang, "Functional oxide nanobelts: materials, properties and potential applications in nanosystems and biotechnology," *Annual Review of Physical Chemistry*, vol. 55, pp. 159–196, 2004.
- [19] M. Batzill and U. Diebold, "The surface and materials science of tin oxide," *Progress in Surface Science*, vol. 79, no. 2–4, pp. 47–154, 2005.
- [20] X. Yong and M. A. A. Schoonen, "The absolute energy positions of conduction and valence bands of selected semiconducting minerals," *American Mineralogist*, vol. 85, no. 3–4, pp. 543–556, 2000.
- [21] Y.-Z. Long, M. M. Li, C. Gu et al., "Recent advances in synthesis, physical properties and applications of conducting polymer nanotubes and nanofibers," *Progress in Polymer Science*, vol. 36, no. 10, pp. 1415–1442, 2011.
- [22] B. K. Sharma, N. Khare, and S. Ahmad, "A ZnO/PEDOT : PSS based inorganic/organic heterojunction," *Solid State Communications*, vol. 149, no. 19–20, pp. 771–774, 2009.
- [23] X. Liu, T. Lin, J. Fang et al., "In vivo wound healing and antibacterial performances of electrospun nanofibre membranes," *Journal of Biomedical Materials Research*, vol. 94, no. 2, pp. 499–508, 2010.